EFFECTS OF MAGNETIC DOMAIN AND TWIN BOUNDARY INTERACTIONS ON MAGNETO-MECHANICAL PROPERTIES OF MAGNETIC SHAPE MEMORY ALLOYS

by

Medha Veligatla

A dissertation

submitted in partial fulfillment

of the requirements for the degree of

Doctor of Philosophy in Material Science and Engineering

Boise State University

December 2019

BOISE STATE UNIVERSITY GRADUATE COLLEGE

DEFENSE COMMITTEE AND FINAL READING APPROVALS

of the dissertation submitted by

Medha Veligatla

Dissertation Title:	Effects of Magnetic Domain and Twin Boundary Interactions on Magneto-Mechanical Properties of Magnetic Shape Memory Alloys
Date of Final Oral Examination:	27 September 2019

The following individuals read and discussed the dissertation submitted by student Medha Veligatla, and they evaluated the student's presentation and response to questions during the final oral examination. They found that the student passed the final oral examination.

Peter Müllner, Ph.D.	Chair, Supervisory Committee
Paul Simmonds, Ph.D.	Member, Supervisory Committee
Eric Jankowski, Ph.D.	Member, Supervisory Committee
Carlos J. Garcia-Cervera	Member, Supervisory Committee

The final reading approval of the dissertation was granted by Peter Müllner, Ph.D., Chair of the Supervisory Committee. The dissertation was approved by the Graduate College.

DEDICATION

I dedicate this work to my parents, Veligatla Sreenivas and Veerepalli Leela Rama Devi. It is their constant support and encouragement that motivated me in successfully completing this work.

ACKNOWLEDGMENTS

I am grateful to my advisor, Dr. Peter Müllner for his guidance and mentorship throughout this research. I would like to thank Dr. Carlos. J. Garcia-Cervera for his contribution to this research. I am most thankful to Dr. Paul Lindquist and the committee members: Dr. Paul Simmonds, Dr. Eric Jankowski, and Dr. Carlos. J. Garcia-Cervera for their valuable insights and support.

Dr. Anthony Hobza, a previous graduate student in this research lab, has been very helpful in transferring knowledge required to conduct this research and constantly providing meaningful insights whenever required. I am thankful to all the members of Dr. Müllner's research lab who helped me in conducting research and also maintained a good work culture (Listed in alphabetical order: Ali Mustafa, Andrew Armstrong, Bibek Karki, Brent Johnston, Jaime Guevara, Jiheon Know).

I am indebted to the support that was given by Dr. Bhaskar Chittori (Associate Professor, Civil Engineering) and Dr. Krishna Pakala (Assistant Professor, Mechanical & Biomedical Engineering). A special thank you to my dear husband, Navya Teja Goda who joined late in this journey yet supported me big time. Last but not the least, I would like to thank the Micron School of Material Science and Engineering and the Boise State University R2 Cluster for their financial assistance that was required for completing this research.

ABSTRACT

Magnetic shape memory (MSM) alloys deform substantially when exposed to a magnetic field. This recoverable plastic deformation occurs through crystallographic twinning. Thereby the internal magnetic domain structure modulates the deformation mechanisms through the interaction of magnetic domains with twin boundaries. We study the meso scale magneto-structural interactions that affect the macroscopic material properties of MSM alloys through computational micromagnetics. The study at the meso length scale is most effective as it allows for resolving interactions at the magnetic domain wall width resolution with reasonable computing cost. We apply micromagnetics simulations to evaluate the evolution of magnetic domains, their interaction with twin boundaries, the distribution of magnetic energies, and semi-quantitatively assess the magneto-mechanical properties of MSM alloys.

This dissertation addresses the following phenomena demonstrated by experimental findings: *1. The sample shape dependence of twin boundary propagation.* The results are useful to design actuators. Due to the sample shape, the demagnetization factor varies with the direction of the external magnetic field. Especially when the magnetic field is perpendicular to the long edge of the sample (high demagnetizing field), the magnetic energy intermittently increases with deformation (at low fields), which hinders twin boundary motion and results in gradual actuation. Whereas, when the applied magnetic field is parallel to the long edge of the sample (lowest demagnetizing field), the energy decreases with deformation and the twin boundary moves

instantaneously, resulting in abrupt actuation. *2. Magnetic domain and twin boundary interactions that result in work hardening.* This study addresses the monotonically increasing stress with ongoing deformation in fine twinned MSM alloys. Additional "vertical" magnetic domains form in densely twinned MSM alloys. The interaction of twin boundaries with these vertical magnetic domains results in magneto-elastic defects, which generate high local magneto-stresses. These interaction sites act as obstacles for twinning disconnections, similar to coherent particles in precipitation-hardened aluminum alloys. Whereas in a low twin density MSM alloy, these magneto-stress concentrations are dilute and their effectiveness is reduced by the synergistic action of many twinning disconnections. *3. Effect of magnetic field inclination on mechano-electrical energy conversion.* This study aids in evaluating the power harvesting capacity of MSM alloys. Using the concept of inverse magneto-plasticity (i.e. deformation-induced change of magnetization), experiments were performed in this dissertation to convert mechanical energy to electrical energy under a non-perpendicular bias magnetic field. The highest power output was obtained when the biased magnetic field was inclined with respect to the loading direction. The inclined magnetic field biases the magnetic domain structure such as to increase the magnetization component in the loading direction. This increases the conversion rate from mechanical to electrical energy.

When the MSM material accommodates the meso scale interactions between the magnetic and crystallographic structures, magnetic structures evolve with global and local spatial energy gradients and concentrations of magnetostress. These modulations hinder twin boundary mobility and determine the macroscopic magneto-mechanical properties of MSM alloys.

TABLE OF CONTENTS

LIST OF TABLES

LIST OF FIGURES

CHAPTER ONE: INTRODUCTION

Magnetic shape memory (MSM) alloys are a class of functional materials that exhibit large strain recovery. This recoverable strain occurs through crystallographic lattice reorientation in the martensite phase via twinning. Ni-Mn-Ga is a MSM alloy that has unique magneto-mechanical properties such as magnetic-field-induced deformation and magnetic-field-induced phase transformations. These properties make the Ni-Mn-Ga alloys suitable for applications in various fields such as actuators [1], sensors [2], micropumps [3] etc. In 1996, Ullakko [4] suggested using magnetic field induced reorientation of martensite variants for magnetically powered actuators. Ullakko hypothesized that with several percent strain and rapid control, the MSM alloys may outperform piezoelectric and magnetostrictive materials. Subsequently, Ullakko *et al.* demostrated the deformation in Ni-Mn-Ga with magnetic fields [5]. Following this discovery, research in this field progressed in increasing the magnetic-field-induced strain (MFIS). Subsequently 6 to 12 % MFIS was achieved in Ni-Mn-Ga with 10M and NM (non-modulated) martensite structures [6–8]. Ni-Mn-Ga alloys are magnetically anisotropic and this magnetic anisotropy provides a driving force to move the twin boundary, if the driving force exceeds the resistance for twin boundary motion. This driving force is characterized by the twinning stress. Therefore, the magnetic-field-induced motion of twin boundaries results in the MFIS. While the twin boundaries move in a magnetic field, they undergo a crystal lattice reorientation across twin boundaries. Therefore, this crystal lattice reorientation changes the directions of magnetization [9,10].

MFIS is a phenomenological property of the MSM alloys. Understanding this magnetic phenomenon requires the study of magnetic interfaces and their interactions with various microstructural defects. This involves the magnetic structure, the energy associated with these structures, and their interaction with microstructural features such as twin boundaries. There are numerous analytical methods that reveal these interactions qualitatively. However, research at the meso scale where the magnetic features interact with microstructural features is limited. The magnetic domain wall width is only a few nanometers [11] and resolving the magnetic energies associated at this scale is needed for better understanding the macroscopic shape change in MSM alloys. Calculation of magnetic energies is based on numerical methods that incorporate twin boundaries and magnetic domains [12–16]. Micromagnetism is the study of magnetic order on the meso scale, i.e. larger than atomistic and smaller than macroscopic properties and concerns the formation and structure of magnetic domain patterns. One methodology to assess micromagnetism qualitatively is micromagnetics, which solves the Landau-Lifshitz-Gilbert equation numerically for the time-dependent magnetization [17–19], thus generating equilibrium magnetic structures and their corresponding magnetic energies aid in the analysis of magnetic and crystallographic domain interactions.

This dissertation examines the effect of magnetic interactions on material properties using mesoscopic numerical simulations to complement experimental findings and to semi-quantitatively understand underlying physical phenomena. This study investigates the interplay of different magnetic energies that influence the magneto-mechanical properties of MSM alloys. The results of this study show that the propagation of a twin boundary is affected by the shape of the sample, the direction of the magnetic field, and the density of magnetoelastic defects. For the best actuation performance of Ni-Mn-Ga alloys, these are some of the important parameters to be considered. This study also characterizes the magnetic structures that alter the power generation capabilities in Ni-Mn-Ga. The results of this study aid the optimization of experimental parameters for improving the performance of Ni-Mn-Ga alloys in their respective application fields.

CHAPTER TWO: SCIENTIFIC BACKGROUND

2.1 Magnetism

Magnetism is a physical phenomenon occurring due to the motion of charged particles. This phenomena results in attractive and repulsive forces that are caused by the magnetic dipoles (also called magnetic moments usually represented by arrows with the head pointing north and the tail pointing south). This coil generates a magnetic field and the direction of this field is determined by the *right-hand thumb* rule. (The *right-hand thumb* rule- the thumb determines the direction of magnetic field when the remaining four fingers are curled in the direction of current flow/charge particles). So, in Figure 2-1, as the current flows through a cylindrical coil, the charged particles move in a circular motion.

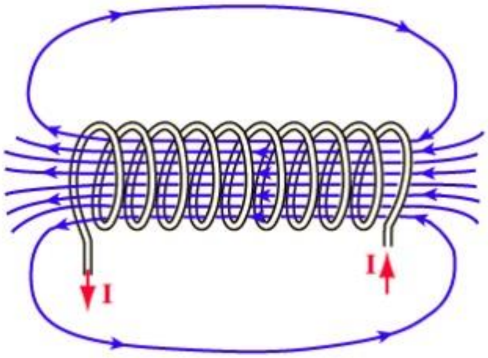

Figure 2-1 Schematic demonstrating the phenomena of magnetism in a current carrying cylindrical coil. The current flow through the coil is shown by red arrows and the magnetic field generated is denoted by blue lines with arrows indicating the direction [20]. Image was taken from webpage: https://physics.stackexchange.com

This results in a magnetic field and the direction of this field is represented by the blue arrows in Figure 2-1. A material is magnetized in a certain direction due to its net magnetization that results from the alignment of the magnetic moments. A small magnetization component is associated with these magnetic moments. Thereby, the magnetic moments play a vital role in determining the macroscopic magnetic properties of materials. These magnetic moments in a crystalline material can be thought to originate from revolving electrons in a planetary motion. In this thought experiments, electrons are viewed as particles. However, a quantitative description of magnetisms relies on quantum mechanics, which treats electrons as waves. Treatment of magnetism on quantum theory is beyond the scope of this introduction. To introduce the idea of atomic magnetic moments, the simple planetary model suffices. A schematic of this planetary motion is shown in Figure 2-2.

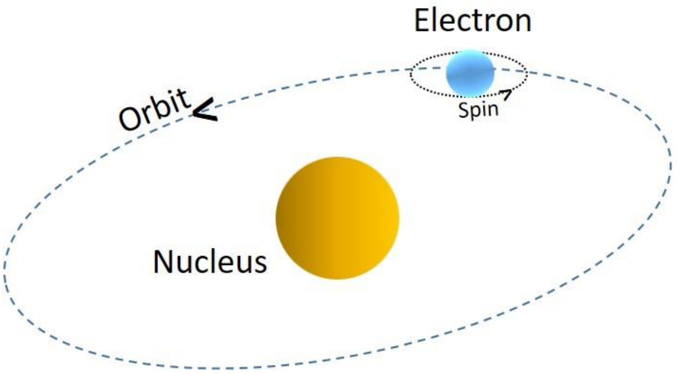

Figure 2-2: Schematic representing an electron orbiting about the nucleus of an atom and spinning about its own axis. The yellow circle represents the nucleus and the blue circle is the electron.

In this simplified assumption, electrons (charged particles) of an atom orbit around the nucleus. This generates a magnetic moment along its orbit axis called the orbital magnetic moment. While the electron orbits around the nucleus, it also spins about its own axis, resulting in a spin magnetic moment along its spin axis. Together the orbital and spin magnetic moments result in a net magnetic moment for each atom in a crystal [21].

The overall arrangement of these magnetic moments determines the magnetic nature of a crystal. Majorly, there are four categories of magnetic materials: (i) paramagnetic materials, (ii) diamagnetic materials, (iii) ferromagnetic materials, and (iv) antiferromagnetic materials. The schematic in Figure 2-3 shows the arrangement of the magnetic moments for these 4 types of magnetic materials. If the atoms carry no net magnetic moment, the material is diamagnetic and magnetic phenomena are entirely induction phenomena. Incomplete cancellation of magnetic moments results in a random arrangement of magnetic moments for a paramagnetic material. There is no net magnetization for a paramagnetic material. In a ferromagnetic material, all of the magnetic moments in the sample are aligned parallel, thus resulting in a net magnetization of the macroscopic sample. In an antiferromagnetic material, the magnetic moments of neighboring atoms are aligned in an anti-parallel arrangement, therefore resulting in no net magnetization in the macroscopic sample.

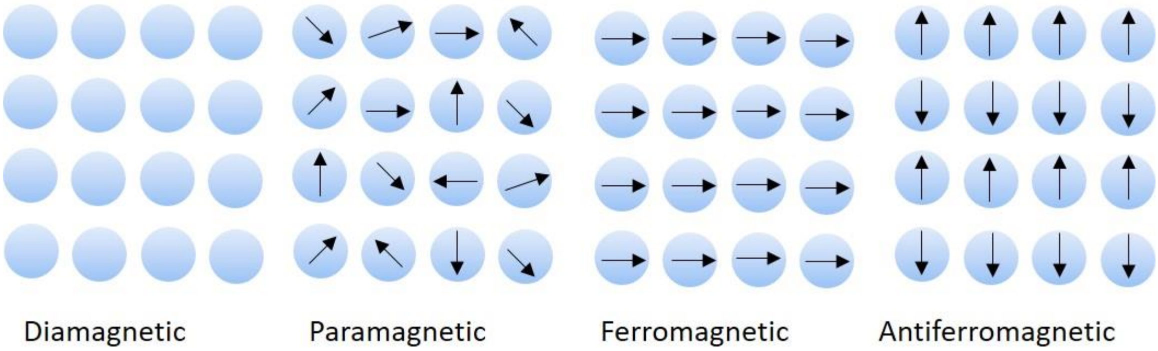

Figure 2-3: Schematic representing the arrangement of magnetic moments corresponding to each atom in a crystal structure for diamagnetic, paramagnetic, ferromagnetic, and antiferromagnetic materials. The circles represent the atoms in the crystal structure and the arrows represent the magnetic moments/dipoles.

2.2 Magnetic Energies

The arrangement of magnetic moments/dipoles in a material is a result of their magnetic equilibrium state. The four magnetic energy terms that contribute to this equilibrium state are exchange energy, anisotropy energy, Zeeman energy, and stray field energy. These are described in the following subsections:

2.2.1. Exchange Energy

The interaction energy between two neighboring spins is the exchange energy E_{ex}. This energy is responsible for ferromagnetism in magnetic materials. The exchange energy between two nearest spins is represented as

$$E_{ex} = -2JS_iS_j\cos\theta \tag{1}$$

where J is the exchange integral, S_i and S_j are two neighboring spins, and θ is the angle between the spins. The exchange energy has a minimum for parallel spins and a maximum for antiparallel spins.

2.2.2. Magnetocrystalline Anisotropy Energy

Magnetocrystalline anisotropy arises due to a directional preference of magnetization. The crystal structure causes anisotropy in material properties and magnetization is one such anisotropic property. The direction along which magnetic moments align spontaneously is the direction of easy magnetization. Rotating the magnetic moments away from this direction increases the energy. In the case of uniaxial magnetic anisotropy (i.e. system with only one axis of easy magnetization), the anisotropy energy E_{ani} is,

$$E_{ani} = K_1\sin^2(\theta_i)+K_2\sin^4(\theta_i)+\ldots \tag{2}$$

where K_1, K_2 are the first and second order anisotropy constants, θ_i is the angle between the magnetic moment and the easy axis. Often, for uniaxially anisotropic materials, researchers cut the series after the first term and set $K_1 = K_u$, where K_u is the uniaxial anisotropy constant (Table 1, in section 4.1.1).

2.2.3. Zeeman Energy

In the year 1896, Zeeman observed the splitting of energy levels when an atom is placed in an external magnetic field. There are two types of Zeeman effects, the *normal Zeeman effect* and the *anomalous Zeeman effect*. The *normal Zeeman effect*, takes only the angular momentum into account such that it considers only the paired electron state, where the total spin is zero. So, it considers the magnetic moment produced only by the orbital angular momentum. Whereas, the *anomalous Zeeman effect* considers both the orbital angular momentum and the spin angular momentum. Therefore, the magnetic moment associated with both orbital and spin momentum are taken into account.

The interaction of the magnetic moment of an atom with the magnetic field causes a change in energy. This change in energy is defined by the relative orientation of the magnetic moment with respect to the acting magnetic field.

$$\Delta E = -\mu_0 M H_e \cos\theta \tag{3}$$

where, ΔE is the change in energy, H_e is the external magnetic field, M is the magnetization, θ is the angle between the magnetization vector and the external magnetic field.

This change in energy was explained with the classical Lorentz theory. A moving electron in a magnetic field encounters a force (Lorentz force). Due to this force experienced by the electron, its orbit experiences a change which in turn affects the energy. This energy change is directly related to the orientation of the orbit with respect to the magnetic field direction. If the plane of the orbit is parallel to the magnetic field, the net Lorentz force is zero, which results in zero energy change i.e. $\Delta E = 0$, i.e. the lowest energy state. If the plane of the orbit is perpendicular to the magnetic field, depending on the clockwise or anti-clockwise rotation of the electrons, ΔE goes to a positive or negative value. So, the lowest energy configuration must have the magnetic dipoles/ moments aligned at 0° to the external magnetic field, while a highest energy configuration will have the moments aligned at 180° to the external field.

2.2.4. Stray Field Energy

With all the magnetic domains aligned in a parallel arrangement, the exchange energy is at the lowest value. With such an arrangement, the north and south poles are generated at the sample ends, which create a magnetic field around the sample, the stray field. Along with this, there is also a field generated inside the sample in the direction opposite to the magnetization. This internal field field H_{int} is proportional to the geometrical demagnetization factor (N_d) and to the magnetization (M):

$$H_{int} = N_d M \tag{4}$$

To lower the stray field energy, magnetic materials form multiple magnetic domains with opposing magnetization directions. As these magnetic domains form, due to the opposite direction of these moments in each of the domains, an alternating north pole and south pole form on the sample ends, which reduces the net magnetization.

2.3 Magnetic Domains

Below the Curie temperature, (temperature above which the material turns paramagnetic) a ferromagnetic material consists of groups of magnetic moments that are parallel. These groups are called magnetic domains. The direction of magnetization of each of these groups varies. Magnetic domain boundaries separate magnetic domains, with magnetic moments pointing in different directions. Across a magnetic domain boundary, the orientation of magnetic moments changes gradually from one magnetic domain to its neighboring magnetic domain. When an external magnetic field is applied, magnetic domains that are nearly aligned with the direction of the external field start to grow at the expense of the neighboring magnetic domains through the motion of magnetic domain boundaries. Additionally, at high magnetic field strength, the magnetic moments rotate to become parallel to the direction of the magnetic field. When all magnetic moments are parallel, the sample is magnetically saturated [21].

Twinning in MSM Alloys

In sections 2.1-2.3, we introduced concepts relating to magnetism. Here, we describe the deformation mechanisms in shape memory alloys. Also, we describe how the magnetic properties of magnetic shape memory alloys couple with the lattice. This coupling presents the basis for magnetic-field-induced straining.

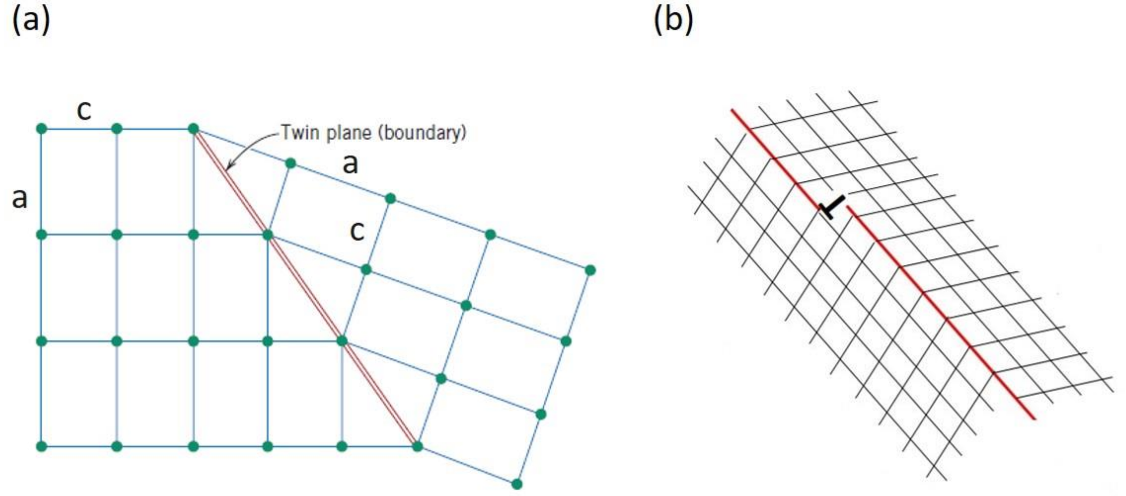

Figure 2-4 Schematics showing the twin boundary in a tetragonal crystal lattice with “a” and “c” representing the lattice parameters. (a) Represents the reorientation of the crystal lattice across a twin boundary (red). (b) Also represents the reorientation of the crystal lattice but on a smaller scale with a disconnection (inverse “T”) moving across the shear plane.

Deformation twinning is a shear mechanism. Thereby, a region deforms by a homogeneous shear in such a way that the deformed state has the same crystallographic structure, albeit in a different orientation than the original state. Figure 2-4 shows a schematic of this process. On the microscopic scale, twinning disconnections (also known as twinning dislocations) facilitate the propagation of the twin boundary as they move along the twin boundary (Figure 2-4b).

While the MSM alloy is strained, twin boundaries move through the material and change the orientation of the *c*-axis. Figure 2-5 illustrates the deformation mechanism (going from the fully compressed to the fully elongated state) in a single crystal MSM alloy with increasing magnitude of the external magnetic field. The volume fraction of the twin orientations change in a varying magnetic field, causing a resultant shape change. The first rectangular bar from the left represents a single martensite variant without twin boundaries and with its axis of easy magnetization (c-axis) parallel to the long axis of the sample. The gray inset shows the crystallographic orientation of the tetragonal unit cell. When a magnetic field acts perpendicular to the *c*-axis, the preferentially oriented twin domains (blue insets) start to nucleate and grow at the expense of the other (gray insets, central rectangular bar in Figure 2-5). The crystallographic orientation within each twin domain is represented by the insets (schematic of unit cell i.e. *c*-axis parallel or perpendicular to the long axis of the sample). As the field strength increases, the regions with blue insets grow and the twin boundaries move across the sample (rectangular bar on the right in Figure 2-5). This magnetic shape change occurs only if the magnetocrystalline anisotropy energy of the material is high enough to change the *c*-axis in the direction of the applied magnetic field. The maximum MFIS equals the spontaneous strain, i.e. $1 - c/a$ (c and a are the lattice parameters of the tetragonal crystal lattice for the martensite phase).

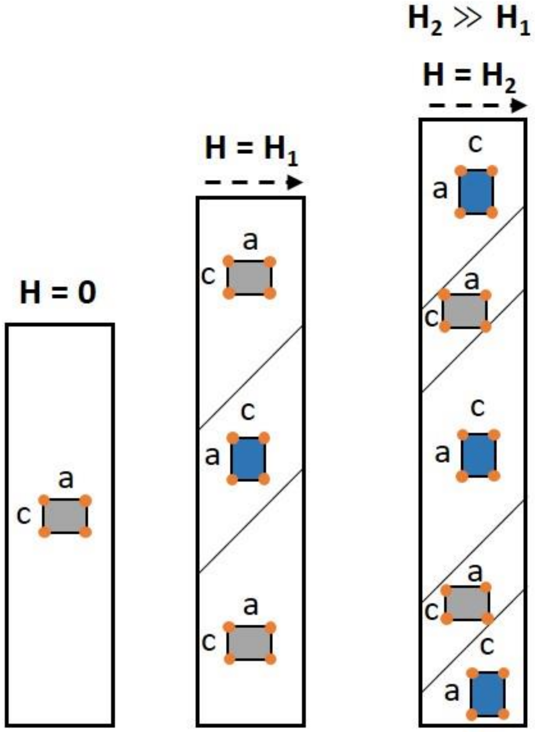

Figure 2-5 Schematic of the MSM effect in a single crystal Ni-Mn-Ga alloy. The lines (inclined at 45º to the length of the bars) across the rectangular bar represent twin boundaries. The change in orientation of the unit cell within each twin domain is represented by the insets. With increasing magnetic field (0 to H_2), the regions with c-axis parallel to the magnetic field grow at the expense of the others resulting in elongation.

The driving force for twin boundary motion in MSM alloys has been analytically described by various researchers [9,22–24]. Considering the interplay between stress and magnetic fields, the martensite variants, magnetic domains and magnetization rotation, Karaca *et al.* [25] proposed a microstructural sequence of mechanisms of the magnetization process in a heavily twinned MSM alloy martensite. The schematic in

Figure 2-6 shows the transformation from the austenite phase to the martensite phase under compressive stress and in the presence of a magnetic field. The schematic also describes the corresponding magnetic domain structure evolution while this transformation occurs. In

Figure 2-6, “2a” is a self-accommodated martensite structure formed by cooling the sample from austenitic temperature to room temperature without stress or a magnetic field.

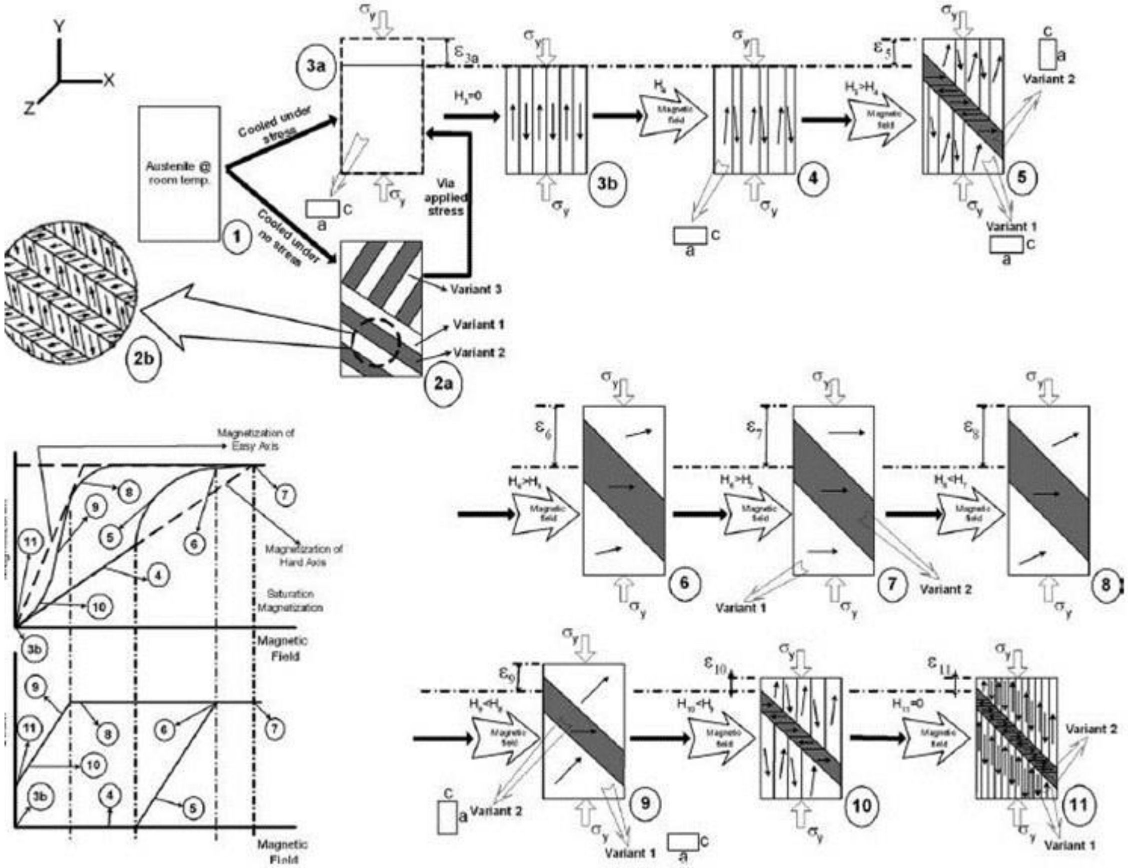

Figure 2-6 Schematic of magnetic and microstructural evolution of martensite twin variants illustrating magnetic field induced strain mechanism under different experimental conditions. Reprinted from Acta Materialia, 54, H. E. Karaca, I. Karaman, B. Basaran, Y. I. Chumlyakov, and H. J. Maier, pp 241, Copyright (2005), with permission from Elsevier [25].

In

Figure 2-6, “3a” is the martensite structure formed with a mechanical stress. For a multivariant case (schematics “2a-2b”), the twin microstructure and magnetic domains have a complex structure when compared to a single variant crystal (schematics “3a”). When a magnetic field is applied perpendicular to the compression direction, the domain wall motion and magnetization rotation take place simultaneously, even before martensite re-orientation. This is because domain wall motions occurs at lower magnetic field magnitudes than martensite reorientation. The change in magnetization rotation and formation of a second variant is shown from 4 to 5 (in

Figure 2-6), when a magnetic field is applied simultaneously with an external mechanical load. When the magnetic field reaches the saturation field, the magnetization direction of variant 1 completely rotates towards the applied magnetic field direction (7, in

Figure 2-6). When the magnetic field decreases, the applied stress works against the magnetic field and thus the magnetization direction of variant 1 rotates towards the easy axis (8, in

Figure 2-6). As the magnetic field is further decreased, the magnetic field might not be enough to favor variant 2, thereby variant 2 starts to reorient to variant 1, as shown in inset 9 (in

Figure 2-6). A further decrease in the magnetic field decreases the volume fraction of variant 2 while favoring the formation of variant 1. The final magnetic domain structure is shown in inset 10 (in

Figure 2-6).

Müllner et. al. [26] proposed a microscopic model to explain the MFIS in Ni-Mn-Ga MSM alloys with moving twin disconnections (described with a Burgers vector, b and its associated step height, t). They describe the role of internal magnetic force on the motion of twinning disconnections. For a microstructure with two martensite variants A and B that are separated by a twin boundary, the magnetostress (τ_M) is given by

$\tau_M = \frac{\Delta E_M}{s}$ (5)

where ΔE_M is the change in energy density between variant A and variant B that acts as a force on the disconnection and *s* is the twinning shear. If the easy axes of magnetization (*c*-axis) in variant A and variant B are nearly perpendicular across the twin boundary, the magnetic energies associated with these variants is given by $E_{M,A}$ and $E_{M,B}$ where

$E_{M,A} = -\mu_0 MH \cos(\gamma - \vartheta)\, K \sin^2 \vartheta$ (6)

$E_{M,B} = -\mu_0 MH \cos(\gamma - \vartheta)\, K \cos^2 \vartheta$ (7)

The total magnetic energy in each of these variants is the sum of the Zeeman energy and the magnetic anisotropy energy. *M* is the saturation magnetization, *H* is the applied magnetic field, γ is the angle between the the *c*-axis and the magnetic field, ϑ is the angle between the *c*-axis and the magnetization vector. Using equations (5), (6), and (7), the magnetostress experienced in a magnetic field (acting parallel to *c*-axis in one variant and perpendicular to the other variant due to the orientation of the *c*-axis across the twin boundary) is given by:

$$\tau_M = \begin{cases} \frac{\mu_0 MH}{s}\left(1 - \frac{\mu_0 MH}{4K}\right) & for\ H \le H_A \\ \frac{K}{s} & for\ H \ge H_A \end{cases} \quad (8)$$

where *K* is the magnetic anisotropy constant and H_A is the saturation magnetic field.

Müllner et. al [9] described the twin boundary propagation in a multi-variant martensite structure when there is a bias magnetic field to a sample that is under compressive stress. The direction of this magnetic field, compressive stress and the mechanism of twin boundary motion through moving dislocations is shown schematically Figure 2-7 as an inverse "T". *A* and *C* in Figure 2-7a are the two twin variants separated by a twin boundary. The orientation of the *c*-axis in their respective regions is denoted by

C_A and C_c. The direction of the compressive stress is represented by two arrows pointing towards each other and the arrow above the magnetic field (H) denotes its direction. TB labels the twin boundary and F_{mag}, the magnetic force and F_{mech}, the mechanical force are the two forces acting on the twinning dislocation. In Figure 2-7b, DB represents the domain boundary, in this case it is the boundary separating two martensite variants, F_{inter} acting in the direction of F_{mag} is the force generated due to the dislocation-dislocation interaction.

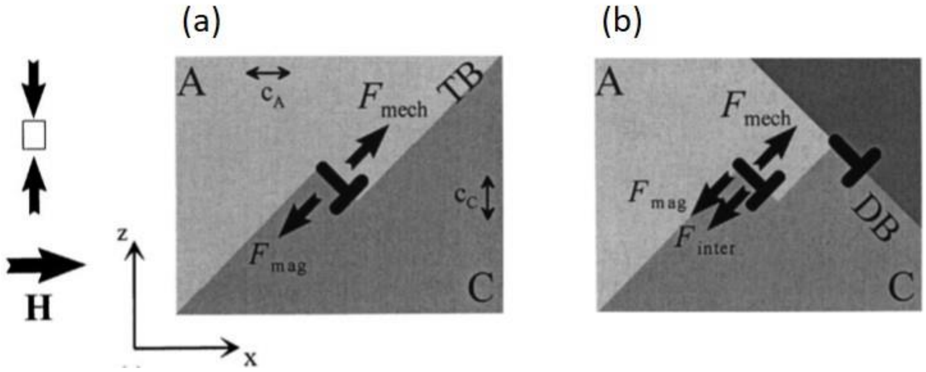

Figure 2-7 (a) A schematic representation of magnetic (F_{mag}) and mechanical (F_{mech}) forces acting on a twinning dislocation along a twin boundary (TB). (b) A schematic representation of magnetic (F_{mag}), mechanical (F_{mech}), and dislocation interaction (F_{inter}) forces that a twinning dislocation experiences as it approaches a martensite variant boundary (domain boundary- DB). Reprinted from Journal of Magnetism and Magnetic materials, 267, P. Müllner, V. A. Chernenko, and G. Kostorz, pp 331, Copyright (2003), with permission from Elsevier [9].

The first twinning dislocation that is blocked at the domain boundary obstructs the process of twinning. It repels all the subsequent dislocations. This repelling force can be overcome by increased mechanical stress/load and the subsequent twin dislocations can move and align along the domain boundary. While this process takes places, the dislocations experience repulsion when the distance from the wall is larger than their step height. As they move past this distance, the dislocation and the wall experience attraction, thus, resulting in a metastable state with dislocations piling up on the domain wall.

A statistical model to understand the reversible magnetostrain properties in twinned martensite was developed by Glavatska et. al. [22]. They incorporated a distribution of internal stress sources in their model and obtained the following criteria (9).

$$\langle (|\sigma_n| - |\sigma_c|)^2 \rangle = \sigma_0^2 \qquad (9)$$

$(|\sigma_n| - |\sigma_c|)$ is the critical stress that is needed to overcome the pinning of the twin boundaries. Where, $|\sigma_n|$ is the stress of the n^{th} twin boundary, $|\sigma_c|$ is the average stress value from the stress distribution curve, and σ_0 is a parameter describing the width of the distribution. This model was further improved by Chernenko et. al. [22] to obtain the effective twinning stresses at various magnetic fields and for samples with single and multi-variant martensite microstructures.

Recently, Müllner [24] developed a mechanism based model that predicted the twinning stresses for the different types of twin boundaries (type I- 0.33 MPa and type II- 4.7 MPa) and their temperature dependence. The model takes into account the difference in nucleation of the twinning disconnection loop for the two types of twin boundaries by comparing the energy of the growing disconnection loops to the work done by stress in expanding this loop. It was concluded that the activation energy for type I twin boundary is a material constant, whereas for type II depends on structural fluctuations at the interfaces. When the thermal energy is higher than these activation energies, the effect of temperature on twinning stress depends on the temperature dependence of the material's shear modulus and lattice constants.

Imaging Techniques for Studying the Evolution of Magnetic Domains

The interaction of magnetic domains and twin domains can be studied through various microscopy techniques such as Kerr microscopy [27], magnetic force microscopy [28], Bitter pattern imaging [13], scanning electron microscopy [29–31], magneto-optical method [32–34], atomic force microscopy [35], and interference contrast colloid and Lorentz transmission electron microscopy [36,37]. These methods offer a wide scale range from the nanometer scale to the sample scale on which twin microstructures occur. This section gives a brief overview of imaging techniques to study magnetic domains structures in twinned Ni-Mn-Ga alloys [31],[34], [28], [28],

2.7.1. Scanning electron microscopy

In 2005, Y. Ge *et al.* [38] applied two techniques to image magnetic domain interactions with SEM. In these two techniques, the surface of the image was perpendicular to the electron beam. The first technique evaluated the interaction of secondary electrons with the stray magnetic field above the sample surface that gave an overview of the underlying magnetic domain structure (obtained from the scanning electron image). In the second technique, the image was formed with backscattered electrons to reveal a detailed domain pattern. The contrast in this technique consists of both the absorbed and the

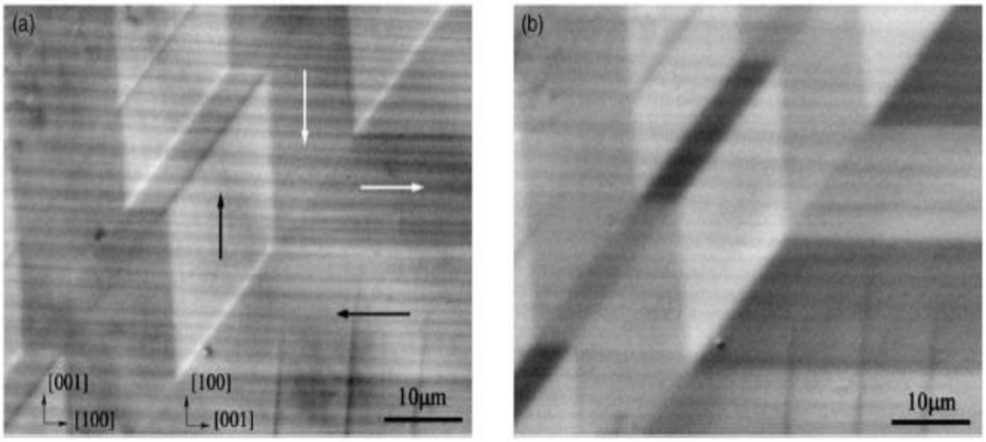

Figure 2-8 Magnetic domain structures in a two-variant Ni-Mn-Ga alloy obtained with backscatter electron imaging (a) in composition contrast mode and (b) in topography contrast mode. Arrows indicate the local direction of magnetization. Reprinted from [Y. Ge, O. Heczko, O. Söderberg, and V. K. Lindroos, Various magnetic domain structures in a Ni – Mn – Ga martensite exhibiting magnetic shape memory effect, J. Appl. Phys., 96, 2159, 2004], with the permission of AIP Publishing [38].

deflected electron contrast. Both methods reveal the in-plane magnetization component of the sample. Using these two techniques, Ge *et al.* [38] imaged interaction of magnetic domains with twin boundaries for various twin microstructures. The domain walls and domain contrasts for a two orientation specimen is shown in Figure 2-8. The composition contrast mode (COMPO mode) and the topography contrast mode (TOPO mode) are the two different backscatter electron imaging modes that captured the images in Figure 2-8. COMPO mode uses the sum signal from all the four-quadrant solid state diode backscatter detectors, while the TOPO mode uses the difference signal from two diagonal quadrants as the other two quadrants are turned off. Applying the type 2 method in COMPO mode, Ge *et al.* obtained images with good domain contrast and domain wall contrast for 180º domains (Figure 2-8a). With TOPO mode, high contrast between the 90º domains was obtained (Figure 2-8b). The domains that are connected by 90º domain walls (high contrast) coincide with twin boundaries. Microstructural details down to 5μm can be captured through this imaging technique. The high and low contrast transitions correspond to 180º domains. The arrows in the figure indicate the domains magnetized parallel to the easy axis of magnetization ([001] direction). Researchers studied various other twin structures and also identified regions where the direction of magnetization changes with similar imaging techniques [30,31].

2.7.2. Optical microscopy with magneto-optical indicator film

In 2007, Lai *et al.* [34] used an optical microscope equipped with an electromagnet to study the *in situ* microstructural and magnetic transformations during the motion of a twin boundary. This was done using a polarized light microscope with a magneto-optical indicator film. This indicator film captured the domain structure as the stray field from the domain structure on the sample surface caused an out-of-plane magnetization (in the indicator film). Figure 2-9 shows the evolution of magnetic domain patterns with an increasing magnetic field applied perpendicular to the axis of easy magnetization. A single

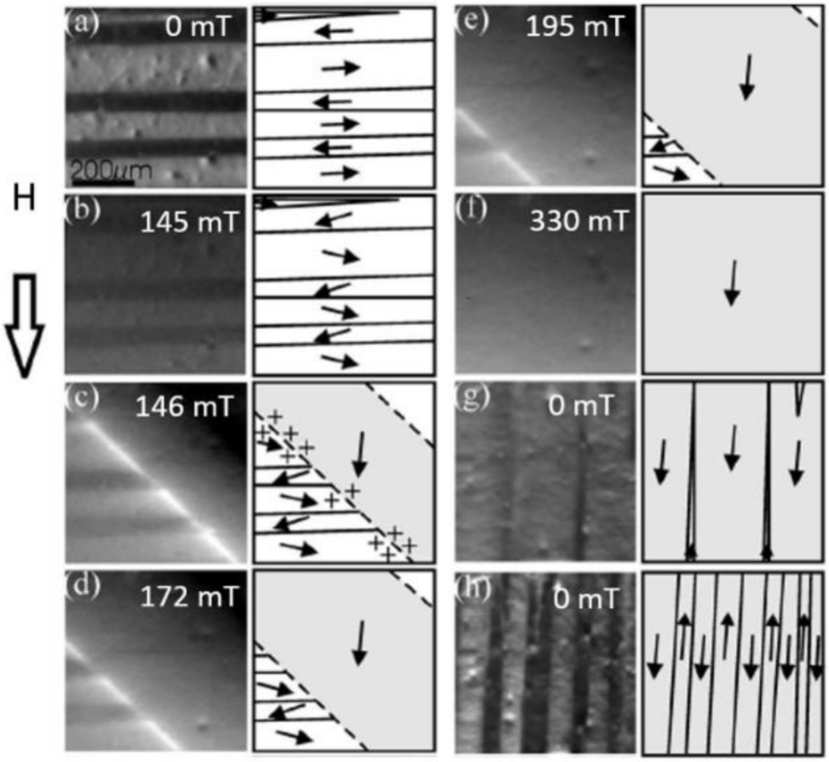

Figure 2-9 Evolution of magnetic domain patter with increasing magnetic field (a) to (f). The hollow arrow indicates the direction of applied field from 0 mT to 330 mT. The remanence and demagnetized states are shown in (g) and (h). Reprinted from [Y .W. Lai, N. Scheerbaum, D. Hinz, O. Gutfleisch, R. Schäfer, L. Schultz, and J. McCord, Absence of magnetic domain wall motion during magnetic field induced twin boundary motion in bulk magnetic shape memory alloys, Appl. Phys. Lett., 90, 192504, 2007] with the permission of AIP Publishing [34].

variant state is shown in Figure 2-9a, with magnetic domains separated by 180º domain walls. As the magnetic field was increased (the open arrow in the image indicates the field direction) the changes in domain structures were captured. Figure 2-9a through Figure 2-9e show the movement of a twin boundary and the change in domain structure as the twin boundary moves across the sample. With an increasing magnetic field, the magnetically favorable twin grows at the expense of the original twin domain. A single variant state is obtained in Figure 2-9f. After removal of the magnetic field and demagnetizing in the direction of the applied field, the sample has a regular single martensite variant magnetic domain structure, albeit with an orthogonal orientation of magnetization vectors (Figure 2-9g and Figure 2-9h).

Ge *et. al.* [30] reported, magnetic domains in Ni-Mn-Ga alloys imaged with an optical microscope using non polarized light. The sample surface analyzed under the microscope was magnetized to saturation such that the *c*-axis (axis of easy magnetization) is parallel to the long axis of the sample. However, there were traces of other minor variants (marked in Figure 2-10). The imaging surface was parallel to the (010) plane and consisted of two minor (101) twin variants (indicated in Figure 2-10) that run diagonally across the image. In both the twin variants the *c*-axis is in-plane and they are magnetized along their *c*-axis which results in a stair case like pattern. From the analysis pertaining to this image, they hypothesize that multi-domain structure forms that results in surface

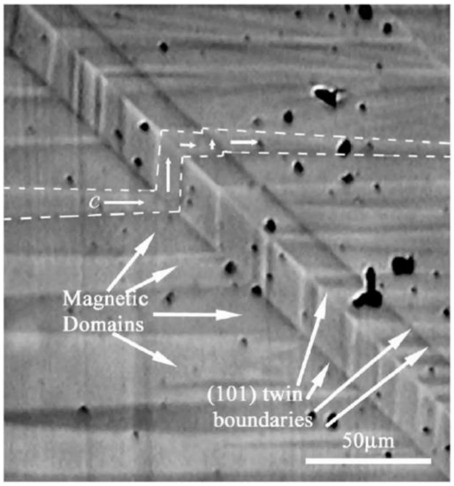

Figure 2-10 Magnetic domain configuration obtained for a Ni-Mn-Ga alloy using an optical microscope. One magnetic domain is traced with dashed lines and the orientation of c-axis (axis of easy magnetization) with in this domain is indicated by horizontal and vertical lines. Reprinted from [Y. Ge, O. Heczko, O. Söderberg, and S.-P. Hannula, Direct optical observation of magnetic domains in Ni-Mn-Ga martensite, Appl. Phys. Lett., 89, 082502, 2006] with the permission of AIP Publishing [30].

relief, which along with domain wall nucleation reduce the magnetostatic and magnetoelastic energies.

2.7.3. Scanning probe microscopy

Niklasch *et al.* [28] developed an *in-situ* loading frame to function in an atomic force microscope (AFM) for studying the interaction between magnetic domains and twin boundaries during a stress induced martensitic reorientation with a magnetized tip. This form of scanning probe microscopy is also known as magnetic force microscopy (MFM). Niklasch *et al*. [28] captured topography and magnetic force images while deforming a $Ni_{50}Mn_{30}Ga_{20}$ single crystal. The magnetized AFM tip first captures the topography of the sample surface in tapping mode, followed by another scan across the same area that captures the magnetic field gradient between the sample surface and the magnetized AFM tip. Figure 2-11a and Figure 2-11b demonstrate the topography and the

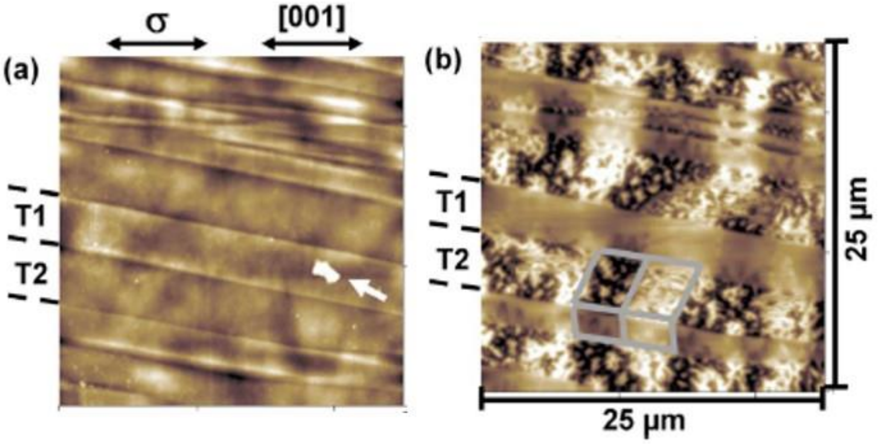

Figure 2-11 MFM imaging of (a) Topography (b) domain structure of a Ni-Mn-Ga alloy at 2.5% strain. In b, shallow contrast indicates in-plane magnetization while strong black/white contrast indicates out-of-plane magnetization. Reprinted from [D. Niklasch, H. J. Maier, and I. Karaman, Design and application of a mechanical load frame for in situ investigation of ferromagnetic shape memory alloys by magnetic force microscopy, Rev. Sci. Instrum. 79, 113701, 2008] with the permission of AIP Publishing [28].

magnetic domain structure respectively. The topography image shows the twin variants indicated by T1 and T2. The MFM image of the same region has different contrasts. The two variant regions have in-plane domain structures, resulting in weaker contrast. The twin boundary between the two variants coincides with the 90^o domain walls. Every alternate twin variant region has internal domain structures with bright and dark contrasts. These internal domain structures are separated by 180^o domain walls. The gray boxes in Figure 2-11 indicates the magnetic domains. Formation of such internal domain structures balances the magnetocrystalline and magnetostatic energies.

2.7.4. Transmission electron microscopy

Venkateswaran *et al.* [28] studied the magnetic domains of twinned Ni-Mn-Ga with Lorentz microscopy in the transmission electron microscope. Figure 2-12 demonstrates a phase reconstruction of a Fresnel through focus series from martensite plates (c-axis in plane with the foil). Figure 2-12a through Figure 2-12c show domain walls that coincide with twin boundaries and also domain structures within these twin boundaries. Figure 2-12d is the phase reconstruction resulting in a herringbone martensite domain structure that clearly shows a pair of white and black phase ridges. Figure 2-12e and Figure 2-12f are gray scale induction components that indicate the different directions of magnetic inductions. The color plot of this gray scale magnetic induction image is Figure 2-12g. The color plot clearly delineates the 90° and 180° domain walls. The domain walls that coincide with the twin boundaries are the 90° walls and those lying within a twin variant are the 180° domain walls. A schematic of these 90° and 180° walls across and within the

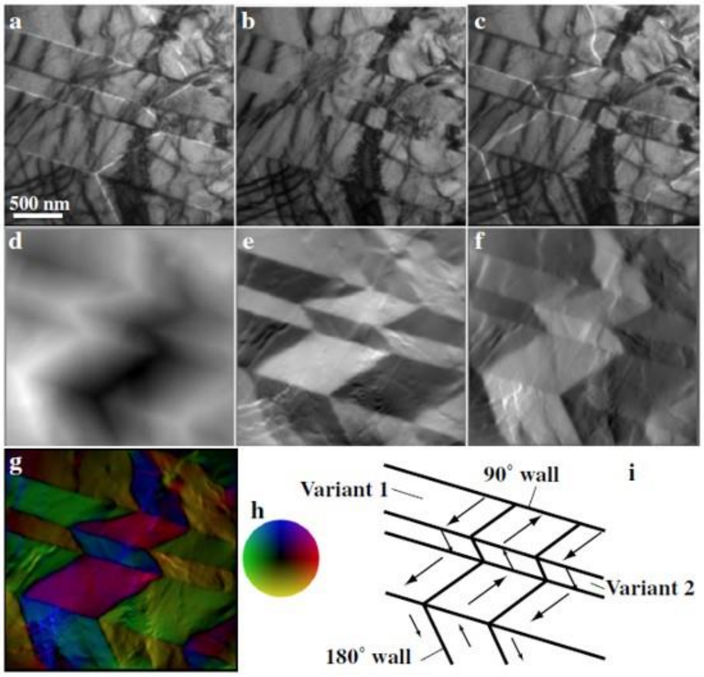

Figure 2-12 Martensite phase reconstruction of Ni_2MnGa. (a)-(c) are Fresnel images with twin boundaries and domain structures. (d)-(f) gray scale induction images that express magnetic field direction (g) color plot delineating domain walls (i) schematic of domain walls. Reprinted from Acta Materialia, 55, S.P. Venkateswaran, N.T. Nuhfer, and M. De Graef, Magnetic domain memory in multiferroic Ni2MnGa, pp 5, Copyright (2007), with permission from Elsevier [36].

twin boundaries is shown in Figure 2-12i. The 90° domain walls that separate the twin variants are oriented along different cubic axes and the 180° domain walls with a single variant contain two magnetic domains with the c-axis oriented in opposite directions.

2.8. Numerical Simulations

Y. M. Jin [14] discussed the role of twin boundary mobility on magneto-mechanical properties of MSMA with domain structure evolution through micromagnetics simulations. Jin illustrated the coupling of magnetic domain evolution and twin boundary motion in a martensite phase for a polycrystalline material by using phase field micromagnetics microelastic modeling. This modeling approach combined the phase model of tetragonal martensite and the uniaxial ferromagnetic polycrystal micromagnetics model. The mathematical calculations for the phase model and the polycrystal micromagnetics are described in [12]. The simulations started with an initial domain microstructure with a domain configuration that has the lowest energy state [14] i.e. martensite variants defined across a twin boundary (separated by 90º domain walls) and within these martensite variants were domain structures (separated by 180° domain walls). In Jin's work, different kinetic coefficients were used to alter the mobility of the twin boundary. Figure 2-13 demonstrates the evolution of domain structure of one such case where the kinetic coefficient = 0.2. The illustration shows the evolution of magnetization and strain response with time (t^* denotes time steps). In this simulation, the domain structures expand on one side of the twin boundary until the 180° domain walls annihilate, which result in a single domain state. While on the other side of the twin boundary, expansion in

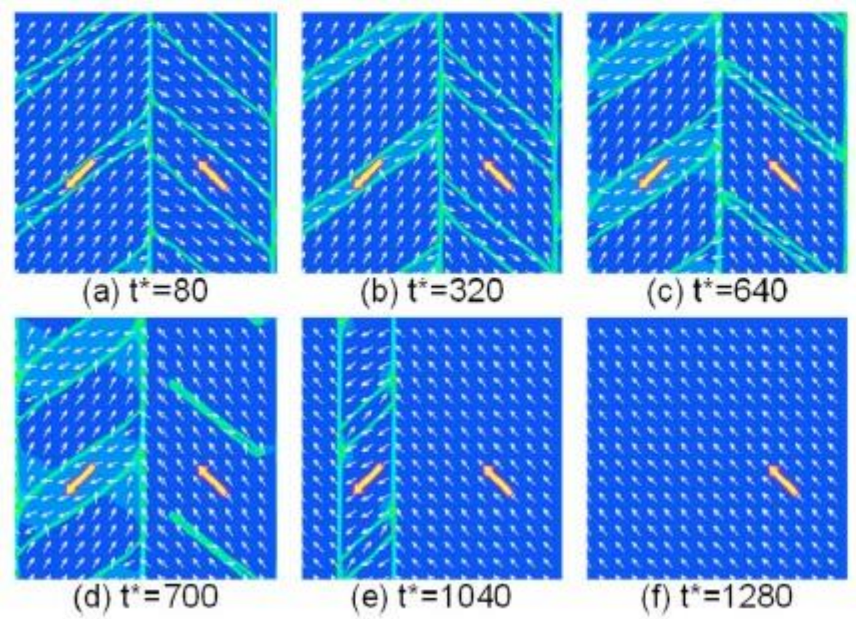

Figure 2-13 Illustration of magnetic domain structure evolution with time across a moving twin boundary. Reprinted from [Y. M. Jin, Effects of twin boundary mobility on domain microstructure evolution in magnetic shape memory alloys: Phase field simulation, Appl. Phys. Lett. 94, 062508, 2009] with the permission of AIP Publishing [14].

the 180° domains which is favorable by external field occurs, but subsequently shrinks (due to the internal field). This results in a multi-domain configuration. While this change in domain structure occurs, the twin boundary moves across and results in a final single state domain.

Phase-field models solve for free energy minimization that consider chemical energy, gradient energy, elastic energy, external mechanical energy, magnetocrystalline anisotropy energy, magnetostatic energy, exchange energy, exchange energy, and the Zeeman energy. The microstructure evolution that takes place while reaching equilibrium state follows Time-Dependent-Ginzburg-Landau kinetic equations. Using this type of phase-field simulation analysis, Peng *et al*. studied the martensitic microstructural evolution and evaluated various material characteristics of MSM alloys. Some of those are pseudoelastic stress-strain behavior [15], hysteretic magneto-mechanical behavior [39] and effects of demagnetization on magnetic-field-induced strain (MFIS) [13]. For studying the hysteretic magneto-mechanical behavior [39], they used the phase-field model with a friction- type resistance in the kinetic equation for the reorientation of martensite. This approach helped to better describe the hysteretic microstructure evolution and the associated responses under various quasi-static magneto-mechanical loading paths. In Peng's study, simulations were performed to characterize the microstructure evolutions at a constant compressive stress of 0, 1.5, and 2.5 MPa and stress induced microstructural evolution under a constant magnetic field of 0.05, 0.3, and 1T. The initial equilibrium configuration is a single variant (say variant I- blue regions in Figure 2-14) with the easy axis along the compressive stress. A magnetic field is applied along the easy axis of variant II (perpendicular to the compressive stress in Figure 2-14). In order to facilitate the nucleation of variant II (the red

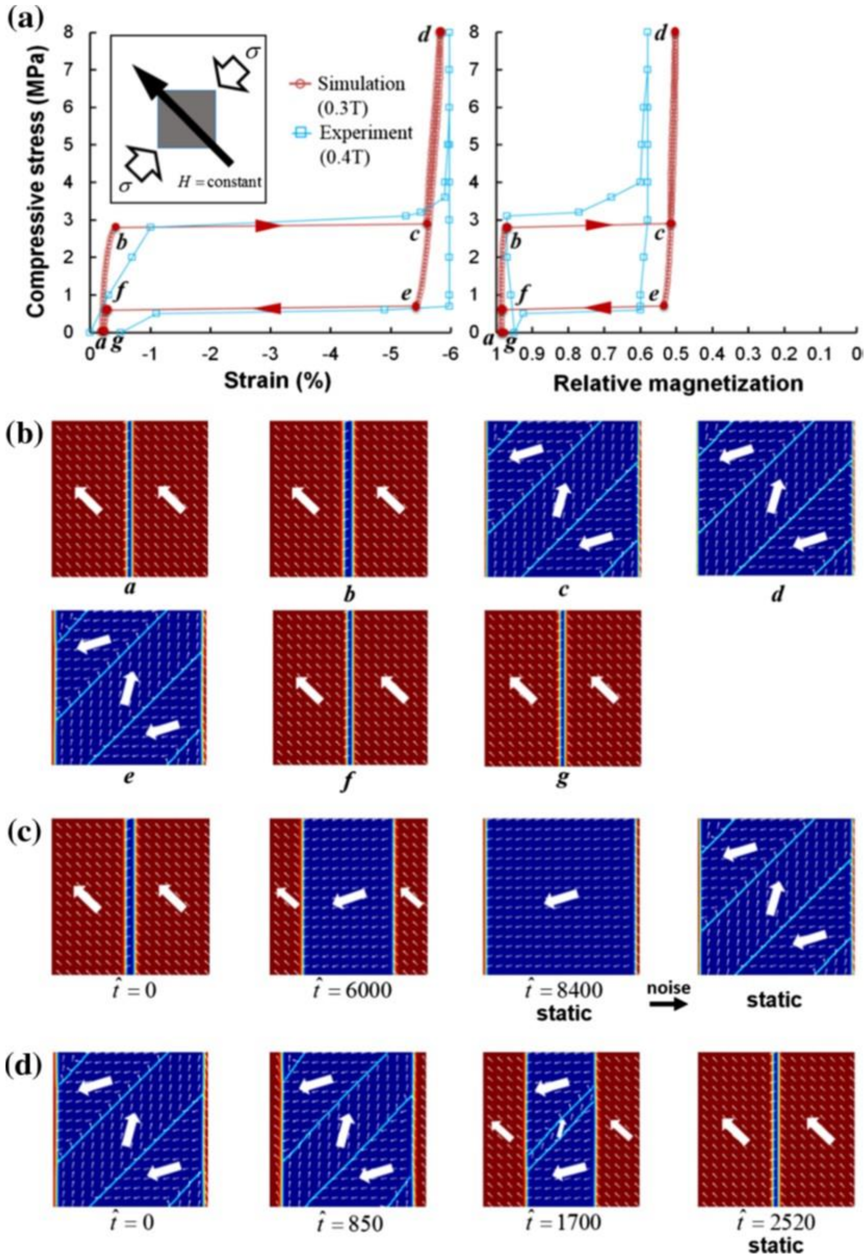

Figure 2-14 (a) Numerical calculations of strain and relative magnetization with increasing compressive stress at a constant bias magnetic field of 0.3 T (experimental at 0.4 T). (b) quasi-static microstructures (c) non equilibrium microstructural evolution with time for a forward martensite transformation (corresponding to b→c, in figure a) (d) non equilibrium microstructural evolution with time for a reverse martensite transformation (corresponding to e→f, in figure

a). Reprinted from Acta Materialia, 88, Q. Peng, Y.J. He, and Z. Moumni, A phase-field model on the hysteretic magneto-mechanical behaviors of ferromagnetic shape memory alloy, pp 20, Copyright (2015), with permission from Elsevier [39].

regions) during the magnetic field loading, one layer of variant II is put into the middle column of the simulated mesh grids. Similarly, one layer of variant I is put into the first column of the mesh grids to facilitate the reverse martensite reorientation during the unloading process. Figure 2-14 shows the martensitic reorientation and the comparison between experimental and simulated stress strain behavior with a magnetic field of 0.3 T perpendicular to the loading direction. In this case, when the compressive stress increases to 2.9 MPa (states “b”–“c” in Figure 2-14a) the strain which is related to martensite reorientation (variant II (Red) to I (Blue)) and the relative magnetization experience a sudden change. From states “c”–“e” in Figure 2-14b, it is observed that the magnetization vectors in the variant I (stress-preferred variant) are not aligned with the easy axis of the variant and their corresponding relative magnetizations are about 0.5 (relative magnetization in Figure 2-14a). During unloading, as the compressive stress is decreased to 0.6 MPa reverse martensite reorientation (variant I to II) takes place (states “e”–“f” in Figure 2-14b). The nonequilibrium microstructure evolutions of the forward (Variant II to variant I) and reverse (Variant I to Variant II) martensite reorientations are shown in Figure 2-14c and Figure 2-14d, respectively. It is observed that the stress preferred (during forward martensite reorientation or loading) and field-preferred (during reverse martensite reorientation or unloading) variants grow via twin boundary motion and domain wall motion. The stress plateaus during the loading (2.9 MPa) and unloading (0.6 MPa) processes form a rate-independent hysteresis. Using such a simulated data, phase diagrams of martensite variants for various compressive stresses and magnetic fields were constructed and reported.

In a Ni-Mn-Ga alloy, when a mechanical test is performed at certain constant magnetic fields, while unloading, only a portion of the strain (in loading) is recovered. In order for N-Mn-Ga alloys to perform with maximum efficiency for sensor applications, it needs to be completely pseudoelastic (because the magnetization or flux density returns to its initial value only if the stress-strain curve exhibits complete pseudoelasticity [2][15]). Furthermore, it was found that the demagnetization factor i.e. specimen geometry factor, also influences the magnitude of strain reversal. Therefore, using phase-field simulations, the dependence of the partial pseudoelastic stress-strain behavior on the constant field and the demagnetization factor was evaluated by Peng *et.al*. [15]. They concluded that while under compressive loading and unloading, the demagnetization factor component that is parallel to the applied magnetic field significantly effects the partial strain recovery, but the component which is parallel to the compressive stress has no effect. It was also observed that the recoverable strain can be increased by either increasing the magnetic field or by reducing the demagnetization component which is parallel to the magnetic field.

The effect of various demagnetization factors on MFIS and microstructural evolution in Ni-Mn-Ga alloys has been studied using phase-field simulations [13]. The twin boundary movement and the magnetic domain evolution depend on the component of the demagnetization factor that is parallel to either the favored martensitic variant or the unfavored martensitic variant. It was observed that the velocity of the magnetic domain wall during the MFIS process decreases with increasing the component of demagnetization factor that is parallel to the unfavored martensitic variant. The microstructural evolution corresponding to a minimum demagnetization effect and a maximum demagnetization effect along the favored variant is shown in Figure 2-15a and Figure 2-15b respectively. In Figure 2-15, the regions separating the two variants (variant I in blue and variant II in red) is the twin boundary and the lines that are diagonal to the sample are the magnetic domain boundaries. In the low demagnetization factor case (i.e. Figure 2-15a) the field favored variant II (red regions) grow at the expense of

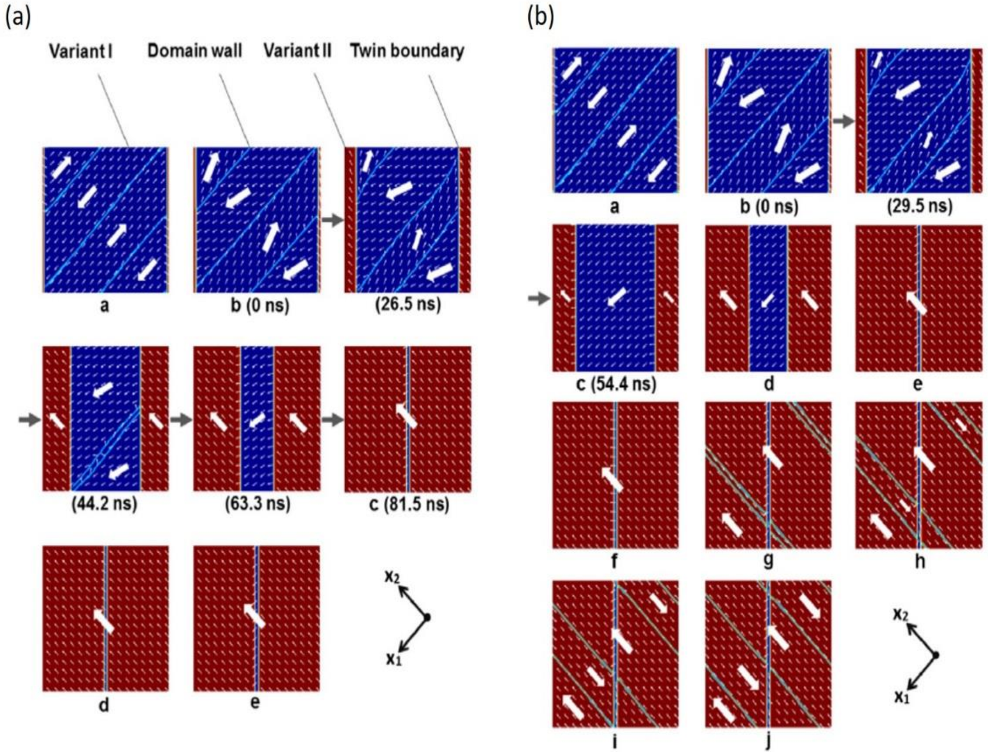

Figure 2-15 (a) Quasi-static state microstructures and (b) non-equilibrium microstructural evolution with time during MFIS. Blue regions correspond to martensite variant I, Red regions correspond to martensite variant II, Vertical lines correspond to twin boundaries separating variant I and variant II, Cyan lines correspond to magnetic domain walls. Reprinted from Materials & Design, 107, Q. Peng, J. Huang, and M. Chen, Effects of demagnetization on magnetic-field-induced strain and microstructural evolution in Ni-Mn-Ga ferromagnetic shape memory alloy by phase-field simulations, pp 365 & 367, Copyright (2016), with permission from Elsevier [13].

field un-favored variant I (blue regions) by twin boundary motion. From the calculations it was concluded that the switching field increased with increasing demagnetization factor (along the favored variant). Because, as the demagnetization factor is higher the demagnetization field at the onset of MFIS is larger in the direction opposite to the applied magnetic field. Therefore, higher magnetic fields are required for the initiation of MFIS.

Using micromagnetics numerical calculations, A. Hobza *et al.* [18] studied the contribution of different magnetic energies to torque as a function of the orientation of the specimen in the magnetic field for two different twin microstructures. Figure 2-16a gives the change in energy as a function of angle (magnetic field with respect to specimen) for the ABA and BAB microstructures (A and B denote twin orientations with the axis of easy magnetization parallel and perpendicular to longest sample edge). The BAB microstructure

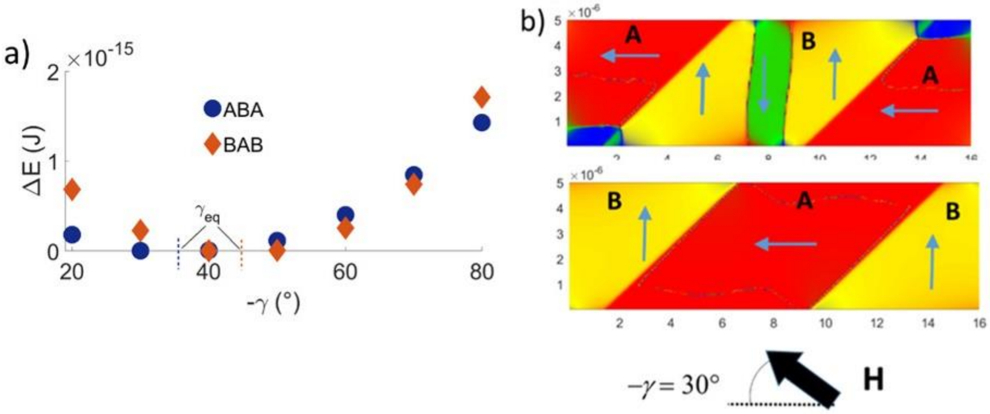

Figure 2-16 (a) Change in total energy as a function of magnetic field angle for ABA and BAB. (b) ABA and BAB equilibrium magnetic domain structures at -γ = 30º. Reprinted from Journal of Magnetism and Magnetic Materials, 458, A. Hobza, C. J. García-Cervera, P. Müllner, Twin-enhanced magnetic torque, pp 189, Copyright (2018), with permission from Elsevier [18].

resulted in a smaller total energy but the energy increased more quickly away from the minimum energy resulting in a larger torque. While experimental and numerical results differ quantitatively by about 50%, both show the same dependence of the torque on the twin microstructure. The equilibrium magnetic structure for ABA contained 180° magnetic domain walls in both A and B twin domains, while the twin domains in the BAB microstructure were fully saturated.

CHAPTER THREE: MOTIVATION

The discovery of MFIS generated immense interest in studying MSM alloys (especially Ni-Mn-Ga single crystals) and evoked the development of MSM for various applications such as actuation [1,4,10,40–44], sensing [40,45,46], and power harvesting [2,47–52]. The research in this field is widely distributed with research groups (e.g. [14,33,51,53]) characterizing MSM properties such as MFIS, twin boundary mobility, power efficiency, magnetic domain evolutions etc. In this dissertation, we performed micromagnetics simulations to analyze the magnetic energy distributions to understand the mechanisms with which internal magnetic structures and their interactions impact the magnetic, mechanical, and magneto-mechanical properties of MSM alloys. This study concentrates on evaluating three different magneto-mechanical properties of MSM alloys, which are discussed in detail in the following chapters (Chapter Five, Chapter Six and Chapter Seven). As a result of this research, I will publish three first author papers. Some of these results were presented at the 16th International Conference on New Actuators, 2018 and at the International Conference on Ferromagnetic Shape Memory Alloys, 2019.

In Chapter Five (i.e. "Sensitivity of twin boundary movement to sample orientation and magnetic field direction in Ni-Mn-Ga" submitted on July 19, 2019 for publication in Acta Materialia), we studied the magnetic domain structures and the magnetic energies associated with these structures to benefit the designing strategies of MSM actuators. The magnetic response of an MSM alloys is directly associated with twin boundary movement. Depending on the direction of the magnetic field with respect to the sample orientation, the material responded abruptly (when the magnetic field was parallel to the long axis of the sample) or gradually (when the magnetic field was perpendicular to the long axis of the sample). We studied this dependency experimentally and with numerical simulations. My contributions to this study were the magnetic characterization experiments and micromagnetics simulations and their evaluation.

In Chapter Six (i.e. “Magnetic domain-twin boundary interactions in Ni-Mn-Ga” submitted on September 11, 2019 for publication in Acta Materialia), the magnetic and microstructural interactions that effect the mechanical behavior of MSM alloys were studied. Straka *et. al.* [54] found that by varying the twin density (single twin boundary and fine twins), the mechanical properties of the MSM alloy varied. Also, Perevertov *et. al* [55] and Heczko *et. al*. [27] reported microscopic images of densely packed twin boundaries interacting with magnetic domains that are magnetized away from the *c*-axis (Figure 3-1). In this study, we evaluated the effect of the magnetic domains that result in

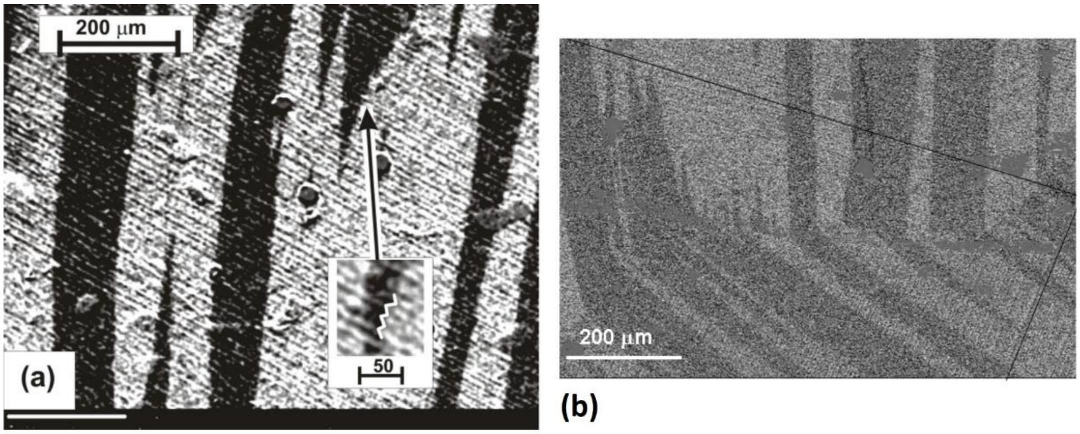

Figure 3-1 Experimental microscopic images showing the interaction of fine twins and magnetic domains. (a) Reprinted (figure) with permission from [O. Perevertov, O. Heczko, and R. Schafer, Phys Rev B, 95, 144431-3, 2017] Copyright (2019) by the American Physical Society [55] (b) Copyright (2017) by IEEE [27].

magnetoelastic defects and their effect on mechanical properties. My contributions to this work were the micromagnetics simulations and their evaluation.

In Chapter Seven (i.e. “Asymmetric properties of energy conversion in Ni-Mn-Ga with biased field orientation” to be submitted), the power generation capabilities of MSM alloys in an inclined biased magnetic field was investigated. Combining MFIS with the inverse magnetoplastic effect in a biased magnetic field, Ciocanel *et al.* [49] showed an increase in electrical power output in MSM when the biased magnetic field was inclined to the loading direction. We performed experiments and numerical calculations to analyze the asymmetrical behavior of power output in an inclined magnetic field at lower magnetic fields.   For this study, I conducted the experiments, along with Dr. Paul Lindquist and also performed the micromagnetics simulations, which I also evaluated.

CHAPTER FOUR: MICROMAGNETISM METHODOLOGY- A NUMERICAL APPROACH TO STUDY THE EVOLUTION OF MAGNETIC DOMAINS

This section presents the general methodological approach for performing micromagnetics simulations for the three cases presented in Chapter Five, Chapter Six, and Chapter Seven. The details of the numerical approach that we applied to evaluate the magnetic domain structures and their energies are described here. The response of a magnetic material to an external magnetic field depends on the magnetic structure and the relaxation mechanisms of that structure. The magnetic domain structure minimizes the magnetic energy. The minimum energy state results from the contribution of four distinct magnetic energies as described section 2.2 (pages 7-9). Micromagnetics is the detailed study of the magnetic domain structure with respect to the equilibrium energy on a micrometer length scale. This growing field of study was pioneered by Brown [56] in 1937 and presently, in extension to this work and with the use of fast computational approaches, in-depth characterization of magnetic structures has been achieved.

4.1 Methodology

4.1.1. Grid definition

The interplay of the four energy terms discussed in section 2.2, govern the formation of a magnetic domain structure. Domains are homogeneously magnetized regions separated by domain walls. In Ni-Mn-Ga, the domain wall width is about 12 nm [8]. We choose a cell size of 4 nm x 2 nm in the *x* and *y* directions to provide a few cells per cell wall width and at the same time to allow simulating a volume large enough to include multiple twin boundaries.

In these calculations, a high density of magnetic moments were defined such that there is an adequate number of moments to show the rotation of magnetic moments near transition regions. This dense structure definition required 384 magnetization vectors in the *x* direction and 192 vectors in the *y* direction. The sample size used for these numerical calculations in each of the cases is 1.6 µm x 0.52 µm x 0.36 µm (in x, y, and z) at 3% strain. All the numerical calculations have the same defined initial magnetic state, such that each component of the magnetic vector in the *x*, *y*, and *z* direction is the same and the magnitude of the normalized magnetic vector is unity. The energy minimization ran over 20,000 iterations for a fixed real time interval of 0.2 ns. An equilibrium magnetic structure with magnetic moments is obtained for each energy minimization calculation, which shows the evolution of the magnetic domain for different experimental conditions. This description of the numerical calculation holds good for all the below described cases.

Table 1 Constants used for running the micromagnetics simulations for Ni-Mn-Ga

Constant	Abbreviation	Value	Composition	Reference
Saturation magnetization	M_s	0.61 T	$Ni_{51.3}Mn_{24}Ga_{24.7}$	[57]
Exchange interaction	C_{ex}	6×10^{-12} J/m	$Ni_{49.1}Mn_{29.4}Ga_{21.5}$	[58]
Magnetocrystalline anisotropy	K_u	2.45×10^{5} J/m^3	$Ni_{50.5}Mn_{30.4}Ga_{19.1}$	[59]

With the parameters listed in Table 1, a simulation was conducted on a sample with 3% strain. A single twin boundary was defined in the sample such that the twin boundary makes 45º angle with respect to the length of the sample. The direction of the applied magnetic field was along the long axis of the sample, shown in Figure 0-1. The simulated equilibrium domain structure was obtained for this sample configuration. Each of the colors in this plot denote the predominant direction for the magnetic moments, yellow for upward, green for downward, red for to the left, and blue for to the right (not present in this figure). Selected regions of the twin boundary with 90º domain walls and a 180º domain wall interfaces are magnified in the vector plots. The vector plots show the evolution of domain structure across transition regions with 90° and 180° domains walls.

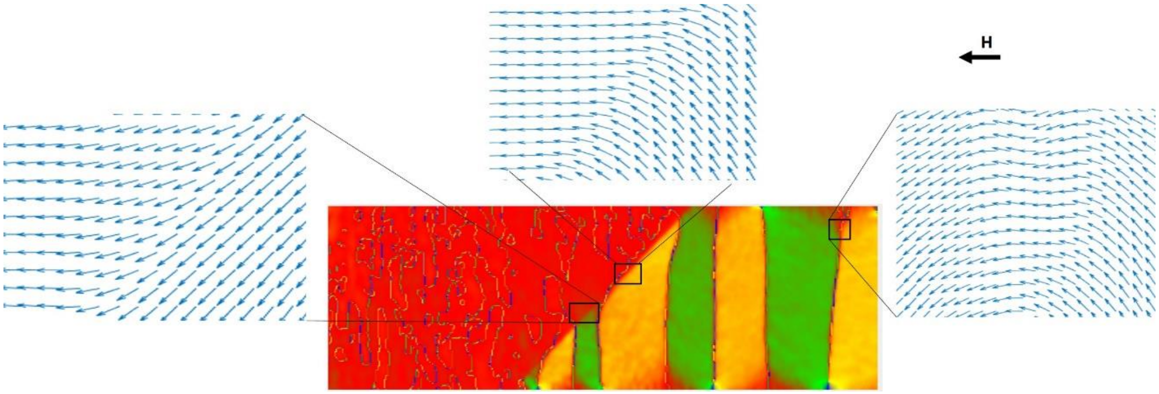

Figure 0-1 Color plot of a micromagnetics simulation for a specimen with a single twin boundary, strained to 3%. The vector plots indicate the direction of magnetization at transition regions (marked square boxes). Direction of external applied magnetic field H is indicated by the black arrow.

4.1.2. Governing equations

The code applied in this study solves the Landau-Lifshitz-Gilbert equation [30]:

$$d\mathbf{M}(\mathbf{r})/_{dt} = -\left(\mu_0\gamma/_{M_s}\right)\mathbf{M}\times\mathbf{H} - \alpha\left(\mu_0\gamma/_{M_s}\right)\mathbf{M}\times[\mathbf{M}\times\mathbf{H}] \tag{10}$$

where $\mathbf{M}(\mathbf{r})$ is the magnetization density at point r, $M(\boldsymbol{r})$ is its modulus, γ is a gyromagnetic ratio, α is the dimensionless damping parameter, and **H** is the effective vector magnetic field, which is the derivative of total energy with respect to magnetization.

$$\mathbf{H} = -\frac{\delta E}{\mu_0 \delta \mathbf{M}} = -\left({}^{2K_u}\!/_{\mu_0 M_s^2}\right)(M_2 e_2 + M_3 e_3) + \left({}^{2C_{ex}}\!/_{\mu_0 M_s^2}\right)\Delta\mathbf{M} - \nabla\mathbf{U} + \mathbf{H}_{\text{ext}} \tag{11}$$

Where E is the total magnetic energy, K_u is the anisotropy constant, M_s is the saturation magnetization, M_2 and M_3 are magnetization components that are orthogonal to the axis of easy magnetization, e_2 and e_3 are axis directions in which the magnetization is not spontaneous, C_{ex} is the exchange constant, $\Delta\mathbf{M}$ is the square of the gradient of magnetization, μ_o is magnetic permeability of free space, $\mathbf{H}_{ext}$ is the external magnetic field.

4.1.3. Energy minimization

While conducting the simulations, the amount of time required to attain an equilibrium state varied from experiment to experiment. The code was designed such that each simulation test runs for 20,000 iterations. However, it was found that more time/iterations were required to obtain an energy minimum. In this research, a minimum of 180,000 (i.e. 9 hours) iterations and a maximum of 380,000 iterations (i.e. 19 hours) were conducted for each data point obtained via numerical calculations. For the results shown in Chapter Five and Chapter Six, the energy minimization was obtained by including angle sweeps about 0°/ 90° (i.e. 360°-0°-10°/80°-90°-100°, since the experiment was conducted with magnetic fields oriented at 0° and 90°). For Chapter Seven, a certain field direction/angle was repeated to make a total of 180,000 iterations. This is because the magnetic field orientation varied by only 3° from experiment to experiment (e.g. 75°, 77°, 79°,). Figure 0-2b is a plot of Energy as a function of number of iterations for an experiment that attained equilibrium state (The lowest energy value stabilizes and remains constant at the end of the experiment). In some cases, e.g. in Chapter Seven, at lower field magnitudes, the energy did not reach its equilibrium state. Figure 0-2a shows the plot of Energy as a function of number of iterations for an experiment that did not reach an equilibrium state (The lowest energy value is still not attained since the slope of the energy curve has a negative slope at the end of the experiment).

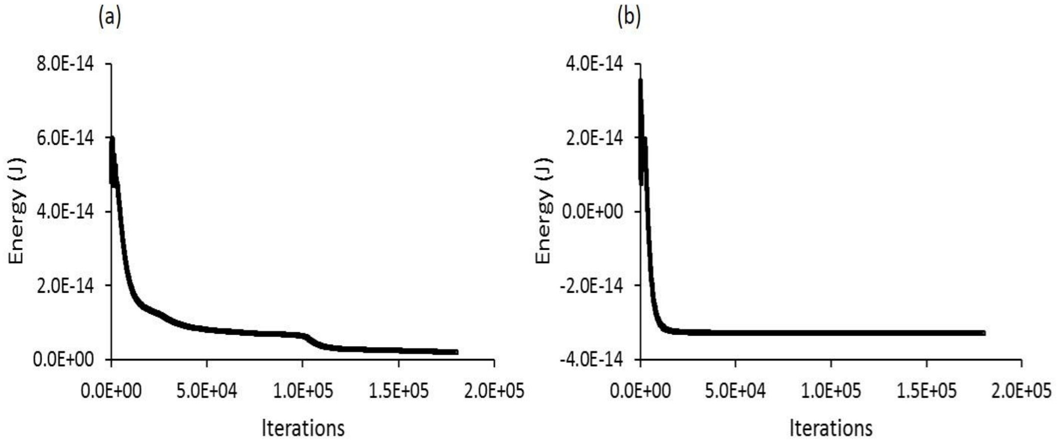

Figure 0-2 Energy as a function of number of iterations for cases (a) non-equilibrium state and (b) equilibrium state.

CHAPTER FIVE: SENSITIVITY OF TWIN BOUNDARY MOVEMENT TO SAMPLE ORIENTATION AND MAGNETIC FIELD DIRECTION IN NI-MN-GA

Medha Veligatla[1]

Christian Titsch[2]

Welf-Guntram Drossel[2,3]

Carlos J. García-Cervera[4,5]

Peter Müllner[1]

[1] Micron School of Materials Science and Engineering, Boise State University, Boise, ID, 83725, USA

[2] Institute for Machine Tools and Production Processes, Technische Universität, 09126 Chemnitz, Germany

[3] Fraunhofer Institute for Machine Tools and Forming Technology, 09126 Chemnitz, Germany

[4] Deparment of Mathematics, University of California, Santa Barbara, CA, 93117, USA

[5]Visiting Professor at BCAM – Basque Center for Applied Mathematics, Bizkaia, Spain

Keywords: Ni-Mn-Ga, micromagnetics, actuators, magnetic energy density

Submitted to Acta Materialia on July 19, 2019 and is under review

5.1 Abstract

When applying a magnetic field parallel or perpendicular to the long edge of a parallelepiped Ni-Mn-Ga stick, twin boundaries move instantaneously or gradually through the sample. We evaluate the sample shape dependence on twin boundary motion with a micromagnetics computational study of magnetic domain structures and their energies. Due to the sample shape, the demagnetization factor varies with the direction of the external magnetic field. When the external magnetic field is applied perpendicular to the long edge of the sample, i.e. in the direction in which the demagnetizing field is highest, the magnetic energy intermittently increases when the strength of the applied magnetic field is low. This energy gain hinders the twin boundary motion and results in a gradual switching, i.e. a gradual magnetization reversal as the applied magnetic field is increased. The formation of 180° magnetic domains offsets this effect partially. In contrast, when the applied magnetic field is parallel to the long edge of the sample, i.e. in the direction in which the demagnetizing field is lowest, the energy decreases with each subsequent magnetization domain reversal and the twin boundary moves instantaneously with ongoing switching. The actuation mode with the field parallel to the long sample edge lends itself for on-off actuators, whereas the actuation mode with the field perpendicular to the long sample edge lends itself to gradual positioning devices.

5.2 Introduction

Macroscopic deformation in magnetic shape memory (MSM) alloys occurs when the material is subjected to an external magnetic field or a mechanical stress. Lattice reorientation via twinning in the martensite phase causes this shape change. An MSM single crystal with one twin boundary consists of two twin domains sharing the boundary.

These twin domains have different magnetization and crystallographic orientations [5,57]. Depending on the direction of the external magnetic field, one variant grows at the expense of the other as the twin boundary moves along the sample. The maximum magnetic-field-induced strain depends on the martensite structure and lattice parameters and varies between 6 and 12% [5,6,8,60] . With a few microseconds response time [61], these materials have great potential as actuators. Numerous research groups have studied the material properties of Ni-Mn-Ga single crystals and their response to variable magnetic fields to improve the performance of MSM actuators [33,41,42,62–66].

In 1995, Ullakko [4] introduced the concept of using magnetic field induced reorientation of martensite variants for magnetically powered actuators. Ullakko suggested that with several percent strain and rapid control, the magnetic shape memory alloys may outperform piezoelectric and magnetostrictive materials. Subsequently, Ullakko *et al.* demonstrated deformation in Ni_2MnGa with magnetic fields [67]. In 2004, Suorsa *et al*. [1] measured various properties that determine the dynamic behavior of a 10M Ni_2MnGa MSM material. For a sample dimension of 1 mm x 2 mm x 10 mm, the authors reported the acceleration of the sample surface, rise time and actuation velocity to be 5000 m/s^2, 0.2 ms and 1.3 m/s respectively. The switching behavior of the material dictates the response of the actuator. Recently, Saren *et al*. [61] and Smith *et al*. [68] reported twin boundary velocities of 39 and 82 m/s, implying actuation speeds of 2.4 and 4.8 m/s. Pagounis *et al*. summarized some recent progress on MSM actuators [43].

The goal of this paper is to study extrinsic factors that influence twin boundary motion in MSM actuators. We apply experimental and numerical methods to Ni-Mn-Ga single crystals in a magnetic field to study the macroscopic response via twin boundary movement and their corresponding mesoscopic magnetic energies. We are particularly interested in the response of the material when exposed to magnetic fields in different directions, namely parallel and perpendicular to the long sample axis. While we performed switching field tests to demonstrate the macroscopic magnetic response, the micromagnetics simulations were carried out to demonstrate the mesoscopic magnetic interactions.

5.2.1. Micromagnetics

The field of micromagnetics was pioneered by Brown [56] and a comprehensive review was presented by Chantrell *et al.* [69]. Many research groups have used micromagnetics to characterize the mesoscale magnetic properties of Ni-Mn-Ga alloys [12–15,39,70–72]. The theory of solving the Landau-Lifshitz dynamic equation was applied with various methods, such as phase field modeling [12–15,39,73]. This method has been used to study the twin boundary mobility[14], magnetic domain evolutions [73], demagnetization effects [13], and magneto-mechanical properties[15,39] of Ni-Mn-Ga. These research groups studied the magnetic domain evolution as the twin boundary moves along the sample length. In the present study, we simulate the magnetic domain structures for samples with one twin boundary inclined at 45° to the sample edge. For each state, the position of the twin boundary is predetermined and fixed. We do not assess the twin boundary nucleation phase. The magnetic structures start with an initial condition where the sum of magnetization in the x, y, and z direction is unity and evolve to a minimum energy state with respect to time. The position of the twin boundary was determined by the strain on the sample i.e. the fraction $f_{\parallel}$ of region with the *c*-axis (axis of easy magnetization) parallel ($f_{\parallel}$) and perpendicular ($f_{\perp} = 1 - f_{\parallel}$) to the sample length was determined by the strain ε on the sample: $\varepsilon = f_{\dashv}(1 - {}^{c}/_{a})$, where a and c are the lattice parameters. Therefore, the position of the twin boundary changes with increasing strain on the sample and the *c*-axis across this twin boundary is nearly perpendicular. The location of the twin boundaries are defined fixed by the strain value. Thus, we simulate for a static twin boundary condition at various strains steps that correspond to elongation from 0 to 6% and to compression from 6 to 0% with 0.5% increments. We neglect twin boundary mobility. This allows us to study the interactions of magnetic domains and twin boundaries in greater detail at equilibrium conditions. Hobza *et al*. applied a code developed by Garcia-Cervera [74] to study the torque generated by a magnetic field on Ni-Mn-Ga samples with various twin microstructures [18,70]. This code evaluates the actual dynamics (Landau-Lifshitz equation). In our method, we only solve linear systems of equations with constant coefficients. The cost per step of our method is O(N log N), where N is the number of cells. Using this code, we obtained magnetic energies for magnetic equilibrium structures that summarize the switching behavior for a single twin boundary system in Ni-Mn-Ga. We mapped the different energy contributions in the process of magnetic domain evolution. In order to qualitatively compare these energies, the simulations were arranged such that they replicate the experimental setup of a switching field test at small scale. The equilibrium magnetic structures and energies obtained through these simulations take into account the anisotropy, exchange, Zeeman, and stray field energies. The code solves the Landau-Lifshitz-Gilbert equation to approach the minimum energy state:

$$ {}^{d\mathbf{M}(\mathbf{r})}/_{dt} = -\mu_0\gamma\,\mathbf{M}\times\mathbf{H} - \alpha\left({}^{\mu_0\gamma}/_{M_s}\right)\mathbf{M}\times[\mathbf{M}\times\mathbf{H}] \qquad \text{(equ. (10) in 4.1.2)} $$

where $\mathbf{M}(\mathbf{r})$ is the magnetization density at position $\mathbf{r}$, γ is a gyromagnetic ratio, α is the dimensionless damping parameter, and $\mathbf{H}$ is the effective local magnetic field vector, which is the negative derivative of total energy with respect to magnetization:

$$\mathbf{H} = -\frac{\delta E}{\mu_0 \delta \mathbf{M}} = -\left({}^{2K_u}\!/_{\mu_0 M_s^2}\right)(M_2 e_2 + M_3 e_3) + \left({}^{2C_{ex}}\!/_{\mu_0 M_s^2}\right)\Delta\mathbf{M} - \nabla\mathbf{U} + \mathbf{H}_{\text{ext}}$$

(equ. (11) in 4.1.2)

where K_u is the anisotropy constant, M_s is the saturation magnetization, M_2 and M_3 are magnetization components that are orthogonal to the axis of easy magnetization, e_2 and e_3 are axis directions in which the magnetization is not spontaneous, C_{ex} is the exchange constant, μ_o is magnetic permeability of free space, and $\mathbf{H}_{\text{ext}}$ is the external magnetic field.[1] The individual summation terms in equation (2) are the energies associated with magnetocrystalline anisotropy, exchange interaction, stray field, and external applied field (Zeeman energy). In short, the magnetocrystalline energy is the energy associated with the orientation of magnetic domains with respect to the axis of easy magnetization, the exchange energy is the short range interaction energy between neighboring magnetic moments, and the stray field and Zeeman energies are associated with magnetic domain splitting and the external magnetic field respectively. Hobza *et al*. provide a detailed description of these energy terms and the micromagnetics code [70].

5.3 Experiments and Simulations

All the experiments were conducted on a Ni-Mn-Ga single crystal with 10M martensite structure and composition $Ni_{49.5}Mn_{28.8}Ga_{21.7}$ (Goodfellow). A rectangular sample with dimensions 3.93 mm x 2.86 mm x 1.06 mm was cut with all faces parallel to {100}. X-ray diffraction and energy dispersive X-ray spectroscopy were done with a

---

[1] Equations 1 and 2 are given in SI units and differ from those given in Ref. [74].

Bruker D8 Discover diffractometer and a Hitachi S-3400N-II scanning electron microscope equipped with an Oxford Instruments Energy EDS to confirm the crystal structure and the composition. Magnetic switching field experiments were conducted with an ADE model 10 vibrating sample magnetometer (VSM). For the VSM experiments, the sample was mounted to a quartz tube and exposed to an increasing magnetic field. The experiment were done with two configurations, namely such that the magnetic field was parallel to the longest (designated "parallel") and the intermediate (designated "perpendicular") edge of the sample. First, the sample was placed in the field with the parallel sample configuration. The field was increased from 0 to 1.2 T to fully saturate the sample and then reduced to 0 T. Then, the electromagnet was rotated such that the sample was in the perpendicular configuration. In this setup the field was increased from 0 to 1.2 T and reduced to 0 T. Then the magnet orientation was rotated back to the parallel configuration. We conducted 6 experiments with alternating parallel and perpendicular configurations and measured the magnetization as a function of magnetic field strength. At the beginning of the experiments in the parallel and perpendicular configurations, the sample starts with fully extended (6% strain) and fully compressed (0% strain) states, respectively.

We conducted micromagnetics simulations to assess the equilibrium magnetic structure and to calculate the magnetic energies of Ni-Mn-Ga samples for magnetic fields in the parallel and the perpendicular configuration and for various deformation states. The strain was varied from the fully compressed state (i.e. 0%) to the fully elongated state (i.e. 6%) in increments of 0.5%. The sample dimensions used for simulating 0% and 6% correspond to 1.55 μm x 0.53 μm x 0.36 μm (L x W x t) and 1.64 μm x 0.50 μm x

0.36 µm (*L* x *W* x *t*). The length (*L*) and width (*W*) of the sample were varied with respect to the strain while the thickness (*t*) was kept constant. The sample dimensions corresponding to each strain are given in Table 1 in the Appendix A. A twin boundary at 45° to the sample edge was introduced when the strain was varied from 0.5 to 5.5 %. The position of the twin boundary was determined by the strain on the sample i.e. the fraction of region with the *c*-axis (axis of easy magnetization) parallel and perpendicular to the sample length was determined by the strain on the sample (APPENDIX A, Table A-1). The entire simulation had 73,728 cells, defined such that 384 were along the longest sample dimension and 192 were along the intermediate dimension. Thus at 3% strain, each cell size along the long and intermediate dimensions were 4.17 nm and 2.70 nm respectively. Each simulation ran for 20,000 iterations. To obtain a magnetic structure with minimum energy configuration, we added multiple runs that continued from the previously ended run. In total, we did 380,000 iterations for each simulation condition to obtain the minimum energy state. Simulations were conducted at 100 mT, 150 mT, 200 mT, 250 mT, and 300 mT for all strain values. The direction of the magnetic field was applied parallel and perpendicular to the longest dimension of the sample (Figure 0-1). Figure 0-1a and Figure 0-1b illustrate the initial sample size and the direction of the magnetic field for perpendicular (fully compressed to 0% strain) and parallel (fully elongated to 6 % strain) sample configurations. The lines inside these rectangular schematics marked as ‘c’ represent the orientation of the axis of easy magnetization in their fully compressed and elongated states.

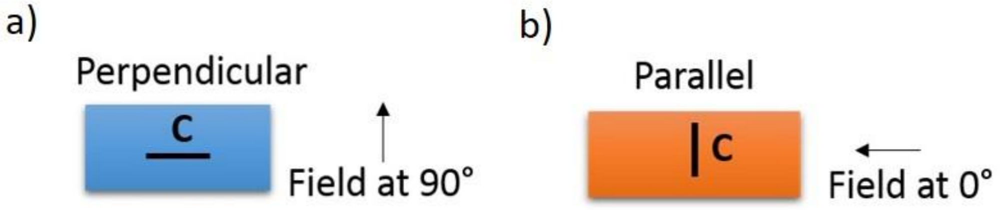

Figure 0-1 Schematics of samples used for micromagnetics simulations and experimental set up with respect to magnetic field. The direction of magnetic field is indicated by the arrows. (a) Initial sample dimension for perpendicular sample configuration: starting with fully compressed (0% strain) sample and (b) initial sample dimension for parallel configuration: starting with fully elongated (6% strain).

5.4 Results

The results of the VSM switching field experiments in the parallel and the perpendicular sample configuration are shown in Figure 0-2. The plot is a record of magnetization *vs* external magnetic field $\mu_0 H$.For the sample setup with the parallel configuration, the magnetization increased linearly until 0.4 T, followed by a sudden rise

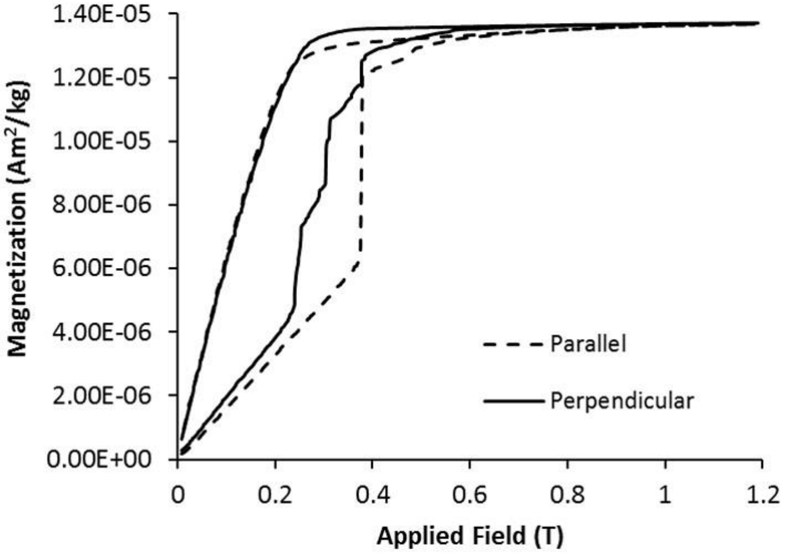

Figure 0-2 Switching behavior of $Ni_{49.5}Mn_{28.8}Ga_{21.7}$. The curves represent the change in magnetization as a function of applied magnetic field for magnetic fields applied in different directions. The dotted and solid curves correspond to perpendicular and parallel sample configurations.

to near saturation. The quick and complete rise indicates that twinning occurred throughout the entire sample. (This event is often referred to as switching.) For the sample setup with the perpendicular configuration, the increase in magnetization up to saturation occurred gradually over multiple small steps from 0.25 T to 0.38 T.

Figure 0-3 is a plot of numerically calculated magnetic energy densities with respect to sample deformation at various magnetic fields for the parallel configuration. In this setup, since we started the experiment with a fully elongated sample, the deformation started at 6% and proceeded to 0% and the energy density decreased monotonically with deformation. With an increasing magnetic field, the slope magnitude increased.

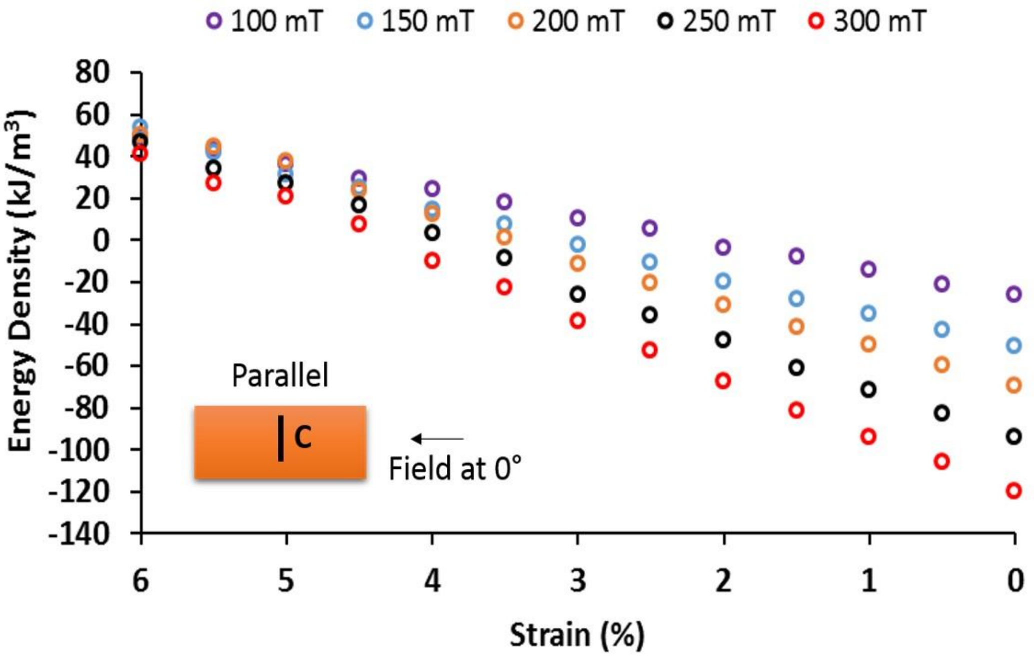

Figure 0-3 Numerical calculation of magnetic energy densities for different strains in parallel sample configuration. The energy densities are plotted against sample deformation as they occur during an experiment (i.e. starting from fully elongated to fully compressed). The inset shows a sample with the direction of easy magnetization (represented by c) and the orientation of the external magnetic field.

Figure 0-4 is a plot showing the numerically calculated magnetic energy densities with sample deformation at various magnetic fields for the perpendicular configuration, starting from the fully compressed state (i.e. 0% strain). The strain on the abscissa goes from 0 to 6%. At 100 mT, with increasing strain, the energy density decreased initially, went through a local minimum, then increased and went through a local maximum before it decreased again. At 150 mT, with increasing strain, the energies decreased with a steeper slope compared to when the field was at 100 mT. Then the slope flattened with increasing strain and went through a subtle minimum at 5% strain and a subtle maximum at 5.5% strain. We call this localized increase in energy during elongation as local

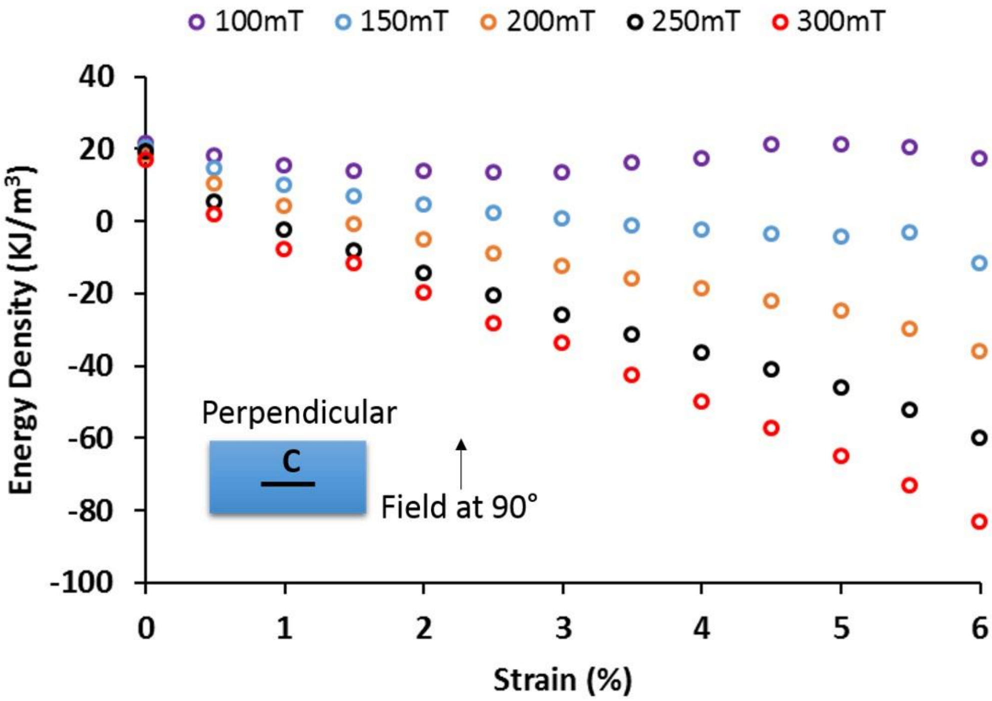

Figure 0-4 Numerical calculation of magnetic energy densities for a function of strain in perpendicular sample configuration. The energy densities are plotted against sample deformation as they occur during an experiment (i.e. starting from fully compressed to fully elongated). The figure inset shows a sample with the direction of easy magnetization (represented by c) and the orientation of the external magnetic field.

maxima. Following the local maxima, the energy again decreased.. Therefore, the local energy maximum was between 4.5 and 5% strain for 100 mT and at 5.5% strain for 150 mT. At magnetic fields equal to or larger than 200 mT, the energy density decreased monotonically with increasing strain. The slope of the energy got steeper with increasing magnetic field.We obtained energy plots for all simulated states, which were 130 (13 strain states, 2 field directions, and 5 field values). In the following, we selected all 13 strain states for the lowest (100 mT) and highest (300 mT) magnetic field values to display the magnetic domain structures (Figure 0-7). From these states, we selected the states with 100 mT in parallel configuration, fully compressed (0% strain, Figure 0-6) and fully expanded (6% strain, Figure 0-7), respectively and with 100 mT in the perpendicular (Figure 0-8) and the parallel (Figure 0-9) configuration at 4.5% strain to highlight the impact of field direction on magnetic energy distributions.

Figure 0-5(a, b) are the equilibrium magnetic domain structures obtained for parallel sample configuration. Figure 0-5a and Figure 0-5b show the magnetic structure evolution for a single twin boundary system starting from 6% to 0% at 100 mT and 300 mT respectively. In both cases, one twin domain had a single magnetic domain structure (represented in red, magnetic moments pointing to the left) while the other twin domain across the twin boundary had multiple magnetic 180° domains (yellow, magnetic moments pointing up, and green, magnetic moments pointing down). The magnetic domain boundaries within the right twin were 180° domain boundaries. The twin boundary carried 90° magnetic domain boundaries, where the yellow/red boundary was a head-to-tail boundary and the green/red domain boundary was a tail-to-tail boundary. Figure 0-5c and Figure 0-5d are the equilibrium magnetic structures obtained for the perpendicular sample configuration. Figure 0-5d shows the magnetic domain structure evolution for a single twin boundary system from 0% to 6% strain at 300 mT. It is similar to Figure 0-5(a, b) where one variant had a single domain structure and the other variant across the twin boundary had multiple magnetic domains. In this case, however, the left twin domain with the axis of easy magnetization horizontal had multiple magnetic domains. These results agree with the experimental characterization of magnetization

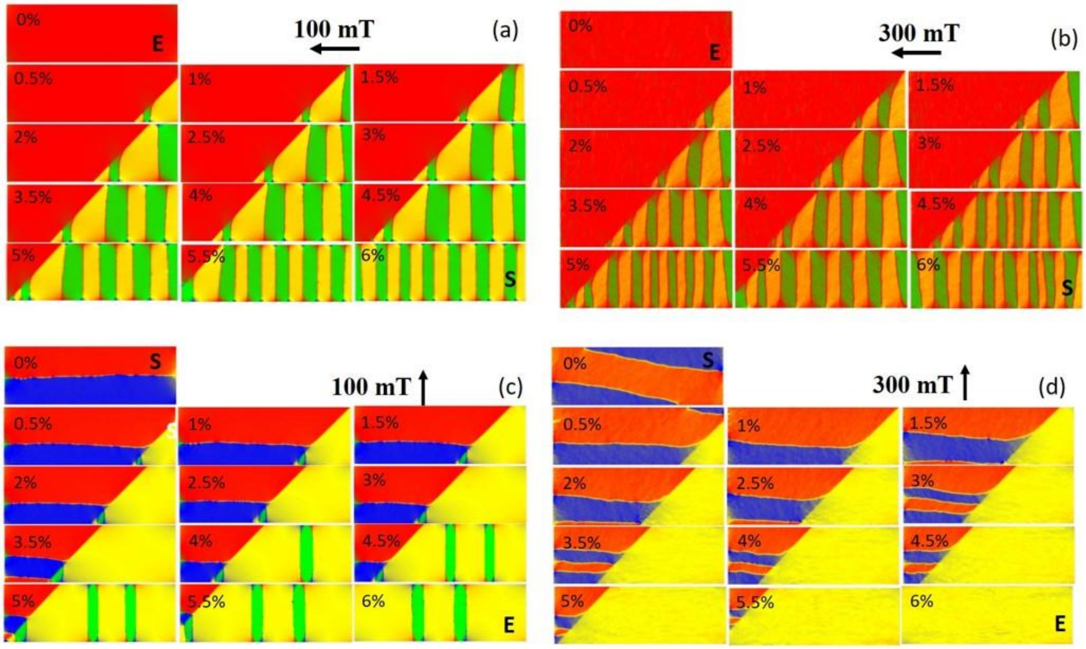

Figure 0-5 Evolution of the magnetic domain structure obtained from simulations for a switching field test at 100 and 300 mT in a single twin boundary state. (a, b) are the equilibrium domain structures for parallel sample configuration and (c, d) are the equilibrium domain structures for perpendicular sample configuration. The letter 'S' and 'E' indicate the start and end of deformation as the switching field test is performed i.e. the sample deforms from 6 to 0% for parallel and 0 to 6% for perpendicular sample configuration. The colors here indicate the direction of magnetization in the magnetic domains: red (←), blue (→), yellow (↑), and green (↓). The red hue in the yellow magnetic domains in (b) is due to a significant rotation of magnetic moments towards the left and away from the direction of easy magnetization as a result of higher magnitude of magnetic field (300 mT).

reported by Faran *et al*. [75]. Whereas at 100 mT (Figure 0-5c), as the magnetic structure evolution occurred from 0% to 6% strain both twin domains contained multiple magnetic domains. Up to a strain of 3.5%, the left twin domain contained one blue magnetic domain (magnetic moments pointing to the right) and the right twin domain had one green magnetic domain. The blue and green magnetic domains met at the twin boundary in a head-to-tail configuration. From 4 to 6% strain, additional green magnetic domains formed in the right twin domain. These green magnetic domains extended across the entire sample.

The four energy terms (anisotropy, exchange, stray field, and Zeeman) that are associated with the total magnetic energy calculation are shown for selected cases in Figure 0-6, Figure 0-7, Figure 0-8, and Figure 0-9. Figure 0-6 and Figure 0-7 demonstrate the energies corresponding to 0% and 6% strain respectively at 100 mT for parallel sample configuration. Since there were no magnetic domain boundaries for the 0% strain

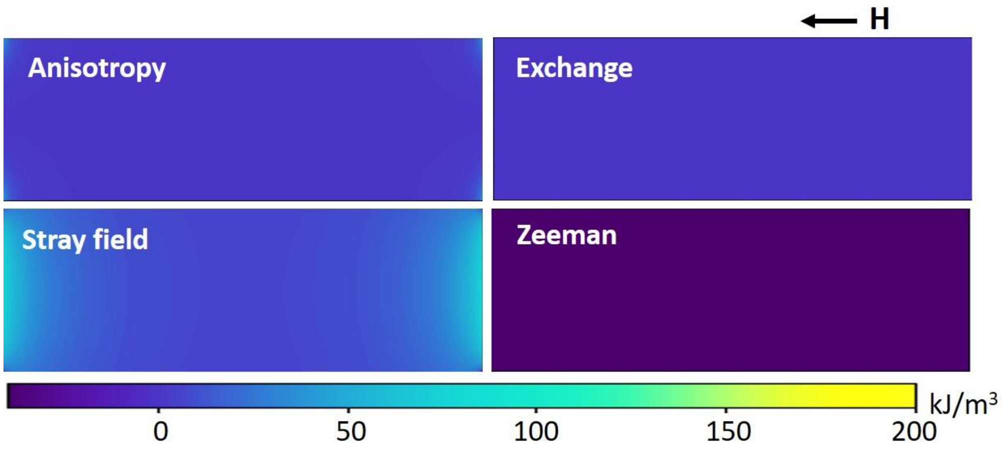

Figure 0-6 Energy maps at 0% strain in a 100 mT magnetic field for sample setup in parallel configuration. The direction of the field is indicated by the arrow. Each plot as labeled represents the anisotropy, exchange, stray field, and Zeeman energy associated with the magnetic domain structure at equilibrium. The maps are homogeneous because the samples has n twin and magnetic domain boundaries.

case (see Figure 0-5a), all the energies were uniformly distributed across the sample (Figure 0-6). In the case of the 6% strain, since there were multiple magnetic domains

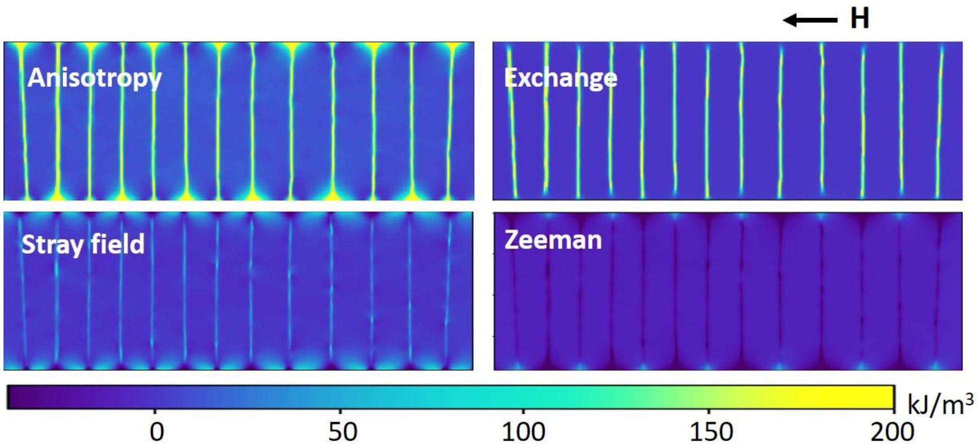

Figure 0-7 Energy maps at 6% strain in a 100 mT magnetic field for sample setup in parallel configuration. High densities of anisotropy and exchange energy decorate the magnetic domain boundaries.

(see Figure 0-5a), the anisotropy and exchange energy was high at the magnetic domain boundaries compared to the regions within the domains (Figure 0-7). Figure 0-8 and Figure 0-9 show the energies associated with the 4.5 % strain at 100 mT for the perpendicular and the parallel configuration respectively.

In Figure 0-8, at the twin boundary and the magnetic domain boundaries (where the domain orientation changes due to transition) the anisotropy and exchange energies are high compared to the regions that have a uniform orientation of magnetic moments. The stray field energy was quite uniform across the sample, but the alternating domain regions (light blue in Figure 0-8 bottom right, green in Figure 0-5), which had the magnetic moments pointing in the direction opposite to the external field, had significantly heightened Zeeman energy and lowered stray field energy.

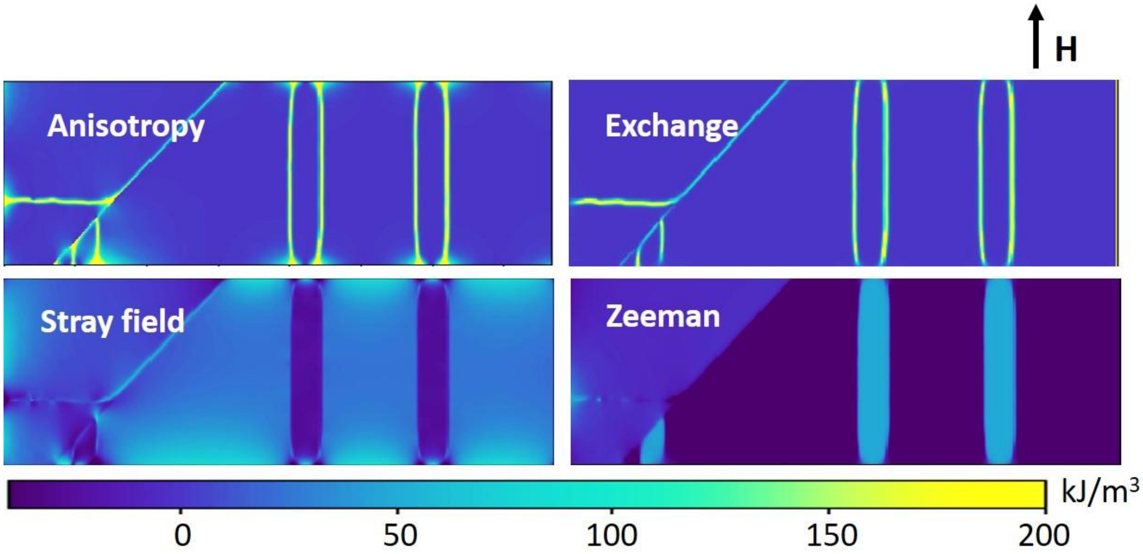

Figure 0-8 Energy maps at 4.5% strain in a 100 mT magnetic field for sample setup in perpendicular configuration. The twin boundary has lower energy than the magnetic domain boundaries. The vertical magnetic domains with magnetization pointing down (green in Fig. 5) have low stray field and high Zeeman energy.

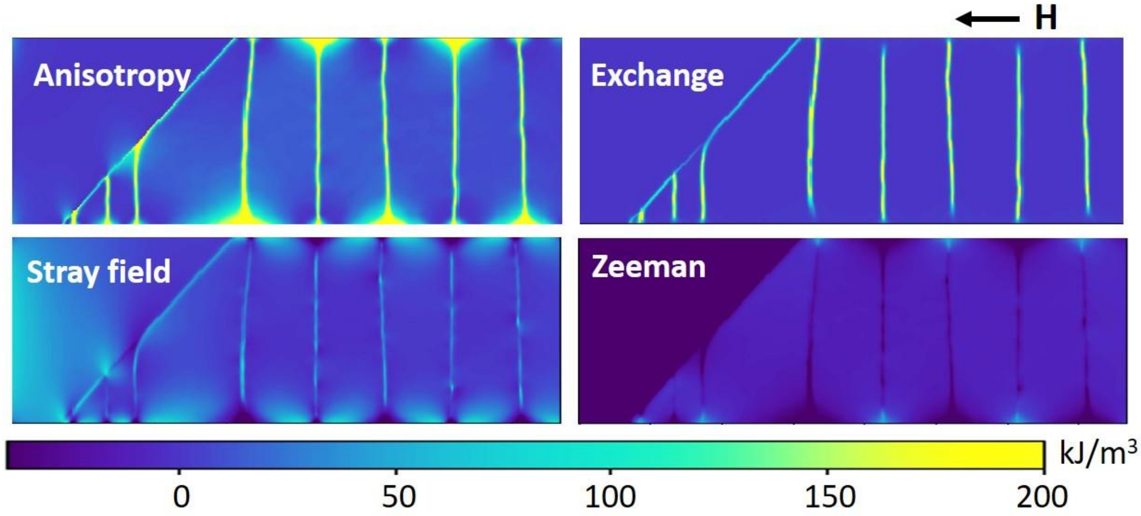

Figure 0-9 Energy maps at 4.5 % strain in a 100 mT magnetic field for sample setup in parallel configuration. The twin domain with c parallel to the longest edge (red in Fig. 5) has low Zeeman energy.

Figure 0-9 represents the same strain state (4.5%, 100 mT) in parallel configuration. While the anisotropy, exchange and stray field energies were high at transition regions compared to the regions with uniform orientation of magnetic moments, the Zeeman energy, on the whole, fell on the lower end of the energy scale with no distinguished change in energy from one magnetic domain to another.

Figure 0-10a and Figure 0-10b show the contribution from each energy term (anisotropy, exchange, stray field and Zeeman energy) towards the total magnetic energy for different strain states at 100 mT in the parallel and the perpendicular configurations. From comparing the energies in Figure 0-10 with the magnetic domain evolution in Figure 0-5, it follows that the anisotropy and exchange energies increased with the increasing number of magnetic domains in the structure, whereas the stray field and Zeeman energies decreased. For the perpendicular field configuration (Figure 0-10b), at 4% strain and at 4.5% strain the Zeeman energy increased, while the stray field energy decreased.

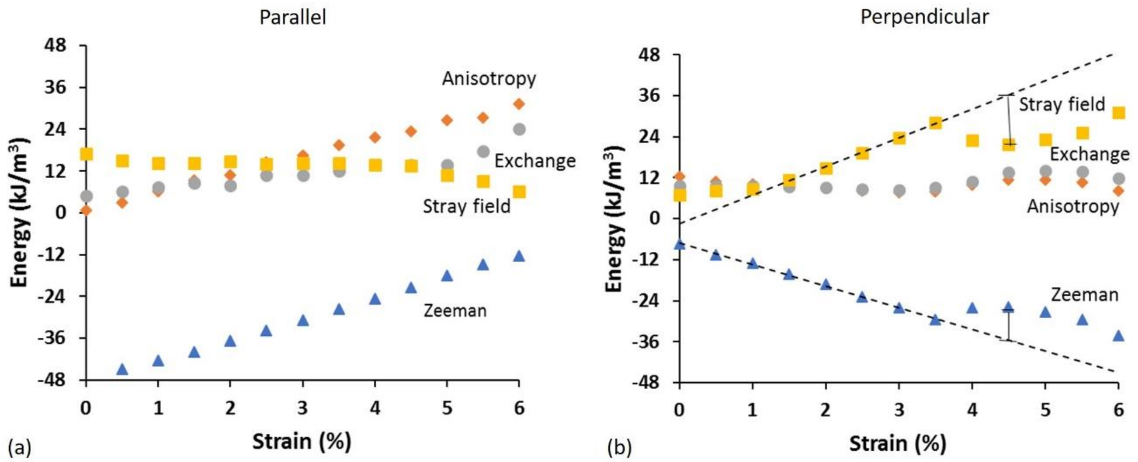

Figure 0-10 Contributions from anisotropy, exchange, stray field and Zeeman energies to the total magnetic energy of equilibrium magnetic structures obtained at different strain states at 100 mT. (a) In the parallel configuration and (b) In the perpendicular configuration.

5.5 Discussion

Here we qualitatively compare the experimental and numerical results. We do not attempt to compare the experimental and numerical results quantitatively because the volume of the simulated sample is orders of magnitude smaller than that of the experimental sample. Experimental data (Figure 0-2) shows that for the parallel sample configuration, switching in the material is abrupt, whereas for the perpendicular sample configuration it occurs gradually in a step-like behaviour. The results from numerical calculations for the parallel sample configuration show that the magnetic energy density monotonously decreases with increasing magnetic field and strain (Figure 0-3). This decrease in energy density explains the spontaneous switching that we see in the experimental data. Once the magnetic field provides enough driving force to nucleate a twin boundary, the twin boundary moves through the entire sample since, the energy continuously decreases as the twin boundary advances. In the case of the perpendicular sample configuration (Figure 4), results from numerical calculations at 100 mT show a localized increase in energy from 4 % to 5.5 % strain. With an increasing magnetic field, the overall energy becomes lower and so does the local energy maximum at large strain. Above 200 mT magnetic field, the total energy follows the same monotonously decreasing trend as for the parallel configuration. This means that when a twin boundary forms at a low magnetic field strength, it can advance only as long as the energy decreases and it stops at a strain where the energy is a local minimum. To overcome the energy barrier (i.e. the local maximum) the magnetic field must increase. Since the material remains at the energy valley until the required magnetic field is applied, the twin boundary movement is retarded. This results in gradual, step-like switching.

The shape of the sample plays an important role for the twin boundary motion. The motion of the twin boundary magnetizes the sample and, thus, reduces the Zeeman energy. This is the main driving force for twin domain switching. As the sample gets magnetized, the stray field energy increases. For a parallelepiped bar (present study), in the perpendicular configuration, the magnetic field is perpendicular to the long axis of the sample, which results in a higher demagnetization factor (and, thus, higher stray field energy) compared to the parallel configuration (where the field is parallel to the long axis of the sample). This effect is shown in Figure 0-10 where the stray field energy increases strongly with an increasing strain between 1 and 3.5 % strain for the perpendicular configuration (Figure 0-10b). In contrast, the stray field energy increases only moderately with ongoing deformation in the parallel configuration (Figure 0-10a).

To lower the stray field energy, the magnetic structure tends to form multiple domains separated by 180° domain walls. This happens for the perpendicular and the parallel sample configurations (Figure 0-5). However, in the parallel configuration, 180° magnetic domains form only in that twin domain where the axis of easy magnetization is perpendicular to the magnetic field. In this case, the 180° magnetic domains reduce the stray field energy without changing the Zeeman energy. In contrast, because of the large demagnetization factor perpendicular to the longest edge of the sample, 180° magnetic domains form in both twin domains for the perpendicular configuration. This means that in the twin domain with the easy axis of magnetization parallel to the magnetic field, the green domains (in Figure 0-5c) are magnetized opposite to the direction of the magnetic field. These domains increase the Zeeman energy. The increase in Zeeman energy partially compensates for the decrease in stray field energy. This can be explained by comparing the domain structures in Figure 5a (100 mT, parallel configuration) and Figure 5c (100 mT, perpendicular configuration). In Figure 5a, as the material is magnetized parallel to the length of the sample, the demagnetization factor is less than the perpendicular field case shown in Figure 5c. Due to this large demagnetization for case 5c, the stray field energy is lowered at the expense of Zeeman energy (Figure 10). This lowering of stray field energy results in domain splitting for case 5c, while case 5a contains a single red domain.

These results have implications for the design of magnetic shape memory alloy actuators. If one attempts to build an on-off actuator, i.e. a device that switches abruptly between two states, the magnetic field must be applied parallel to the long direction of the magnetic shape memory element. In this configuration, the device switches instantaneously from fully elongated to fully contracted. To switch abruptly from fully contracted to fully extended requires a strong magnetic pulse perpendicular to the sample, where the field strength of the pulse is sufficient to saturate the sample. If one attempts to build a positioning actuator capable of adjusting a position gradually, the magnetic shape memory element must be long and the magnetic field must be applied perpendicular to the stroke. Gradual resetting with a magnetic field parallel to the direction of the stroke is not possible, since such actuation results in instantaneous and complete switching. Instead, resetting can be achieved with second actuator in a “push-push” configuration [76].

5.6 Conclusions:

We combined experiments and numerical calculations to study the effect of magnetic field to sample orientation on twin boundary motion with varying magnetic fields on a rectangular bar sample. Lowering the Zeeman energy is the main driving force for twin domain switching. As the twin boundary moves through the sample, the sample gets magnetized, which increases the stray field energy. This effect is stronger when the magnetic field is perpendicular to the longest sample extension because of a higher demagnetization factor. The demagnetizing field hinders twin domain switching in the perpendicular configuration. The formation of 180° magnetic domains partially offsets this shape effect. The perpendicular configuration lends itself for a gradual positioning device while the parallel configuration is ideal for an on-off switch.

5.7 Acknowledgements

We thank Andrew Armstrong for assisting with the experimental set-up. PM acknowledges partial financial support from the National Science Foundation through project DMR-1710640 and the high-performance R2 compute cluster (DOI: 10.18122/B2S41H) provided by Boise State University’s Research Computing Department.

CHAPTER SIX: MAGNETIC DOMAIN-TWIN BOUNDARY INTERACTIONS IN NI-MN-GA

Medha Veligatla[1]

Carlos J. García-Cervera[2,3]

Peter Müllner[1]

[1] Micron School of Materials Science and Engineering, Boise State University, Boise, 83725, USA.

[2] Deparment of Mathematics, University of California, Santa Barbara, 93106, USA

[3] Visiting Professor at BCAM – Basque Center for Applied Mathematics, Mazarredo 14, E48009 Bilabo, Basque Country, Spain

Keywords: Twin boundary, magnetic domain boundary, micromagnetics, magnetic energies

Submitted to Acta Materialia on September 11, 2019 and is under review

6.1 Abstract

The stress required for the propagation of twin boundaries in a sample with fine twins increases monotonically with ongoing deformation. In contrast, for samples with a single twin boundary, the stress exhibits a plateau over the entire twinning deformation range. We evaluate the twin boundary and the magnetic domain boundary interactions for increasing twin densities. As the twinned regions get finer, these interaction regions result in additional magnetic domains that form magnetoelastic defects with high magnetostress concentrations. These magnetoelastic defects act as obstacles for twinning disconnections and, thus, harden the material. Whereas in a low twin density microstructure, these high-energy concentrations are absent or dilute and their effectiveness is reduced by the synergistic action of many twinning disconnections. Therefore, with increasing twin density, the interaction of the twin boundary and the magnetic domain boundaries reduces the twin boundary mobility. The defect strength has a distribution such that twinning disconnections overcome soft obstacles first and harder obstacles with ongoing deformation. The width of the distribution of obstacle strength and the density of obstacles increase with increasing twin density and, thus, the hardening coefficient increases with increasing twin density.

6.2 Introduction

Ni-Mn-Ga belongs to a class of ferromagnetic shape memory alloys that undergoes shape change by martensite variant reorientation induced by a magnetic field [8,77]. In the absence of a magnetic field, a mechanical stress aids in the martensitic reorientation [78]. The deformation mechanism in MSM alloys is twinning. The regions on either side of the twin boundary have different magnetization and crystallographic orientations. When the material is undergoing deformation, the twin boundary propagates across the sample. While this happens, crystallographic reorientation takes place and one region starts to grow at the expense of the other. This crystallographic reorientation can take place with a single twin boundary or with many twin boundaries. The amount of deformation in the MSM alloy is quantified by conducting a uniaxial compression test. Many research groups characterize the mechanical properties of these MSM alloys with and without a magnetic field [5,7,79,80]. There are also research groups that study the magnetic domains [13,34,60,73,81–83] and twin boundary structure, type, and mobility [24, 84-87].

Before the research in magnetic shape memory alloys steered towards the study of twin boundaries in Ni-Mn-Ga, L. Straka *et al.* [54,88] studied the mechanical behavior of these alloys by varying the number of twin boundaries in the sample. The experimental results showed that the sample with many twin boundaries required high stress compared to the sample with a single twin boundary to move the twin boundaries through the

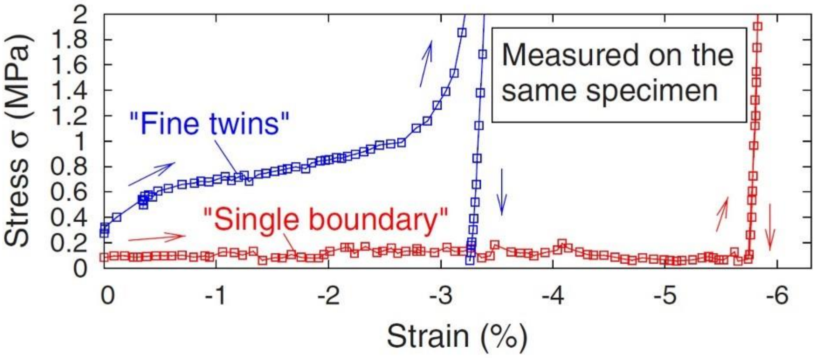

Figure 0-1 Stress-strain curves for a sample with a single twin boundary (red) and with fine twins (blue). The sample with only one twin boundary exhibits a stress plateau at about 0.1 MPa. The sample with fine twins exhibits clear work hardening over a stress range from 0.4 to 2 MPa. Reprinted from [L. Straka, N. Lanska, K. Ullakko, and A. Sozinov, Twin microstructure dependent mechanical response in Ni – Mn – Ga single crystals, Appl. Phys. Lett. 96, 2010], with the permission of AIP Publishing [54].

sample. In addition, the stress monotonically increased with increasing strain for the sample with many twin boundaries, i.e. the samples exhibit work hardening (Figure 0-1, [54]). In contrast, there is a stress plateau for the sample with a single twin boundary. Later, as the research advanced in the MSM field, it was recognized that the twin boundaries in Ni-Mn-Ga can be classified into Type I and Type II. In 2016, Heczko *et al.* [89] studied the mechanical behavior of Ni-Mn-Ga alloys with single type I, single type II, and fine twins. Again, the stress-strain curves for the single twin boundary exhibited plateau, while for the fine twin boundaries the stress increased monotonically. Researchers speculated that the interaction of twin boundaries with magnetic defects or mutual interactions of differently oriented twins caused this work hardening [89]. The work hardening affects functional properties of magnetic shape memory alloys such as the magnetic switching field and hysteresis losses. Understanding these properties will aid the design of MSM actuators and sensors.

In the present study, we evaluate these twin boundary and magnetic domain interactions for increasing twin density in a Ni-Mn-Ga sample by using micromagnetics simulations. We use a code developed by Garcia-Cervera [74]. Hobza *et al.* used this code to study magnetic torque phenomena in Ni-Mn-Ga [70]. Here, we add magnetic energy mapping to this code to identify the structure and energy of defects resulting due to the interaction of magnetic domains and twin boundaries. The results show that the interaction of magnetic domain boundaries and twin boundaries cause the hardening of fine twinned Ni-Mn-Ga.

6.2.1. Micromagnetics:

In the present study, we simulate the domain evolution using micromagnetics. We obtain the equilibrium magnetic state with respect to time with a fixed twin microstructure, i.e. with static twin boundaries. Studying the static twin boundary state allows us to investigate greater details at the interaction sites of magnetic domains and twin boundaries. Garcia-Cervera [74] developed this micromagnetics code and Hobza *et al*. [70] applied it to Ni-Mn-Ga system to study the torque generated by a magnetic field on samples with various twin microstructures. This code evaluates the Landau-Lifshitz equation. In our method, we only solve linear systems of equations with constant coefficients. The cost per step of our method is O(N log N), where N is the number of cells. Using this customized micromagnetics code, we obtained magnetic energies for magnetic equilibrium structures at varying twin densities in Ni-Mn-Ga. The equilibrium magnetic structures and energies obtained through these simulations take into account the anisotropy, exchange, stray field, and Zeeman energies. The code solves the following Landau-Lifshitz-Gilbert equation to approach the minimum energy state:

$$d\mathbf{M}(\mathbf{r})/_{dt} = -\mu_0\gamma\,\mathbf{M}\times\mathbf{H} - \alpha\left({}^{\mu_0\gamma}/_{M_s}\right)\mathbf{M}\times[\mathbf{M}\times\mathbf{H}] \qquad \text{(equ. (10) in 4.1.2)}$$

where $\mathbf{M}(\mathbf{r})$ is the magnetization density at position $\mathbf{r}$, γ is the gyromagnetic ratio, α is the dimensionless damping parameter, and $\mathbf{H}(\mathbf{r})$ is the magnetic field, which is the negative derivative of total energy with respect to magnetization:

$$\mathbf{H} = -\frac{\delta E}{\mu_0\delta\mathbf{M}} = -\left({}^{2K_u}/_{\mu_0 M_s^2}\right)(M_2+M_3) + \left({}^{2C_{ex}}/_{\mu_0 M_s^2}\right)\Delta\mathbf{M} - \nabla\mathbf{U} + \mathbf{H}_{\text{ext}}$$

(eq. (10) in 4.1.2)

where K_u is the anisotropy constant, M_s is the saturation magnetization, M_2 and M_3 are magnetization components that are orthogonal to the axis of easy magnetization, C_{ex}

is the exchange constant, μ_o is the magnetic permeability of free space and $\mathbf{H}_{ext}$ is the external magnetic field.[2] The individual summation terms in Equation 2 are the energies associated with the magnetocrystalline anisotropy, the exchange interaction, the stray field and the external magnetic field. In the present study, we evaluate the evolution of magnetic domain structures to study the twin boundary motion in the absence of an external magnetic field. Therefore, the Zeeman energy term is neglected in this calculation (i.e. $\mathbf{H}_{ext} = 0$). The other energy terms are briefed as follows: magnetocrystalline energy is the energy associated with the orientation of magnetic domains with respect to the axis of easy magnetization, the exchange energy is the short range interaction energy between neighboring magnetic moments, and the stray field is associated with magnetic domain splitting. A detailed description of these energy terms and the micromagnetics code is given in [70].

6.3 Numerical Simulation

We studied the effect of twin boundary density on hardening by increasing the twin density and evaluating the distribution of the magnetic moments and their resulting magnetic energies. We conducted micromagnetics simulations to obtain the magnetic energies and the equilibrium magnetic structures to evaluate the magnetic domain and twin boundary interactions. The twin densities were varied from a minimum of 1.7 μm^{-1} to a maximum of 47 μm^{-1} on samples with 1 to 5% strain (with 1% increments). The sample sizes used to conduct this study varied from 1.56 µm x 0.53 µm x 0.36 µm (1% strain) to 1.63 µm x 0.50 µm x 0.36 µm (5% strain). Therefore, as the sample dimension changes with the strain, the minimum and maximum twin density at each strain percent is

---

[2] Equations 1 and 2 are given in SI units and differ from those given in Ref. [74].

slightly different. The number of twin boundaries in a sample were systematically increased from the lowest twin density with 1 twin boundary, to the highest twin density with 65 twin boundaries. While doing so, the position of the twin boundaries on the sample edge were determined by the strain on the sample i.e. the fraction of the region with the *c*-axis (axis of easy magnetization) parallel and perpendicular to the sample length was determined by the strain on the sample. Throughout the sample length, the twin boundaries were inclined at 45° with the sample edge and across these twin boundaries the *c*-axis was defined to be nearly 90°. The schematic representation of the simulation set up for the single twin boundary system and a dense twin boundary system is shown in Figure 0-2.

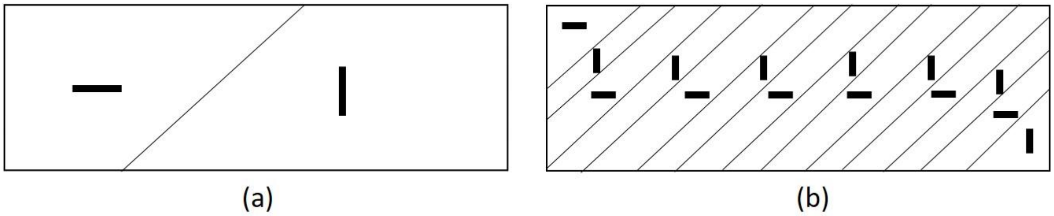

Figure 0-2 Schematic of the sample with (a) single twin boundary and (b) dense twin structure. The horizontal and vertical lines represent the orientation of the c-axis (axis of easy magnetization) and the twin boundaries are inclined at 45° to the edge of the sample.

The horizontal and vertical lines within the twinned regions represent its preferred direction of magnetization, which is nearly 90° across the twin boundaries. The volume of the simulation sample was divided into 384 cells along the longest dimension and 192 cells along the intermediate dimension, making it 73,728 cells in total. Therefore, the dimension of each cell is ≈ 4.06 nm x 2.7 nm (at 1% strain) and each of these cells has an assigned magnetization vector. Each simulation ran for 20,000 iterations. Therefore, to obtain a magnetic structure with the minimum energy configuration, we added multiple runs that continue from the previously ended run, making a total of 180,000 iterations. The individual magnetic energy contributions (anisotropy, exchange, and stray field energy) for the equilibrium state were also obtained during these simulations. All the magnetic energies and domain structures for the equilibrium states obtained for this study were generated in the absence of an external magnetic field.

6.4 Results

Figure 0-3 shows the magnetic energy density plots for twin densities ranging from 1.7 to 47 μm^{-1} for samples with 1 to 5% strain. For low twin densities (up to about 5 μm^{-1}), the calculated energies did not differ significantly.

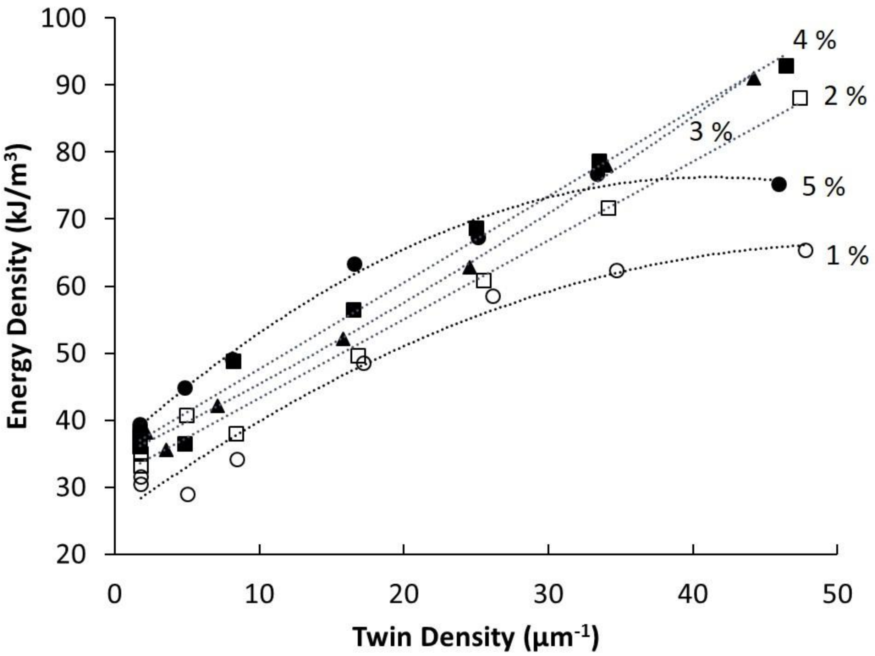

Figure 0-3 Plot of total magnetic energy densities as a function of increasing twin density for samples with 1 – 5 % strain with varied twin densities from 1.7 to 47 μm^{-1}.

Therefore, the energy values appeared scattered with no particular trend. At higher twin densities (from about 8.4 to 47 μm^{-1}), for samples with 2, 3, and 4% strain, the energy density increased linearly with increasing twin density and with increasing strain. In contrast, for samples with 1 and 5% strain, the energy density regressed at a higher twin density. This non-linear dependence was due to the magnetic resolution dependence on the cell size. With a 384 x 192 cell size, at 1 and 5%, the finest twinned regions (i.e. the region between two twin boundaries) were about 12.5 nm wide, which was equivalent to a magnetic domain wall size [11]. At this scale, there were only 3 cells in the twinned region (cell size at 1% strain = 4.06 nm x 2.7 nm) i.e. the actual rotation of magnetic moments within one cell was large, such that the averaging of magnetic moments within one cell led to large errors. The averaging of magnetic moments in one cell resulted in incorrect magnetic domain patterns when the twin width correlated with the magnetic domain wall thickness. This was the case for 1 and 5% strain at large twin density.

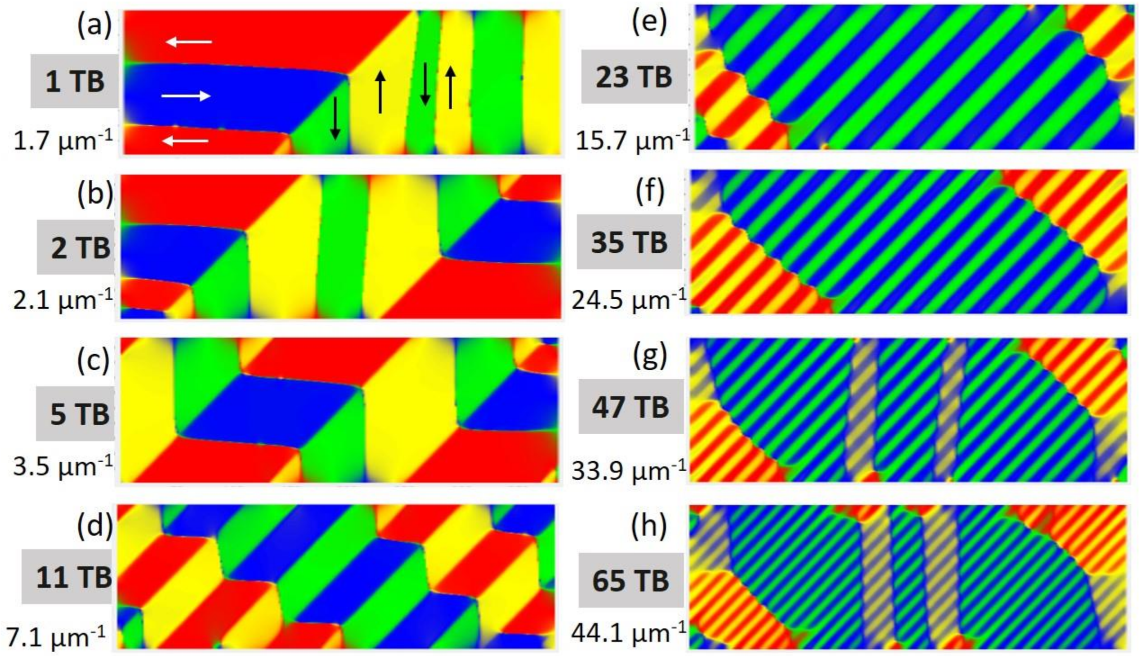

Figure 0-4 The evolution of equilibrium magnetic domain structures of Ni-Mn-Ga at 3% strain with increasing twin density from 1.7 to 44.1 μm^{-1}. The colors red (←), blue (→), yellow (↑), and green (↓) in the figures represent the direction of magnetic moments.

Figure 0-4 shows the equilibrium magnetic domain structures for twin densities ranging from 1.7 (Figure 0-4a) to 44.1 µm^{-1} (Figure 0-4h) for a sample with 3% strain. Colors red (←), blue (→), yellow (↑) and green (↓) represent the direction of magnetic moments. At lower twin densities, from Figure 0-4a to Figure 0-4d (i.e. 1.7 to 7.1 µm^{-1}) the magnetic structures formed 90° domains across the twin boundary and 180° domains within the twinned regions, resulting in a staircase like magnetic domain pattern across the twin boundaries. These results agree with the experimental characterization of magnetization with magneto-optics reported by O. Söderberg *et al* [60]. At higher twin densities, as the twinned regions became thinner, i.e. going from 15.7 to 24.5 µm^{-1} twin density (Figure 0-4e and Figure 0-4f), these staircase like transition regions moved towards the sample edges and became less prominent. The center of the sample had twinned regions with single magnetic domains separated by 90° domain walls across the twin boundary. As the twinned regions got even finer (33.9 and 44.1 µm^{-1}) additional vertical magnetic domains appeared that were perpendicular to the sample length (Figure 0-4g and Figure 0-4h).

Figure 0-5 shows the contribution of each magnetic energy term (anisotropy, exchange, and stray field energy) towards the total magnetic energy for these equilibrium structures (at 3% strain). With increasing twin density (from 1.7 to 44.1 µm^{-1}) the anisotropy and exchange energy increased monotonically, while the stray field energy remained about constant, and the anisotropy energy contributed the most to the total magnetic energy.

Figure 0-6 shows the equilibrium magnetic domain structure for a single twin boundary system. The colors in the figure represent the orientation of the magnetic

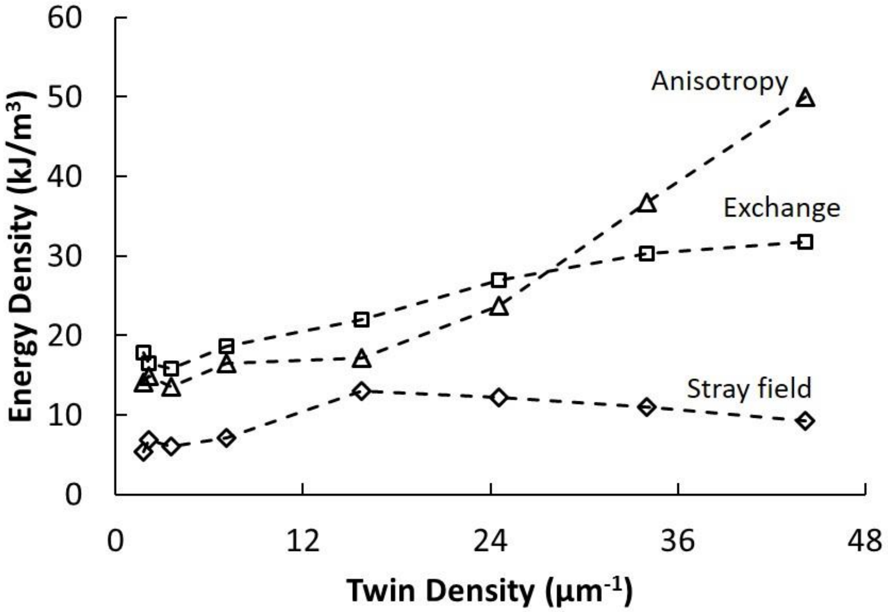

Figure 0-5 Plot of anisotropy, exchange and stray field energy densities with increasing twin density for Ni-Mn-Ga at 3% strain.

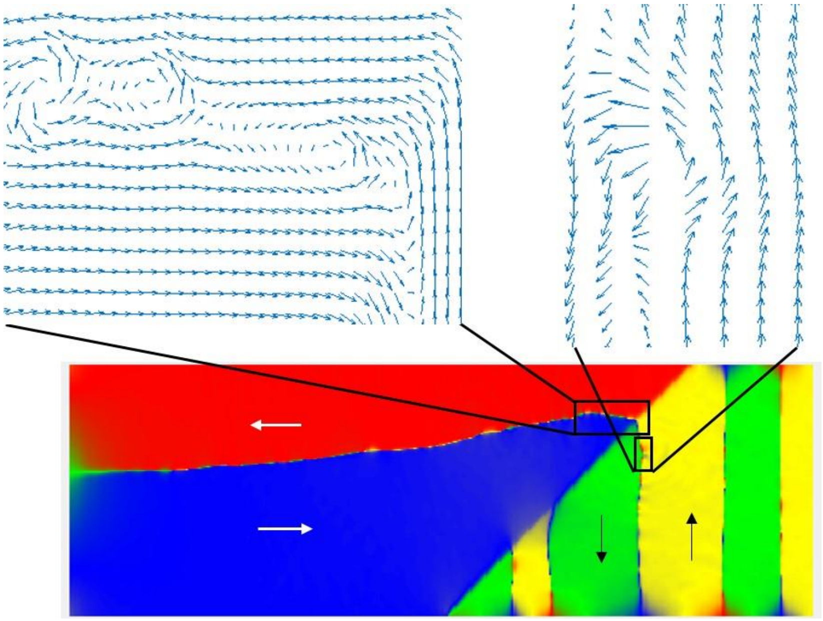

Figure 0-6 Equilibrium magnetic domain structure for a single twin boundary in the sample. The orientation of magnetic moments at the twin boundary and domain boundary are magnified in the regions indicated by rectangles. Colors red (←), blue (→), yellow (↑) and green (↓) represent the direction of magnetic moments. The arrows in the magnified sections reveal vortices of the local magnetic moments.

moments indicated by the arrows. In the twin domain with *c* horizontal, a 180° magnetic domain boundary extended from the twin boundary to the surface of the sample. This magnetic domain boundary connected with another 180° magnetic domain boundary in the twin domain with *c* vertical. Additional vertical 180° magnetic domain boundaries extended from surface to surface. These results agree with the experimental Kerr microscopic images reported by Perevertov *et al.* [55] and Heczko *et al.* [27]. Closure domains formed where the 180° magnetic domain boundaries reached the surface. A region on a magnetic domain boundary and the region at the intersection of the magnetic domain and the twin boundary are magnified in the top two figures. The arrows in these magnified regions show the orientation of the magnetic moments. The regions on either side of the twin boundary formed 180° magnetic domains. These 180° domain walls contain multiple magnetic vortices. The magnetic energy distribution (i.e. the contribution from the anisotropy, the exchange and the stray field energies to the equilibrium state) of a selected region at the intersections of the twin boundary and magnetic domain boundaries is represented in Figure 0-7. The anisotropy and exchange energies were heightened at the twin boundary and at the domain boundary. At the twin boundary, the energies were about 100 kJ/m^3, at the magnetic domain boundary about 200 kJ/m^3, and within the magnetic domains, the energies were less than 25 kJ/m^3. Whereas, the stray field energy was less than 25 kJ/m^3 throughout the sample. As the twinned regions got finer, additional magnetic domains formed that were perpendicular to the sample length. In such an equilibrium magnetic domain structure, there were regions where the twin boundaries interacted strongly with the vertical magnetic domain boundaries and there were regions where the twin boundaries did not or only weakly interacted with the vertical magnetic domains.

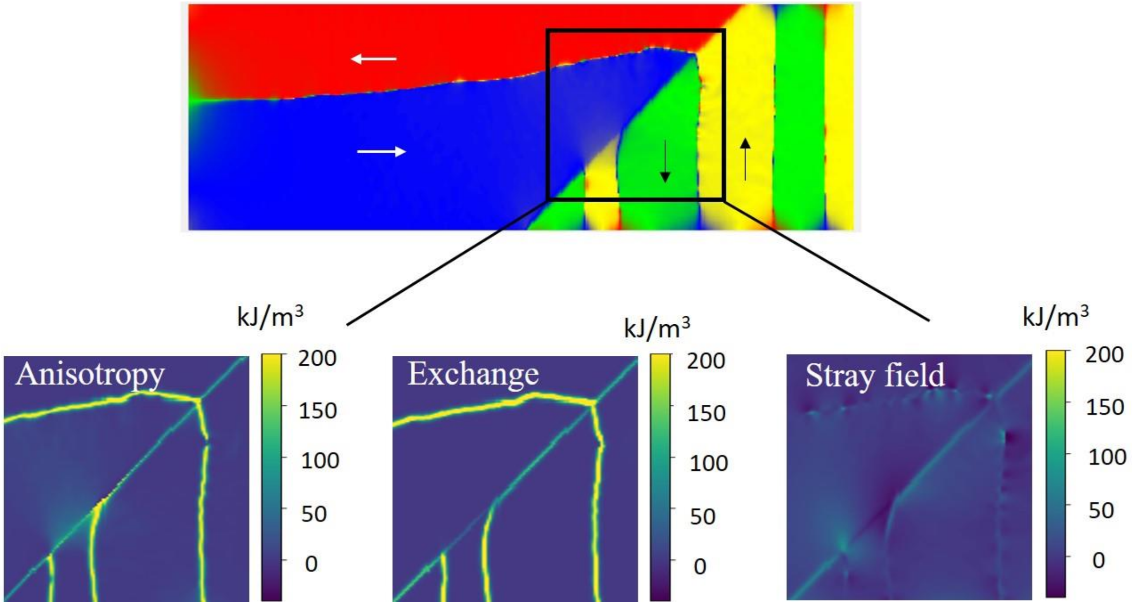

Figure 0-7 Magnetic energy distribution for a single twin boundary in the sample. The Anisotropy, Exchange, and Stray field energy are plotted for the selected region from the domain structure.

Figure 0-8 is the equilibrium magnetic domain structure for such a dense twin boundary system. A region from a regular twin boundary distribution and from the vertical magnetic domain feature is magnified in the inset to show the local orientation of the magnetic moments. In the regular twin boundary region the magnetic moments within the twinned regions were oriented parallel to the axis of easy magnetization i.e. the magnetic moments arrangement was such that they form 90° domain walls across the twin boundaries (blue (→) followed by green (↓) across the twin boundaries). This pattern continued across the entire length of the sample except where the twins interact with the vertical magnetic domain boundary. The red circle highlights a region where the twin boundaries and the vertical magnetic domain boundaries interact. Here, the 90°

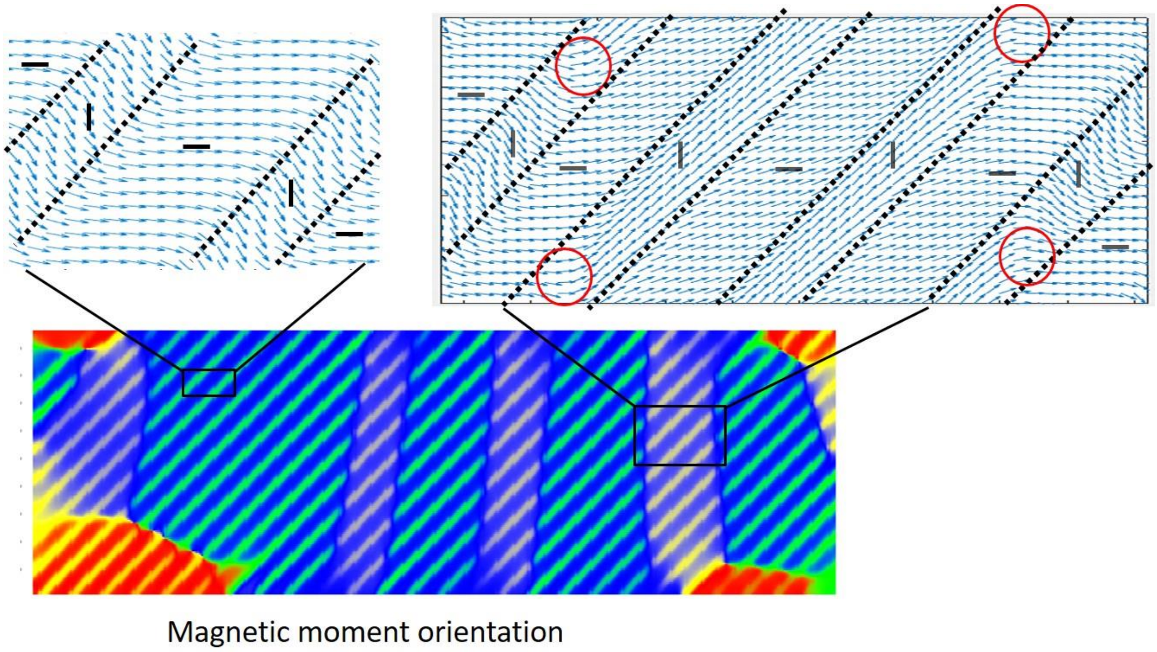

Figure 0-8 Equilibrium magnetic domain structure for a dense twin structure in the sample. The orientation of magnetic moments for regular twin boundary region (left square inset) and vertical domain regions (right square inset) are magnified. Colors red (←), blue (→), yellow (↑) and green (↓) represent the direction of magnetic moments. The black dotted lines are a guide along the twin boundary. The region of intersection of vertical magnetic domain and the twin boundaries are highlighted in a red circles where the magnetic moments are aligned perpendicular to the c-axis (↕). The alternating horizontal and vertical lines within each twin boundary represent the orientation of the c-axis (axis of easy magnetization).

domain walls no longer existed. In this region, irrespective of the twin boundaries, all the magnetic moments aligned horizontally. Within the twins, the magnetic domains tended to orient at a certain angle pointing upwards (approximately parallel to the twin boundaries as emphasized with the titled red rectangle).

Figure 0-9 shows the individual magnetic energy distribution for the regular twin boundary region and the vertical domain feature. The anisotropy energy in the regular twin boundary region was significantly lower compared to that in the vertical magnetic domain feature. Right at the intersection of the twin boundary and the vertical domain wall there were high concentrations of anisotropy energy and also the alternating regions within the vertical domain feature had high anisotropy energy.

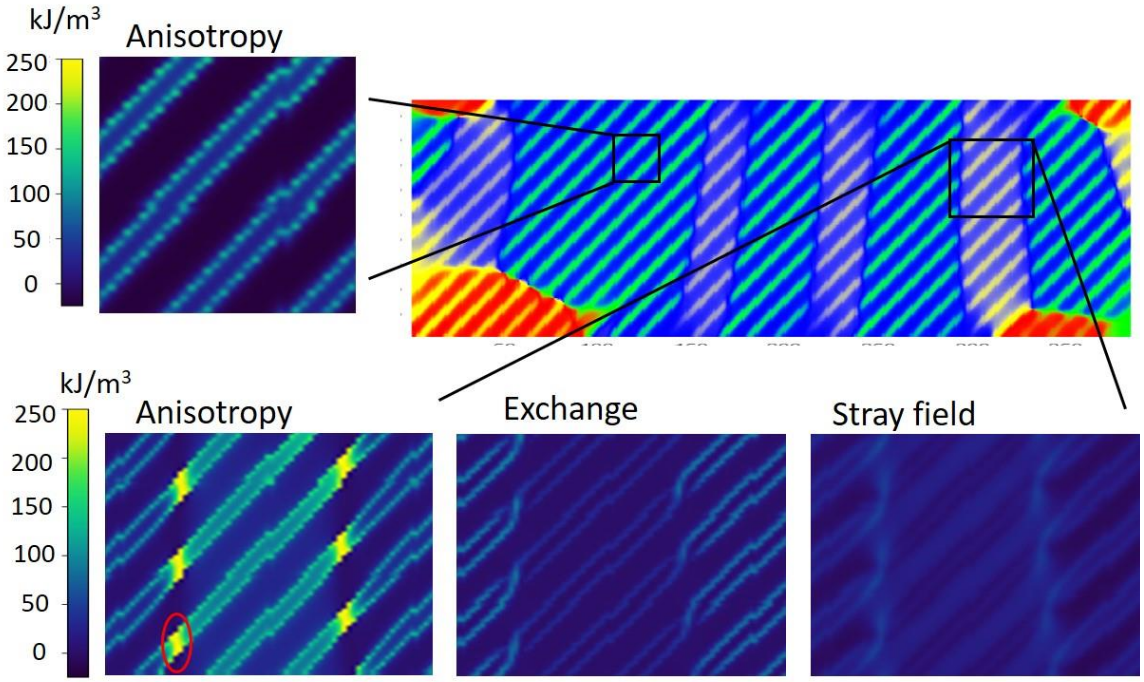

Figure 0-9 Individual magnetic energies for a dense twin structure in regular twin boundary region (left square inset) and vertical domain regions (right square inset). The high concentration of anisotropy energy at the intersection of the twin boundary and vertical domain boundary is highlighted in the oval pattern.

The total magnetic energy (sum of anisotropy, exchange, and stray field energy) for a single twin boundary system is compared to a dense twin boundary system in Figure 0-10. The distribution of magnetic energy was uniform (and low) throughout the sample except at transition regions for the single twin boundary system and at magnetic domain boundaries. Whereas in a dense twin boundary system with multiple vertical magnetic domains there were localized energy concentrations (≈ 300-400 kJ/m^3) at the intersection of the vertical magnetic domain and twin boundaries. In these regions, the magnetic moments stood at a right angle with the direction of easy magnetization.

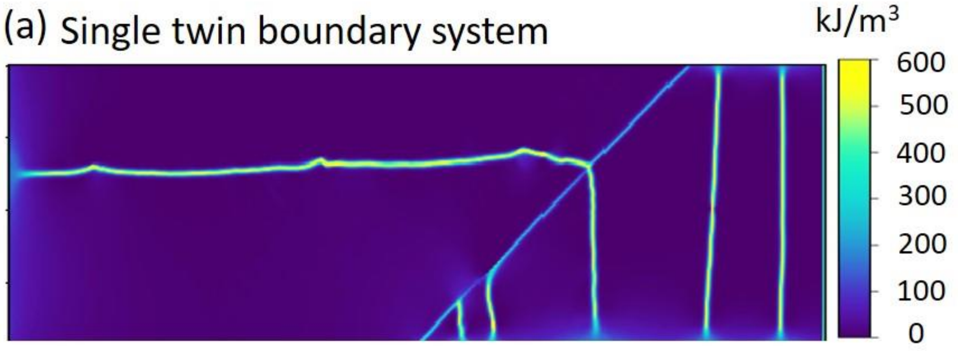

(a) Single twin boundary system

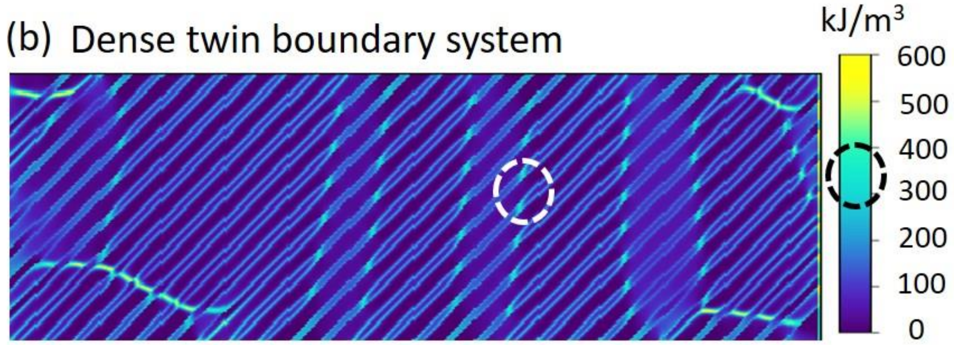

(b) Dense twin boundary system

Figure 0-10 Total magnetic energy for (a) single twin boundary and (b) dense twin structure in Ni-Mn-Ga. The interaction regions of twin boundary and vertical magnetic domains are highlighted in the energy distribution plot. The magnetic energy at this region is also highlighted on the scale.

6.5 Discussion

To study the twin boundary mobility in Ni-Mn-Ga with a fine twinned structure, we evaluated the mesoscale magnetic defects and the magnetic energies associated with these defects. Here we discuss how these magnetic defects lead to the work hardening in densely twinned Ni-Mn-Ga.

In shape memory alloys, deformation twinning (i.e. the motion of twin boundaries) is the dominant deformation mechanism [90]. The twinning disconnection [91] (or twinning dislocation) is the elemental carrier of localized displacements [92]. As a twinning disconnection moves along the twin boundary, the twin boundary is displaced by the disconnection step height and one twin domain gets displaced with respect to the other twin domain by the Burgers vector.

Three basic mechanisms contribute to the twinning stress in shape memory alloys: (i) the Peierls stress [93], (ii) the nucleation stress for generating twinning disconnections [24], and (iii) the interaction of disconnections with other defects such as other twin boundaries [9] and other twinning disconnections [94]. The threshold stress for the twin boundary mobility depends on the twin dislocations and their interaction with interfaces. When the twinning disconnections come closer to an interface, they have to overcome their mutual repulsive interaction. As they overcome this energy barrier with higher mechanical stress, the twinning disconnections move further and get stuck at the domain interface in a position of local mechanical equilibrium. In the present study, the energy barriers in a fine twin system are the high concentrations of anisotropy energy (Figure 0-9 and are also visible in the total magnetic energy plot in Figure 0-10b).

High magnetic energy concentrations arise where twin boundaries interact with the vertical magnetic domains (Figure 0-8). These sites form the transition zones (highlighted in the circle pattern, Figure 0-8) where the magnetic moments are perpendicular to the *c*-axis (axis of easy magnetization) giving rise to high localized internal magnetostress [23,26]. These regions – we call them magnetoelastic defects – are the same regions that have high concentrations of anisotropy energy (highlighted in the oval pattern, Figure 0-9). In these defect regions, the magnetoelastic coupling results in distortion of the lattice, i.e. where the magnetic moment is perpendicular to the *c*-axis (axis of easy magnetization). This distortion is similar to the distortion of Guinier-Preston zones in precipitation strengthened aluminium alloys. Similarly, these magnetoelastic defects result in hardening of a fine twinned MSM alloy. The magnetostress is highest when the magnetic field is perpendicular to *c* and in such a case, the magnetic field exceeds the saturation field and the maximum shear stress exerted by the magnetic field is $\frac{K}{s}$ (is about 1.37 MPa, where $K = 1.65 \text{ x } 10^5 \text{ J/m}^3$ is the anisotropy constant for the 5M structure [59] and $s = 0.1274$ is the twinning shear [87]). The concentration of such magnetoelastic defects increases with increasing twin density. As the twin regions become finer, the contribution from the anisotropy energy drastically increases (Figure 0-5) thereby increasing the total magnetic energy (Figure 0-3). As the twinning disconnections move along the twinning plane, they approach these high energy magnetoelastic defects, which they experience as obstacles. The twinning dislocations require higher mechanical stress to move past these magnetoelastic defects.

In regions where the twin boundaries do not interact with the vertical magnetic domain, there are no such energy concentrations (Figure 0-10). This is because, across the twin boundaries, the magnetic moments are oriented parallel to their axis of easy magnetization (magnified region in Figure 0-8: blue (↔) followed by green (↕)). This results in zero internal magnetostress. So, the twinning dislocations move along the twin boundary without experiencing any obstacles.

In their statistical model, N. I. Glavatska *et al.* [22] assume a distribution of stress sources in magnetic shape memory alloys. The normal Gaussian distribution of the magnetostress effect was used to obtain results for qualitative consideration, which leads to this equation:

$$\langle(|\sigma_n| - |\sigma_c|)^2\rangle = \sigma_0^2 \qquad (3)$$

$(|\sigma_n| - |\sigma_c|)$ is the critical stress that is needed to overcome the pinning of the twin boundaries. Where, $|\sigma_n|$ is the stress of the *n*th twin boundary, $|\sigma_c|$ is the average stress value from the stress distribution curve, and σ_0 is a parameter describing the width of the distribution.

Here, we identify magnetic vortices and the transition regions at the vertical magnetic domain boundaries in densely twinned structures as stress sources. In these regions, the magnetic moments are strongly inclined away from the direction of easy magnetization. Thus, the local magnetic field has a substantial component perpendicular to *c* and causes a magnetostress [26]. In 2004, Chernenko *et.al.* [23] modified the statistical model that was proposed by Glavatska *et al.* to theoretically study the magnetoelastic behaviour of Ni-Mn-Ga with single and poly variant microstructures. They use σ_0 = 1.1 MPa, i.e. the twinning stress ranges to a maximum of 2.2 MPa. From their stress-strain loops (obtained at magnetic fields higher than saturation), the stress (mechanical stress + magnetostress) at 1.5% for a poly variant Ni-Mn-Ga is 3.25 MPa [23].

With increasing twin density, the density of magnetoelastic defects increases and so does the density of local magnetic stress concentrations (Figure 0-8 and Figure 0-10b). Further, the strength of these magnetoelastic defects is more widely distributed. In addition, with higher twin density, more twinning disconnections contribute to the total deformation. The following deformation path emerges: At the onset of deformation, only those disconnections move, that are far away from a magnetoelastic defect. The motion of these disconnections requires low stress. Eventually, these disconnections encounter a strong magnetoelastic defect and stop moving. Other disconnections start to move at a slightly higher stress. As deformation goes on, more and more disconnections encounter stronger magnetoelastic defects and require higher and higher stress for deformation to proceed. This is the work hardening mechanism in highly twinned Ni-Mn-Ga. As the twin density increases, the obstacle density and the width of their strength distribution increase and, thus, the work hardening coefficient (i.e. the slope of the stress-strain curve) increases. Glavatska *et al.* and Chernenko *et al.* found a stress variation of 1-3 MPa [22,23] as discussed above. These stress distributions lead to a corresponding hardening range and agrees well with the mechanical properties reported by Straka *et al.* (Figure 0-1, [54]).

At low twin density, magnetic domain boundaries have high energy and form magnetoelastic defects at twin boundaries (Figure 0-6 and Figure 0-7). However, these defects are very widely spaced, such that many twinning disconnections travel between them. These twinning disconnections form dislocation pile-ups. The force on the head dislocation of a pile-up is the regular force exerted by the applied shear stress multiplied by the number of dislocations in the pile-up ([95], also e.g. [96]). Therefore, the twinning disconnections overcome these defects at very low applied stress. This explains the stress plateau for deformation of samples with only one twin boundary (Figure 0-1).

For highly twinned microstructures, only one or a few twinning disconnections travel between two magnetoelastic obstacles. The number of disconnections per obstacle decreases with increasing twin density because the density of defects increases. Thus, the thinner the twins are, the fewer the disconnections that assist the active dislocation overcoming an obstacle. This further adds to the hardening rate.

6.6 Conclusions

We evaluated the magnetic domains and twin boundary interactions in Ni-Mn-Ga. We found that as the twinned regions get finer, the magnetic interactions with twin boundaries form magnetoelastic defects with the magnetization perpendicular to the axis of easy magnetization. This configuration results in high stress concentrations. The magnetoelastic defects play an important role for twin boundary mobility. The moving twinning disconnections require higher mechanical stress to overcome these local stress concentrations. Thus, magnetoelastic defects act as obstacles for twin boundary motion. In contrast to the dense twin structure, the synergistic action of many twinning disconnections reduces the effectiveness of magnetoelastic defects in microstructures with low twin density. Therefore, in a single twin boundary system or a less dense twin structure, the twin boundaries propagate across the sample with a constant stress. The higher the twin density, the more effectively magnetoelastic defects hinder twin boundary motion. Together with the statistical distribution of defects, these mechanisms result in work hardening. Therefore, the work hardening rate increases with increasing twin density.

6.7 Acknowledgements

We would like to acknowledge high-performance computing support of the R2 compute cluster (DOI: 10.18122/B2S41H) provided by Boise State University’s Research Computing Department. This research was supported in part by the National Science Foundation under project number DMR-1710640.

CHAPTER SEVEN: ENERGY CONVERSION IN NI-MN-GA WITH ASYMMETRICAL BIAS MAGNETIC FIELD

Medha Veligatla[1]

Paul Lindquist[1]

Carlos J. Garcia-Cervera[2,3]

Peter Müllner[1]

[1] Micron School of Materials Science and Engineering, Boise State University, 83725, USA.

[2] Deparment of Mathematics, University of California, Santa Barbara, 93106, USA

[3] Visiting Professor at BCAM – Basque Center for Applied Mathematics, Mazarredo 14, E48009 Bilabo, Basque Country, Spain

Keywords: Magneto-electrical energy conversion, micromagnetics, inclined magnetic field

To be submitted to Journal of Magnetism and Magnetic Materials

7.1 Abstract

Mechanical energy converts to electrical output in a magnetic shape memory alloy due to a variation of internal magnetic flux which is associated with twin boundary motion or crystal reorientation. We studied the mechano-electric energy conversion with dynamic experiments under a bias magnetic field. Tilting the bias magnetic field away from the transverse direction towards more parallel to the twin boundary increases power generation efficiency. Numerical simulations show that at both low and at high magnetic fields, magneto-crystalline anisotropy energy and the Zeeman energy dominate the formation of magnetic domains, respectively. The resulting magnetic domain pattern is asymmetric with respect to the transverse direction at lower fields and symmetric at higher fields. At lower fields, the formation of 180° magnetic domains result in reduced net magnetization parallel to the load axis when the bias field is tilted against the twin boundary. However, when the bias field is tilted along the twin boundary, the major portion of the domain structure (at low strains and in a compressed state) saturates parallel to the load axis. Therefore, the magnetic structure generated at lower bias fields tilted parallel to the twin boundary is more favorable to maximize the power generation due to increased net magnetization parallel to the load axis. However, from experiments, we find that the minimum bias field required to expand the sample against the axial load must be higher than the switching field. Therefore, in order to optimize power output, the energy conversion has to take place at lower bias magnetic fields with the field direction inclined close to parallel to the twin boundaries, and on samples with low twinning stress.

7.2 Introduction

Magnetic shape memory (MSM) alloys are classified as a group of functional materials that exhibit large recoverable strains. Depending on the martensite structure these materials exhibit magnetic field induced strains up to 12% strain [5,6,60]. The strain in these materials is due to the crystallographic reorientation that occurs via twinning [10]. Due to the magneto-crystalline anisotropy, the magnetization in the sample changes with the movement of the twin boundary [26,59], and thus does magnetic flux. The reverse phenomenon, i.e. the deformation-induced change of magnetization, is called the inverse magneto-plastic (IMP) effect [97]. If the sample is placed inside a conductive coil, and the sample is subjected to mechanical cyclic loading and unloading, the cyclic magnetic flux change induces an AC voltage [48,50]. The power harvesting capabilities of MSM alloys under a bias magnetic field applied perpendicular to the loading direction were reported by various research groups [47,49–51,98,99]. The voltage output generation depends on various experimental factors such as the sample size, the number of turns in the conductive coil, the stroke length, the frequency of cycling, the biased magnetic field and also the direction of the biased field.

Nelson *et al.* [100] conducted initial experiments and also developed a model to characterize the power harvesting capability of MSM alloy by tilting the sample in a transverse magnetic field. Recently Guiel et. *al.* [101] showed that the voltage output can be maximized when the bias field was applied 10-20° (or 100-110° in the present study, set up shown in Appendix D) to the loading direction. For a sample size of 20 x 3 x 3 mm^3, the maximum voltage output obtained was 1280 mV (peak-to-peak voltage) at 9.34° away from the transverse direction and along the twin boundary (corresponding to

99.34° in the present study) with transverse (inclined) and axial magnetic fields. This was a 10-fold increase over the output voltage of 122 mV when the bias magnetic field was applied perpendicular to the loading axis. Guiel *et al.* used finite elemental analysis to study the internal magnetic flux density of MSM alloys and concluded that the dramatic increase in voltage output with magnetic field direction change is due to the internal magnetic structure, albeit without detailing the nature of that structure.

In the present study, through experiments, we investigated the voltage/power generation capabilities of an MSM alloy with a sample size of 7.54 x 3.54 x 2.04 mm^3. We also used micromagnetics to study the evolution of domain structures as a function of magnetic field inclination away from perpendicular to the load axis. From the results obtained with experiments and numerical calculations, we evaluate the influence of magneto-crystalline anisotropy and Zeeman energy on the internal magnetization orientation. We show that the asymmetrical behavior of the energy harvesting capability with an inclined magnetic field at lower magnetic fields is due to strong magneto-crystalline anisotropy and the formation of magnetic domains. Whereas, at higher magnetic fields, the Zeeman energy determines the orientation of magnetization and reduces the energy conversion efficiency.

7.3 Experiments and simulations

A single crystal with nominal composition $Ni_{50.5}Mn_{27.75}Ga_{21.75}$ was grown by the Bridgman-Stockbarger technique using the crystal growth system developed by Kellis *et al.*[102]. A sample was cut from the end nearest to the seed that had a 10 M crystal structure and a composition of $Ni_{49.66}Mn_{28.98}Ga_{21.36}$. as determined with energy-dispersive X-ray spectroscopy (EDS). A wire saw was used to cut parallel to {100} faces of the crystal and the sample was polished mechanically with paper and slurry with a final diamond size of 1 µm. The final sample shape was 7.54 x 3.54 x 2.04 mm^3 when fully extended. The transformation temperatures of the sample were measured at a low magnetic field (250 Oe) in a vibrating sample magnetometer (MicroSense Model 10 VSM) while heating and cooling from 25 °C to 70 °C. The transformation temperatures were M_s = 41.4 °C , M_f = 37.8 °C A_s = 45.5 °C and A_f = 47.9 °C.

A screw-driven mechanical test system Zwick-1455 (Zwick, Um) was used to obtain the full stress-strain response (0 to 6% strain) of the sample. The sample was fully elongated before the test was performed. The bottom end of the sample was glued to the apparatus and the sample was mechanically loaded under compression with a constant strain rate = 0.125 mm/min. A magnetic field of 0.6 T was applied perpendicular to the load axis during the compression test. The system was equipped with a 500N load cell (MTS, Schaffhausen) and extensometers that are insensitive to magnetic fields (Heidenhain, Traunreut). The resolutions were better than 0.5N in force and 10 nm in displacement. The magnetic field produced by a permanent magnet system (Magnetic Solutions, Dublin) was better than 1% homogeneous at the position of the sample for field strength and field direction. In the test apparatus, the sample was mounted with the longest edge parallel to the mechanical load direction. The magnetic field application was constant and parallel to the shortest edge of the sample.

The Magneto-Mechanical Test Apparatus (MMTA, shown in appendix D) was used to measure the magneto stress strain measurements, and the electrical work in a rotating magnetic field. The MMTA system consisted of an electromagnet, a voice coil linear motor, a LVDT displacement transducer, a custom made signal conditioning module scaled to output ± 300 μm displacement, a sample compression micrometer with 1 μm sensitivity, a 44 N piezoelectric load cell with ±15% sensitivity i.e. 112410 mV/kN), interchangeable die springs, and a 1601 turn (inner diameter of 6.2 mm by 11 mm long) 43 AWG pickup coil wound with 0.0031 mm^2 insulated copper wire. The electromotive force, Ɛ, induced in the pickup coil was measured with a variable gain, 1 to 50X, op amp that buffered the coil output from the analog to digital converter (ADC) input. For every test, the root mean square voltage and its corresponding power (connecting the coil to a 290 Ω load resistor shunted across the coil leads) was calculated from the electrical output. The details of this test apparatus, its working and processing of raw data are described in [51]. In this setup, magneto stress strain measurements were obtained at magnetic fields ranging from 0.202 to 0.618 T. The magnetic fields were measured from a Hall probe with a corrected accuracy of ±0.50% to 35 kG (at 25° C) that was centered between the electromagnets such that the flat ends (of the Hall probe) are perpendicular to the field direction. In this apparatus, the Ni-Mn-Ga sample was placed such that the long edge was parallel to the load axis. Before testing, the magnetic field on the sample was ramped to about 0.6 T without constraint from the opposite brass platen and the sample was expanded to the maximum length. Then the sample was compressed against a set of compliant springs of the actuation system, where the initial displacement was recorded with an in-line micrometer. The compliance of the actuation system accommodated a portion of the displacement such that the initial strain on the sample was different from the displacement. We therefore corrected the initial sample strain such that the first stress-strain loop started at 0% and the last compression loop ended at 6% strain (which is the twinning strain of 10M Ni-Mn-Ga), while the other loops were placed between 0 and 6% with equal intervals. Cyclic stress-strain curves were generated by loading and unloading the sample with a voice coil motor under a magnetic field biased perpendicular to the load axis. We conducted the following test sequence: (1) we obtained stress-strain curves for initial displacements ranging from 0.05 to 0.35 mm at 0.618 T bias magnetic field; (2) we repeated these experiments at magnetic bias field strengths of 0.202 T, 0.317 T, 0.395 T, 0.502 T and 0.618 T; (3) we repeated these experiments for frequencies ranging from 50 to 125 Hz; (4) we repeated these experiments for peak-to-peak displacements ranging from 40 µm to 100 µm (stroke length); (5) we repeated these experiments for various directions of the magnetic field ranging from 76 to 104° with respect to the loading axis (*i.e.* 90° was perpendicular to the loading axis) and varying the peak-to-peak displacements from 40 µm to 180 µm. While doing the cyclic loading and unloading in the MMTA, the sample was placed inside the pickup coil with the coil axis oriented parallel to the mechanical load axis.

Micromagnetics simulations were conducted to obtain the magnetic energies for each equilibrium state in a rotating magnetic field. Magnetic fields ranging from 0.1 T to 0.6 T were applied to the sample edge (long axis of the sample). The direction of this magnetic field was varied from 75° to 105° with respect to load axis at 3° intervals (i.e. 90° was perpendicular to the load axis). This study was conducted on samples with strain varied from 1 to 5% strain with 1% increments. Their corresponding sample sizes for 1 and 5% strain are 1.56 µm x 0.53 µm x 0.36 µm and 1.63 µm x 0.50 µm x 0.36 µm respectively. A single twin boundary inclined at 45° to the sample edge was introduced by carefully deforming the sample by hand. The position of the twin boundary was determined by the strain on the sample i.e. the fraction, f_i, of the region with the *c*-axis

(axis of easy magnetization) parallel ($f_{\parallel}$) and perpendicular ($f_{\perp} = 1 - f_{\parallel}$) to the sample length was determined by the strain ϵ on the sample: $\epsilon = f_{\perp}\,(1 - c/a)$, where a and c are the lattice parameters. Therefore, the position of the twin boundary changes with the increasing strain on the sample and the *c*-axis across this twin boundary is nearly perpendicular. The volume of the simulation sample was divided into 384 cells along the longest dimension and 192 cells along the intermediate dimension, making it 73,728 cells in total. Therefore, the dimension of each cell is about 4.06 nm x 2.7 nm (at 1% strain) and each of these cells has one assigned magnetization vector. Each simulation ran for 20,000 iterations. This sequence was repeated with the end configuration serving as input for the new simulation to a total of 180,000 iterations to ensure convergence. Magnetic energies, domain structures and the individual magnetic energy contributions (anisotropy, exchange, and stray field energy) for the equilibrium state were also obtained during these simulations. The simulation code solved the Landau-Lifshitz-Gilbert equation, as described in detail in ref. [18].

7.4 Results

The stress-strain curve obtained from the experimental static deformation test under a 0.6 T bias magnetic field is shown as a dotted curve in Figure 0-1. At the beginning of the test, the stress increased rapidly until the material yielded, followed by a plateau-like region with very little work hardening. To compare the static and the dynamic test results, the two experimental data sets were overlaid in Figure 0-1, where the data obtained from the MMTA is shown in colors (on-line).

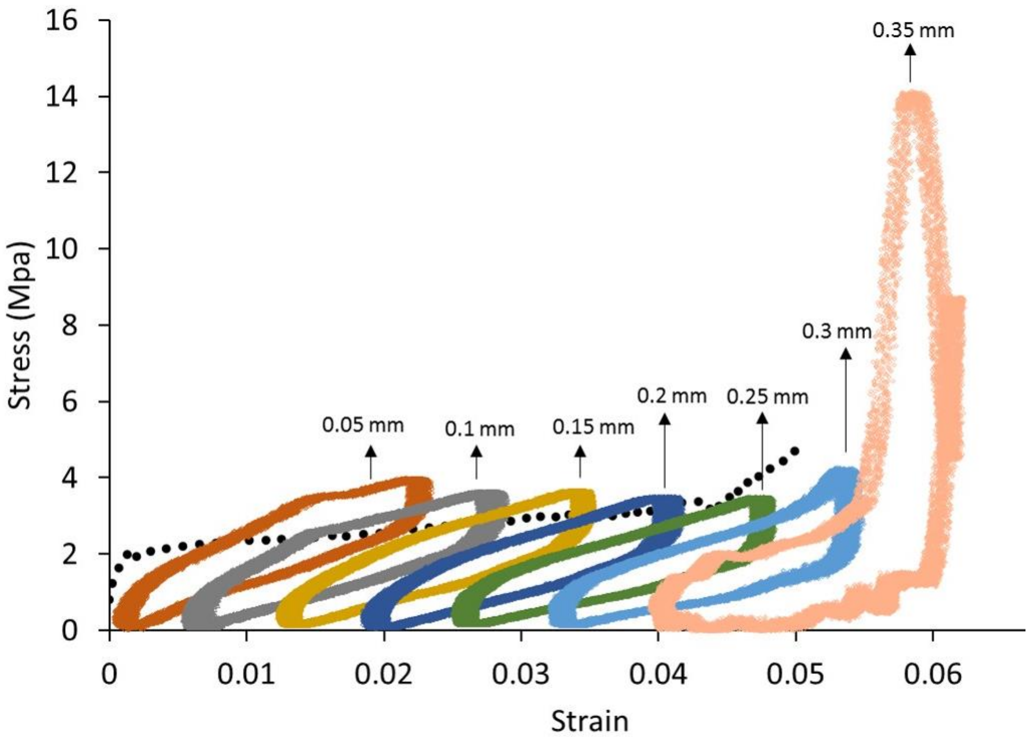

Figure 0-1 Stress-strain curves obtained with static and dynamic loading. The static loading under uniaxial compression obtained at a constant strain rate of 125 mm/min and under a perpendicular bias magnetic field of 0.6 T is represented by the dotted line. The dynamical stress-strain loops (color online) were obtained by cyclic loading and unloading at 75 Hz frequency to a peak-to-peak displacement of 170 µm. Each stress-strain loop obtained at fixed initial displacements ranging from 0.05 to 0.35 mm with 0.05 intervals at 0.6 T bias magnetic field.

The dynamic data stem from the experiments performed with a perpendicular (to the load axis) bias magnetic field of 0.618 T, the loading frequency was 75 Hz, and the peak-to-peak displacement was 170 µm. The dynamic curves have about two fold increase in magnetostress compared to the static deformation curve and the slope of the curves also increased due to the increased strain rate.

The dynamical magneto-mechanical experiments yielded the following results:

1. **Varying magnetic field**: Figure 0-2 shows the voltage (and power) generated as a function of increasing magnetic field. During this test the magnetic

field was increased from 0.202 T to 0.618 T while keeping the frequency and the direction of the magnetic field constant.

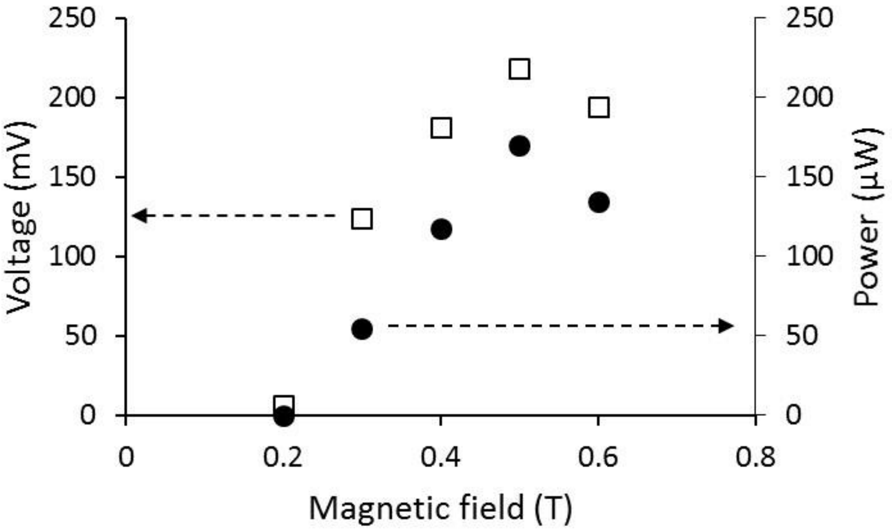

Figure 0-2 Voltage (squares) and power output (circles) measured for increasing magnetic field from 0.202 to 0.618 T, while keeping the following variables constant at: peak-to-peak displacement 80 µm, frequency 75 Hz, bias magnetic field at 77°, and compression on sample 1.8%.

The test sample was strained to 1.85% and then subjected to a cyclic loading and unloading at 75 Hz with a peak-to-peak displacement of 80 µm. The applied magnetic field was at 77° to the loading axis. The results showed that the output voltage (and power) increased with increasing the field, obtaining a maximum of 218.1 ± 0.5 mV (or 170 ± 1 µW) at 0.502 T. The errors are included in the size of the symbols in Figure 7-3. When the field was further increased to 0.618 T, the voltage (or power) values dropped to 194.11 ±0.5 mV (135 ± 1 µW).

2. **Varying frequency**: Figure 0-3 shows the voltage (and power) generated as a function of the loading and unloading frequency. The frequency was increased

from 50 to 125 Hz with 25 Hz increments, while keeping the field constant at 0.618 T and the direction of the field at 77° to the load axis.

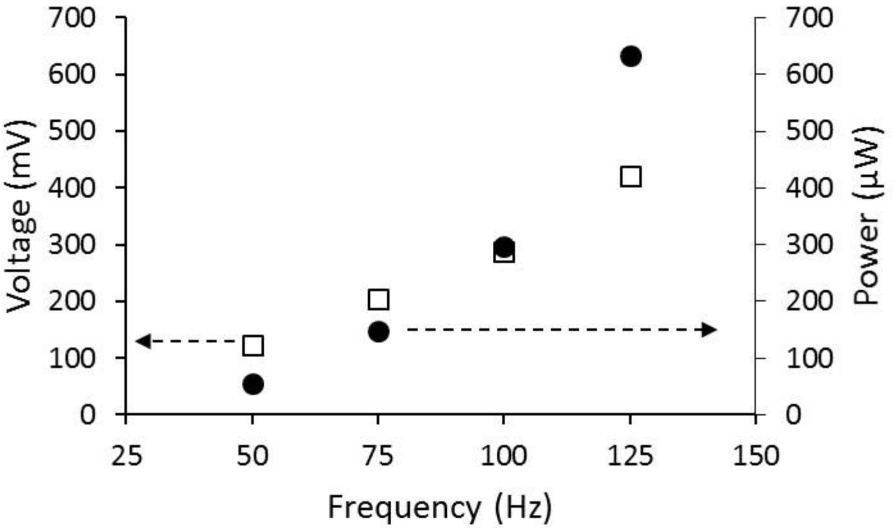

Figure 0-3 Voltage (squares) and power output (circles) measured for increasing frequency from 50 to 125 Hz while keeping the following variables constant at: peak-to-peak displacement 80 µm, frequency 75 Hz, magnetic field 0.618 T, magnetic bias field at 77°, and compression on sample 1.8%.

During this test, the sample was strained to 1.85% and then subjected to a cyclic loading and unloading test with a peak-to-peak displacement of 80 µm. The results showed that the output voltage (or power) monotonically increased with increasing the frequency, achieving a maximum voltage (or power) of 421 ± 0.5 mV (or 634 ± 1 µW) at 125 Hz. Errors are much smaller than the symbols in Figure 7-3. These results also agree with results shown by Lindquist *et al.* [51] that the power output increases with increasing frequency.

3. **Varying the direction of magnetic field**: For this experiment, the output voltage (and power) was recorded for test samples that were strained to 1.8%, 3.1%, and 3.7%. At each of these strains, the magnetic field and the cyclic loading and

unloading frequency was kept constant at 0.618 T and 75 Hz respectively. During these tests, two parameters were varied: 1. magnetic field inclination (with respect to load axis) from 76° to 104° with 2° increments and 2. peak-to-peak displacement from 40 to 180 µm. Figure 0-4 shows the voltage (and power) generated for these test parameters at 1.8% strain.

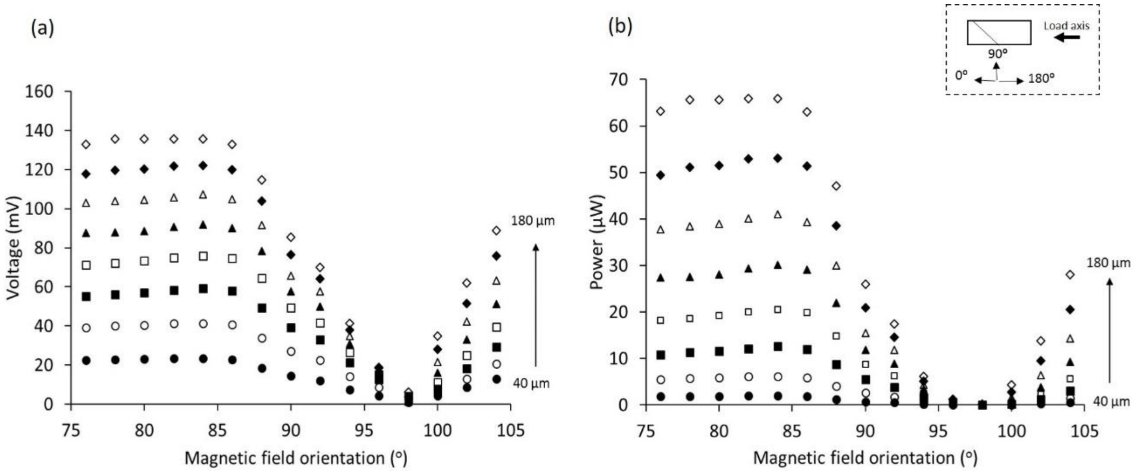

Figure 0-4 (a) Voltage output and (b) Power output measured for magnetic bias field orientations ranging from 76° to 104° with 2° interval and peak-to -peak displacements ranging from 40 to 180 µm with 20 µm intervals. During this experiment, the following variables were kept constant at: magnetic field 0.618 T, frequency 75 Hz, and compression on sample 1.8%. The inset on top right represents the sample, orientation of the twin boundary and the direction of the loading axis.

The output voltage (and power) remained constant (about 130 mV) with increasing field inclination angle from 76° to 84°. From 86° to 98°, the output voltage linearly decreased and converged to nearly 0 mV at 98°. Beyond 98°, the output voltage increased linearly up to 104°. Similar behavior was obtained for the sample with 3.7 % strain (not shown here) except that there was a drop in the voltage at 80° for low peak-to-peak displacement (40 to 60 µm) and at 82° for higher peak-to-peak displacements (80 to 180 µm). For the sample with 3.1%

strain (not shown here), the voltage reduced linearly from 76° and converged to 0 mV at 86° and 88°. From 90° to 100°, the voltage linearly increased with the increasing field inclination angle and beyond 100°, the voltage remained constant.

Micromagnetics simulations were performed for a configuration which replicated the experiments with the goal to calculate the equilibrium magnetic energy (to confirm energy minimization) and the magnetization along the load axis. Except at 0.1 T, at all magnitudes of the magnetic field, the equilibrium energies converged to minimum value. The deviation for 0.1 T was a computational artifact, as the energy did not converge to a minimum within 180,000 iterations. Figure 0-5, shows the normalized change in magnetization with sample elongation (i.e. the difference of axial magnetization at 1 and 2%, at 1 and 3%, at 1 and 4%, and at 1 and 5%, normalized by the saturation magnetization) obtained at 0.2 T (Figure 0-5a) and 0.6 T (Figure 0-5b) as a function of increasing bias magnetic field inclinations (from 75° to 105°). In Figure 0-5a, the change in magnetization in the direction of the load axis (i.e. parallel to the long axis of the sample) with increasing magnetic bias field inclination (from 75° to 105°) at 0.2 T was asymmetric with respect to 90°. Whereas at higher magnitudes of the magnetic field (i.e. at 0.6 T, Figure 0-5b), the data was symmetric about 90°. At both lower (0.2 T) and higher (0.6 T) magnetic fields, the change in magnetization increased with increasing strain difference. The maximum change in magnetization was obtained at 0.2 T, when the bias magnetic field was inclined to 96° with respect to the load axis.

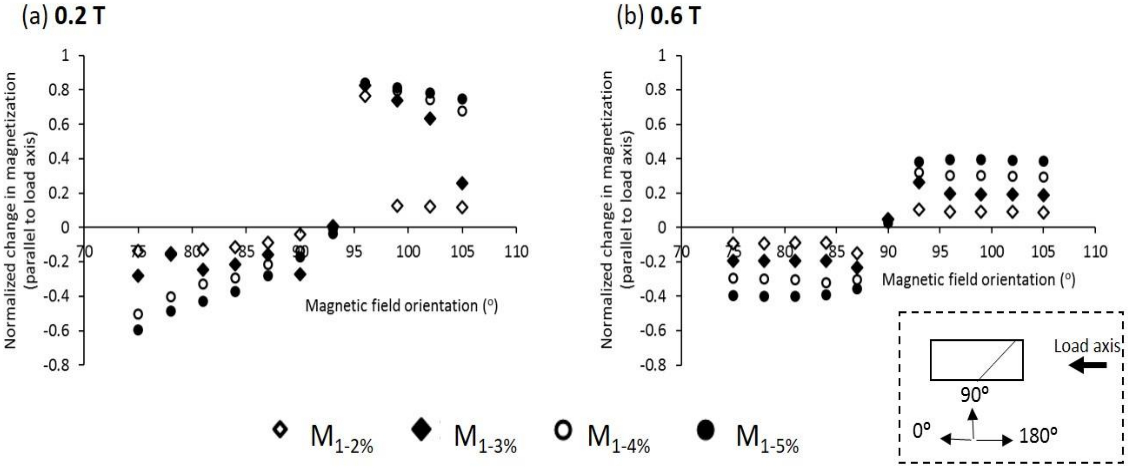

Figure 0-5 Normalized change in magnetization along the load axis at various bias magnetic field inclinations (orientations) from 75° to 105° (with respect to load axis) obtained from numerical calculations. The change in magnetization was obtained for (a) 0.2 T and (b) 0.6 T. The inset is a guide to the field inclination angles and the direction of the load axis.

Figure 0-6 shows the equilibrium magnetic domain structures obtained at low bias magnetic fields (i.e. at 0.2 T) for 1% (Figure 0-6a) and 5% (Figure 0-6b) strain. The arrows in Figure 0-6 indicate the direction of magnetization of its respective domains taken in a central area where the magnetization direction was not impacted by the sample surface. All the structures consisted of a single twin boundary inclined at 45° to the long edge of the sample. In Figure 0-6a (i.e. at 1% strain), at 84° and 90° bias field inclinations, the region on the left side of the twin boundary formed 180° domains (red and blue regions) and the blue region became more prominent as the field inclination was increased. The region on the right remained as a single domain (yellow, ↑). At 96° inclination, the structure evolved into a single magnetic domain per twin region (blue - left domain and yellow - right domain). In Figure 0-6b (i.e. at 5% strain), the magnetic domain structure remained more or less the same with increasing bias field inclination. The structures consisted of 180° domains (blue and red regions) in the left twin region and a single domain (yellow) in the right region. The magnetic domain structures that

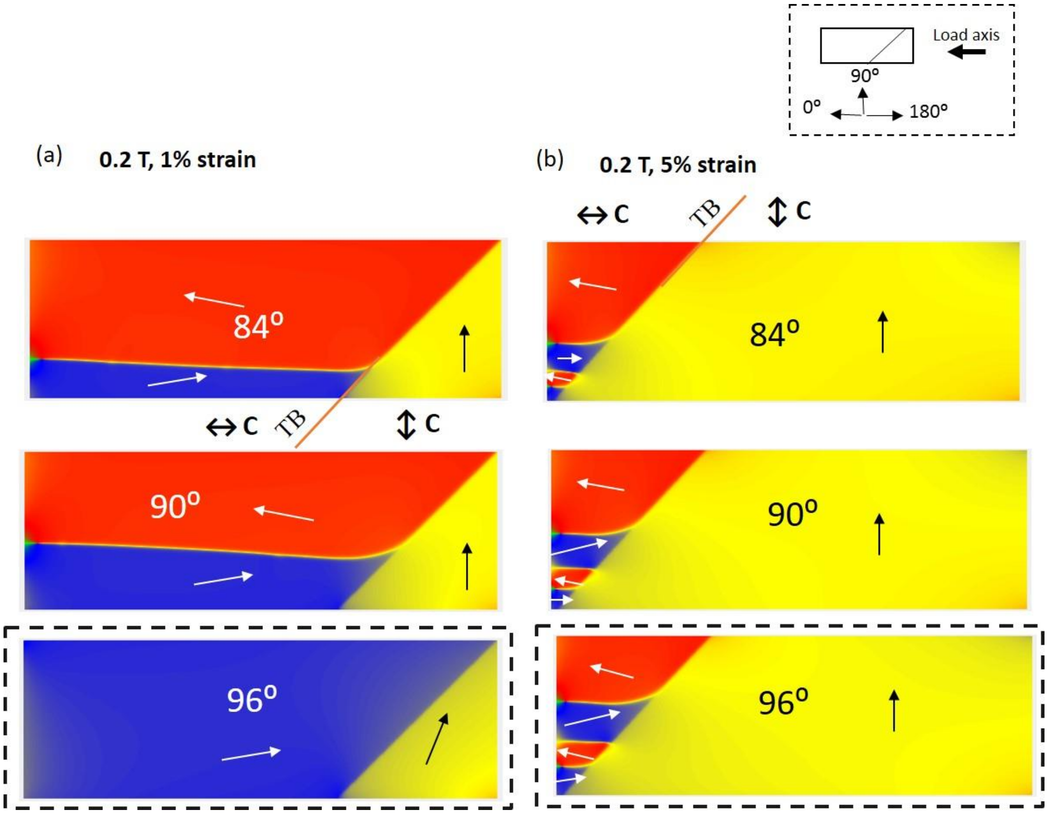

Figure 0-6 Shows the comparison of magnetic domain structures at 1% and 5% strain at the low bias magnetic field. Magnetic domain structures were obtained from simulations at (a) 0.2 T, 1% strain and (b) 0.2 T, 5% strain for magnetic bias field orientations at 84°, 90°, and 96°. The orientation of the bias field (with respect to the load axis) is denoted by the numbers on its corresponding domain structures and the direction of magnetization occupied in the center of each magnetic domain is indicated by the arrows. The domain structures that result in maximum net magnetization along the load axis are highlighted in dashed boxes. “TB” denotes twin boundary and “c” denotes the direction of easy magnetization. The schematic on top right is a representation of the sample and the direction of the load axis. The magnetic domain structures corresponding to all magnetic field orientations ranging from 75° to 105° are shown in Appendix D.

results in maximum net magnetization parallel to the loading direction were obtained at 96° of field orientation and are highlighted in dashed boxes.

Figure 0-7 shows the equilibrium magnetic domain structures at low magnetic field- 0.2 T (Figure 0-7a) and at higher magnetic field- 0.6 T (Figure 0-7b) for 1% strain obtained at various magnetic bias field inclinations. The arrows in Figure 0-7 indicate the direction of magnetization of its respective domains taken in a central area where the magnetization direction was not impacted by the sample surface. All the structures consisted of a single twin boundary inclined at 45° to the long edge of the sample. At 84° and 90° bias field inclinations, the region on the left side of the twin boundary formed 180° domains (red and blue regions) and the blue region became more prominent at higher field orientation. Whereas the region on the right remained as a single domain (yellow, ↑). At 96° inclination,

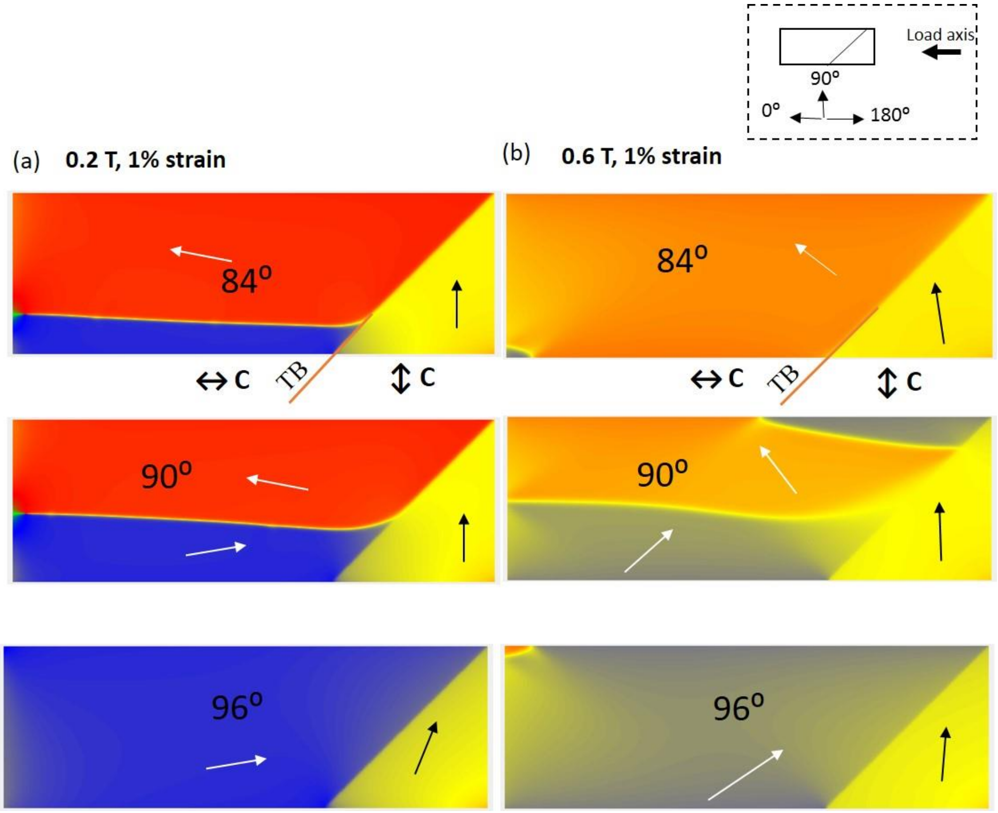

Figure 0-7 Shows the comparison of magnetic domain structures at the low and the high bias magnetic fields. Magnetic domain structures were obtained from simulations at (a) 0.2 T, 1% strain and (b) 0.6 T, 1% strain for magnetic bias field orientations at 84°, 90°, and 96°. The orientation of the bias field (with respect to the load axis) is denoted by the numbers on its corresponding domain structures and the direction of magnetization occupied in the center of each magnetic domain is indicated by the arrows. "TB" denotes twin boundary and "c" denotes the direction of easy magnetization. The schematic on top right is a representation of the sample and the direction of the load axis. The magnetic domain structures corresponding to all magnetic field orientations ranging from 75° to 105° are shown in Appendix D.

the structure evolved back into a single magnetic domain per twin domain (blue - left domain and yellow - right domain). In Figure 0-7a, at low magnetic field (0.2 T), when the magnetic field is aligned at 96° (i.e. the field is aligned more parallel to the twin boundary), the direction of net magnetization in the left twin domain (blue region) is aligned more towards the load axis. Whereas, in Figure 0-7b, at higher magnetic field (0.6 T), when the magnetic field is aligned at 96° (i.e. the field is aligned more parallel to the twin boundary), the direction of net magnetization in the left twin domain is aligned parallel to the field orientation. The average direction of the magnetization deviated in both twin domains markedly from the direction of easy magnetization, i.e. the magnetization was tilted towards the direction of the magnetic field.

7.5 Discussion

The experimental results in Figure 0-3 show that the output voltage linearly increases with increasing frequency at 0.6 T. As the frequency increases, the rate of change of magnetization increases proportionally and so does the output voltage (following Faraday's Law). These results measured at a bias magnetic field at 77° agree with the results reported by Lindquist et. *al.* [51], Karaman et. *al.* [47], and Sayyaadi et. *al.* [103] measured in an orthogonal bias magnetic field. Although a maximum voltage output of 421 ± 0.5 mV was obtained in this study at 0.6 T, this could be enhanced by applying a field of only 0.5 T. We show, in Figure 0-2, that the maximum output voltage was obtained at 0.5 T. With increasing the stroke length, the volume fraction of the crystal re-orientation increases. This implies that the output voltage (and power) increases due to an increase in change of axial magnetization. This is shown in Figure 0-4 where the peak-to-peak displacement is increased to 180 μm, resulting in voltage output enhancement. Also, in Figure 0-4, the output voltage increases when tilting the bias magnetic field in one direction away from orthogonal to the mechanical loading axis. Conversely, the output voltage decreases while tilting the bias magnetic field to the other direction. Guiel *et al.* [101] reported a similar effect of the magnetic field inclination. In addition, Guiel *et al.* showed that the output voltage increases when the magnetic field was tilted so as to become more parallel to the twin boundary as opposed to when tilted so as to become more perpendicular to the twin boundary. We did not identify the orientation of the twin boundaries although from comparison of our results with those of Guiel et. *al.*, we conclude that the twin boundaries were closely parallel to 45° (and not parallel to 135°).

Guiel et. *al*. [101] reported an increase in output voltage from about 27 mV to about 270 mV (RMS voltage) by inclining the magnetic field of 0.7 T to 9.34° from the vertical orientation°. In the present study, with a maximum peak-to-peak displacement of 180 µm, we increased the voltage output to about 130 mV (RMS voltage) at 6° away from the perpendicular bias field. This difference in voltage and field inclination angle from reported values to this present study can be attributed to sample size and other experimental differences. Guiel *et al.* tested a sample with dimensions 20 x 3 x 3 mm^3, which is almost three times longer than the sample of our study and their pick-up coil had 1,000 turns. In addition to the inclined transverse field, they also applied an axial field by placing permanent magnets at the end of the sample. Also, other microstructural aspects such as number of twin boundaries, or the type of twinning may influence the voltage generation.

The numerical simulations show that the change in magnetization parallel to the load axis increases with increasing deformation/strain (Figure 0-5), which implies an increase of power output. The change in magnetization parallel to the load axis is higher at lower bias fields (0.2 T for maximum deformation from 1 and 5% strain) and the maximum value was obtained when the field was inclined at 96°. To explain this drastic increase in magnetization, we use the magnetic structures for 1 and 5% at 0.2 T (Figure 0-6). When the inclination of the biased field was such as to increase the angle between the magnetic field and the twin boundary (i.e. field angle below 90°), the net magnetization parallel to the load axis decreased through the formation of 180° magnetic domains (i.e. growth of blue region in **Error! Reference source not found.**a). This is because the formation of 180° magnetic domains results in regions with reverse magnetization (blue and red regions in **Error! Reference source not found.**a). However, when the biased field inclination was such that the magnetic field direction was more parallel to the twin boundary (i.e. at field inclination angles larger than 90°), the net magnetization parallel to the load axis increased drastically (blue regions in **Error! Reference source not found.**a). This drastic change in orientation of internal magnetization (nearly parallel to the load axis) was observed at smaller strains (when the sample is compressed i.e. at 1% strain Figure 0-6a). At larger strains (i.e. at 5% strain, Figure 0-6b), when the sample is elongated, the magnetization was less affected by the bias field inclination. The reason for the asymmetry with respect to strain is in the orientation of the axis of easy magnetization in the majority twin domain. At 1% strain, the larger twin region is oriented with the *c*-axis parallel to the mechanical loading axis, which results in a large net axial magnetization if one areal fractions of the red and the blue magnetic domains is larger than the other. In contrast, at 5% strain, the larger twin is oriented with the *c*-axis perpendicular to the loading axis. This results in a small axial magnetization component. When the bias magnetic field is perpendicular to the loading axis (90°), the head-to-tail orientation of magnetic moments at the twin boundary between the yellow and the red magnetic domains is energetically favored against the head-to-head configuration between the yellow and the blue magnetic domains. This biases the balance between the fractions of the red and the blue magnetic domains towards red and causes a net axial magnetization. Tilting the magnetic field towards perpendicular to the twin boundary assists this bias and leads to a slight increase of axial magnetization. When tilting the magnetic field towards more parallel to the twin boundary, that bias must be overcome before the blue domain dominates the twin with the axis of easy magnetization parallel to the loading axis.

At higher fields, the Zeeman energy overpowers the magneto-crystalline anisotropy energy. The direction of magnetization tends to align more effectively away from the direction of easy magnetization and in the direction of the external magnetic field. An example of this is shown in Figure 0-7. Due to the influence of the external field, the orientation of magnetization is shifted away from the load axis (or in the direction of the external field), thus reducing the net magnetization in the direction parallel to the load axis (Figure 0-7b). Also, the magnetization direction in both twins is more parallel than perpendicular to each other. Thus, moving the twin boundary causes a lesser change in axial magnetization. Irrespective of the inclination of magnetic field against or along the twin boundary, the net magnetization along the load axis is reduced. This reduced variation in axial magnetization at higher fields results in lower power output compared to lower magnetic fields. This effect is experimentally verified in Figure 0-2 where the voltage generation and power output have a maximum at 0.5 T and decrease at higher magnetic field.

The decrease of voltage generation and power output with the decreasing magnetic field below 0.5 T as determined experimentally (Figure 0-2), results most likely from the reduced effectiveness of the bias magnetic field. To expand the sample against the axial load, the magnetic field must be larger than the switching field, i.e. the magnetostress must overcome the twinning stress [26]. The mechanical hysteresis (Figure 0-1) shows that the twinning stress is about 1 MPa. This corresponds to a switching field of about 300 mT [23]. Thus, below 300 mT, the magnetic field is not sufficient to restore the deformation completely. Additionally, in a configuration with the magnetization perpendicular to the long axis of a sample, the magnetic switching of twin domains is a sluggish process [104]. Thus, it takes a substantially higher magnetic field to completely restore the deformation. Thus, the finite mobility of twin boundaries causes a reduction of change of axial magnetization with decreasing magnetic field. This reduction causes the reduction of Voltage generation and power output. By its nature, the numerical simulations carried out in this study consider static twin patterns. Thus, these numerical simulations do not capture the effect of twin boundary mobility and do not reflect the decrease of change of axial magnetization with decreasing magnetic field.

7.6 Conclusions

We used experimental results to evaluate the effect of various factors such as magnetic field, loading frequency, stroke length, and bias field inclination angle on mechano-electrical energy conversion for a Ni-Mn-Ga alloy transducer. We show in agreement with literature data that the voltage output (and power) can be increased with increasing the loading frequency, stroke length (peak-to-peak displacement), and by changing the orientation of the bias magnetic field parallel to the twin boundary. The results obtained in a fixed setup where the alignment of the sample was not disturbed, remained consistent and were repeatable. However, by removing the sample from the set up or by realigning, the repeatability was compromised. Therefore, the energy conversion is sensitive to many factors such as the sample size, the positioning of the sample within the electromagnets, constraints imposed by fixing the sample, the twin microstructure, and the orientation of the twin boundary with respect to the bias magnetic field inclination.

Using the magnetic domain structures from numerical calculations we analyzed the asymmetry of internal magnetization for various bias magnetic field inclination angles at varying magnitudes of the magnetic field. We conclude that the orientation of internal magnetization is dictated by magneto-crystalline anisotropy at lower fields and by the orientation of the external field at higher magnetic fields (i.e. close to or larger than the saturation field). Also, the power output is maximized at lower magnetic fields (such as 0.2 T or lower than saturation field) due to the increased amount of net magnetization parallel to the load axis. However, reducing the bias magnetic field strength is limited by the twinning stress of the sample. Therefore, in order to generate maximum power output, the energy conversion has to take place at lower magnetic fields and on a sample with low twinning stress.

7.7 Acknowledgements

We acknowledge high-performance computing support of the R2 compute cluster (DOI: 10.18122/B2S41H) provided by Boise State University's Research Computing Department. This research was supported in part by the National Science Foundation under project number DMR-1710640.

CHAPTER EIGHT: CONCLUSIONS AND FUTURE WORK

The main goal of this research was to characterize the magneto-mechanical properties of Ni-Mn-Ga single crystals at mesoscale to explain the experimental findings obtained at macroscale. We analyzed the interactions of magnetic and structural patterns by conducting micromagnetics simulations. Besides the geometric pattern, we analyzed defect energies and energy distributions at magnetic and crystalline interfaces (i.e. twin boundaries).

The sensitivity of twin boundary propagation on sample shape was investigated for designing MSM actuators. A MSM transducer responds differently to a magnetic field parallel and perpendicular to the longest axis of the transducer, namely instantaneously when the magnetic field is parallel and gradually when the magnetic field is perpendicular. At higher magnetic fields, lowering of magnetocrystalline energy is the main driving force for twin boundary motion. At lower fields, the Zeeman energy and the stray field energy also play a role in twin boundary motion. However, the Zeeman and stray field energy are significantly influenced by the demagnetization factor. When the magnetic field is applied in the direction of high demagnetization factor (perpendicular to the long axis of the sample), 180° magnetic domains form (in an attempt to lower the stray field energy) resulting in heightened Zeeman energy regions. As a consequence, gradual actuation occurs. The absence of these local (on the strain axis) energy maxima results in spontaneous actuation (magnetic field parallel to the long axis of the sample, in the direction of low demagnetization factor).

Future work may develop more designing strategies for MSM actuators. For example, the actuation of the MSM micropump [3] requires a localized, non-homogeneous magnetic field. Whereas, the studies in this dissertation consider a homogeneous magnetic field. The micromagnetics code has to be modified to study magnetic responses in an inhomogeneous magnetic field. In order to do that, an input file should be defined with varying magnetic field vectors on each simulation cell. J. Tellinen [3] calculated the distribution of the magnetic field for a shrinkage area in a MSM micropump. From these calculations, Ullako *et al.* reported that perpendicular flux lines are concentrated at the shrinkage and at several millimeters from the shrinkage horizontal flux lines were observed. These flux densities were high enough to generate a shrinkage region i.e. the two twin boundaries (one twin domain) create a shrinkage. By using these reported studies as a reference an optimum twin width (distance between two twin boundaries that cause the shrinkage) and magnetic field orientation could be identified for most the efficient actuation in a MSM micropump or similar settings.

The mechanical behavior of Ni-Mn-Ga single crystals with varying twin densities was studied by interpreting the mesoscale magnetic domain and twin boundary interactions. As the twinned regions get finer, the simulated magnetic structures revealed the formation of additional magnetic domains. These additional domains break the symmetry across the twin boundary with magnetic moments aligned parallel to the twin boundary whereas, in the rest of the sample, the magnetic moments align parallel to the *c*-axis i.e. aligned perpendicular to the twin boundary. Numerous sites where the twin boundaries interact with these newly formed magnetic domains become sources of magnetoelastic defects (due to magnetization perpendicular to the axis of easy magnetization). These defects generate local spatial energy gradients and concentrations of magnetostress that hinder twin boundary mobility and result in work hardening-like behavior. With increasing twin density the effectivity of these magnetoelastic obstacles increases. The obstacles are more effective because the number of twinning disconnections between the defects decreases with increasing twin density. The stress driving a disconnection against an obstacle (or defect) is proportional to the external stress and the number of disconnections piling up at this obstacle.

This study concluded that the mechanical response of the MSM alloy is related to the number of twin boundaries in a sample. We assumed that all the twin boundaries are parallel and inclined at 45° to the long edge of the sample. However, this is not always the case. A sample can contain a more complex twin microstructure with twin boundaries that are randomly oriented. A future study may address the mechanical response when the twin boundaries intersect. These complex microstructures may potentially add more defects in the system which will alter the magnetic and the mechanical behavior of MSM alloys. There is also interest in understanding the mechanical behavior of a fine twinned MSM alloy in the presence of a magnetic field that is biased perpendicular to its loading direction. These details are not addressed in this dissertation and thus, leaves a scope for studying the magnetic interactions of different twin boundary orientations, their mutual interactions when they intersect, in a homogeneous and inhomogenous distribution of internal magnetic fields.

Using the concept of inverse magnetoplasticity, the power harvesting capacity of MSM alloys in an inclined magnetic field was evaluated by performing experiments and simulations. The power output of the MSM alloy increases with increasing stroke length (or peak to peak displacement), and when the biased magnetic field is inclined with respect to the loading direction. At lower fields, the magnetization in the sample is governed by the magneto-crystalline anisotropy that results in net magnetization parallel to the loading direction. As a consequence the power output increases and is more strongly asymmetrical about 90°. Whereas at higher fields, the external magnetic field magnetizes the sample in the direction of the field thereby resulting symmetry about 90°.

We examined the asymmetric power harvesting behavior in a single twin boundary system. This study may be extended to evaluate the power generation capabilities for a densely twinned MSM alloy. A staircase-like magnetic domain structure was obtained for fine twinned MSM alloys (in the absence of external magnetic field, Appendix C) in a part of research that was done in completing this dissertation. The continuation to this study would be to examine the power generation capabilities with such a domain pattern in the presence of an incline magnetic field.

We limited the scope on studying flat twin boundaries. When twin boundaries encounter large obstacles (e.g. blocking obstacle twins and substantially constrained surfaces, e.g. [105]) they tend to bend. On a microscopic scale, such bent twin boundaries contain steps (disconnections) and terraces. Researchers have studied the effect of stress on the shape of twin boundaries (e.g. [106]). Future work may address the effect of a magnetic field on the shape of a blocked twin. To do this, one must reduce the grid size to the size of a disconnection step height. With such a model, one may quantitatively assess magentoelastic properties (as opposed to magnetoplastic properties), which occur in heavily twinned samples with crossing twins [94] and constrained surfaces [107].

REFERENCES:

[1] I. Suorsa, E. Pagounis, K. Ullakko, Magnetic shape memory actuator performance, J. Magn. Magn. Mater. 272–276 (2004) 2029–2030. doi:10.1016/j.jmmm.2003.12.1026.

[2] N.N. Sarawate, M.J. Dapino, Magnetization dependence on dynamic strain in ferromagnetic shape memory Ni-Mn-Ga, Appl. Phys. Lett. 93 062501 (2008). doi:10.1063/1.2969799.

[3] K. Ullakko, L. Wendell, A. Smith, P. Müllner, G. Hampikian, A magnetic shape memory micropump: Contact-free, and compatible with PCR and human DNA profiling, Smart Mater. Struct. 21 (2012). doi:10.1088/0964-1726/21/11/115020.

[4] K. Ullakko, Magnetically controlled shape memory alloys: A new class of actuator materials, J. Mater. Eng. Perform. 5 (1996) 405–409. doi:10.1007/BF02649344.

[5] K. Ullakko, J. K. Huang, C. Kantner, R. C. O'Handley, V. V. Kokorin, Large magnetic-field-induced strains in Ni2MnGa single crystals, Appl. Phys. Lett. 69 (1996). doi:10.1063/1.117637.

[6] S.J. Murray, M. Marioni, S.M. Allen, R.C. O'Handley, T.A. Lograsso, 6% magnetic-field-induced strain by twin-boundary motion in ferromagnetic Ni-Mn-Ga, Appl. Phys. Lett. 77 (2000) 886–888. doi:10.1063/1.1306635.

[7] A. Sozinov, A. A. Likhachev, N. Lanska, K. Ullakko, Giant magnetic-field-induced strain in NiMnGa seven-layered martensitic phase, Appl. Phys. Lett. 80 1746 (2002) 1746–1748. doi:10.1063/1.1458075.

[8] A. Sozinov, N. Lanska, A. Soroka, W. Zou, 12% magnetic field-induced strain in Ni-Mn-Ga-based non-modulated martensite, Appl. Phys. Lett. 102 021902 (2013). doi:10.1063/1.4775677.

[9] P. Müllner, V.A. Chernenko, G. Kostorz, A microscopic approach to the magnetic-field-induced deformation of martensite (magnetoplasticity), J. Magn. Magn. Mater. 267 (2003) 325–334. doi:10.1016/S0304-8853(03)00400-1.

[10] J. Tellinen, I. Suorsa, I. Aaltio, K. Ullakko, Basic Properties of Magnetic Shape Memory Actuators, 8th Int. Conf. ACTUATOR 2002. (2002) 10–12.

[11] D.I. Paul, J. Marquiss, D. Quattrochi, Theory of magnetization: Twin boundary interaction in ferromagnetic shape memory alloys, J. Appl. Phys. 93 4561 (2003) 4561–4565. doi:10.1063/1.1561993.

[12] J.X. Zhang, L.Q. Chen, Phase-field model for ferromagnetic shape-memory alloys, Philos. Mag. Lett. 85 (2005) 533–541. doi:10.1080/09500830500385527.

[13] Q. Peng, J. Huang, M. Chen, Effects of demagnetization on Magnetic-Field-Induced Strain and microstructural evolution in Ni-Mn-Ga Ferromagnetic Shape Memory Alloy by phase-field simulations, Mater. Design 107 (2016) 361–370. doi:10.1016/j.matdes.2016.06.050.

[14] Y.M. Jin, Effects of twin boundary mobility on domain microstructure evolution in magnetic shape memory alloys: Phase field simulation, Appl. Phys. Lett. 94 062508 (2009). doi:10.1063/1.3081011.

[15] Q. Peng, Q. Sun, M. Chen, Phase-field simulations of partial pseudoelastic stress-strain behavior and microstructure evolution of Ni-Mn-Ga, Mater. Sci. Eng. A. 669 (2016) 428–436. doi:10.1016/j.msea.2016.05.099.

[16] Q. Peng, J. Huang, M. Chen, Q. Sun, Phase-field simulation of magnetic hysteresis and mechanically induced remanent magnetization rotation in Ni-Mn-Ga ferromagnetic shape memory alloy, Scr. Mater. 127 (2017) 49–53. doi:10.1016/j.scriptamat.2016.08.033.

[17] A. Aharoni, Micromagnetics: Past, present and future, Phys. B Condens. Matter. 306 (2001) 1–9. doi:10.1016/S0921-4526(01)00954-1.

[18] A. Hobza, C.J. García-Cervera, P. Müllner, Twin-enhanced magnetic torque, J. Magn. Magn. Mater. 458 (2018) 183–192. doi:10.1016/j.jmmm.2018.03.014.

[19] C.J. García-cervera, E. Weinan, Improved Gauss – Seidel Projection Method for Micromagnetics Simulations, IEEE Trans. Magn. 39 (2003) 1766–1770. doi:10.1109/TMAG.2003.810610.

[20] I could not find an author, Physics stack exchange, (n.d.). https://physics.stackexchange.com (accessed April 13, 2018).

[21] W. D. Callister Jr., D. G. Rethwisch, Material science and engineering: An introduction 9th edition, John Wiley & Sons, New York, 1997.

[22] N.I. Glavatska, A.A. Rudenko, I.N. Glavatskiy, V.A. L'vov, Statistical model of magnetostrain effect in martensite, J. Magn. Magn. Mater. 265 (2003) 142–151. doi:10.1016/S0304-8853(03)00242-7.

[23] V. A. Chernenko, V. A. L’vov, P. Mullner, G. Kostorz, T. Takagi, Magnetic-field-induced superelasticity of ferromagnetic thermoelastic martensites: Experiment and modeling, Phys. Rev. B. 69 134410 (2004) 1–8. doi:10.1103/PhysRevB.69.134410.

[24] P. Müllner, Twinning stress of type I and type II deformation twins, Acta Mater.

176 (2019) 211–219. doi:10.1016/j.actamat.2019.07.004.

[25] H.E. Karaca, I. Karaman, B. Basaran, Y.I. Chumlyakov, H.J. Maier, Magnetic field and stress induced martensite reorientation in NiMnGa ferromagnetic shape memory alloy single crystals, Acta Mater. 54 (2006) 233–245. doi:10.1016/j.actamat.2005.09.004.

[26] P. Müllner, V. A. Chernenko, M. Wollgarten, G. Kostorz, Large cyclic deformation of a Ni-Mn-Ga shape memory alloy induced by magnetic, J. Appl. Phys. 92 (2002) 6708–6713. doi:10.1063/1.1513875.

[27] O. Heczko, O. Perevertov, D. Král, M. Veis, I. V. Soldatov, R. Schäfer, Using Kerr Microscopy for Direct Observation of Magnetic Domains in Ni-Mn-Ga Magnetic Shape Memory Alloy, IEEE Trans. Magn. 53 (2017) 1–5. doi:10.1109/TMAG.2017.2707486.

[28] D. Niklasch, H.J. Maier, I. Karaman, Design and application of a mechanical load frame for in situ investigation of ferromagnetic shape memory alloys by magnetic force microscopy, Rev. Sci. Instrum. 79 113701 (2008) 2–5. doi:10.1063/1.3010383.

[29] Y. Ge, O. Heczko, O. Söderberg, S.P. Hannula, V.K. Lindroos, Investigation of magnetic domains in Ni-Mn-Ga alloys with a scanning electron microscope, Smart Mater. Struct. 14 (2005). doi:10.1088/0964-1726/14/5/007.

[30] Y. Ge, O. Heczko, O. Söderberg, S.P. Hannula, Direct optical observation of magnetic domains in Ni-Mn-Ga martensite, Appl. Phys. Lett. 89 082502 (2006). doi:10.1063/1.2335811.

[31] Y. Ge, O. Heczko, O. Söderberg, S.P. Hannula, Comparison of different methods

for studying magnetic domains in Ni-Mn-Ga martensites, Mater. Sci. Eng. A. 481–482 (2008) 302–305. doi:10.1016/j.msea.2006.11.183.

[32] Y.W. Lai, R. Schäfer, L. Schultz, J. McCord, Volume magnetic domain mirroring in magnetic shape memory crystals, Appl. Phys. Lett. 96 022507 (2010). doi:10.1063/1.3292205.

[33] Y.W. Lai, R. Schäfer, L. Schultz, J. McCord, Direct observation of AC field-induced twin-boundary dynamics in bulk NiMnGa, Acta Mater. 56 (2008) 5130–5137. doi:10.1016/j.actamat.2008.06.030.

[34] Y. W. Lai, N. Scheerbaum, D. Hinz, O. Gutfleisch, R. Schäfer, L. Schultz, J. McCord, Absence of magnetic domain wall motion during magnetic field induced twin boundary motion in bulk magnetic shape memory alloys, Appl. Phys. Lett. 90 192504 (2007). doi:10.1063/1.2737934.

[35] M. Reinhold, W.B. Knowlton, P. Müllner, Characterizing Twin Structure and Magnetic Domain Structure of Ni-Mn-Ga through Atomic Force Microscopy, Icomat-08, St Fe NM (2010). (2013) 299–304. doi:10.1002/9781118803592.ch42.

[36] S.P. Venkateswaran, N.T. Nuhfer, M. De Graef, Magnetic domain memory in multiferroic Ni2MnGa, Acta Mater. 55 (2007) 5419–5427. doi:10.1016/j.actamat.2007.05.055.

[37] S.P. Venkateswaran, N.T. Nuhfer, M. De Graef, Anti-phase boundaries and magnetic domain structures in Ni2MnGa-type Heusler alloys, Acta Mater. 55 (2007) 2621–2636. doi:10.1016/j.actamat.2006.12.003.

[38] Y. Ge, O. Heczko, O. Söderberg, V.K. Lindroos, Various magnetic domain structures in a Ni – Mn – Ga martensite exhibiting magnetic shape memory effect,

J. Appl. Phys. 96 2159 (2004). doi:10.1063/1.1773381.

[39] Q. Peng, Y.J. He, Z. Moumni, A phase-field model on the hysteretic magneto-mechanical behaviors of ferromagnetic shape memory alloy, Acta Mater. 88 (2015) 13–24. doi:10.1016/j.actamat.2015.01.044.

[40] J.-H. Lin, M.-H. Chiang, Hysteresis Analysis and Positioning Control for a Magnetic Shape Memory Actuator, Sensors(Basel) (2015). 8054-8071. doi:10.3390/s150408054.

[41] N. Gabdullin, S.H. Khan, Review of properties of magnetic shape memory (MSM) alloys and MSM actuator designs, J. Phys. Conf. Ser. 588 (2015). doi:10.1088/1742-6596/588/1/012052.

[42] S.A. Wilson, R.P.J. Jourdain, Q. Zhang, R.A. Dorey, C.R. Bowen, M. Willander, Q.U. Wahab, M. Willander, S.M. Al-hilli, O. Nur, E. Quandt, C. Johansson, E. Pagounis, M. Kohl, J. Matovic, B. Samel, W. van der Wijngaart, E.W.H. Jager, D. Carlsson, Z. Djinovic, M. Wegener, C. Moldovan, R. Iosub, E. Abad, M. Wendlandt, C. Rusu, K. Persson, New materials for micro-scale sensors and actuators, Mater. Sci. Eng. R Reports. 56 (2007) 1–129. doi:10.1016/j.mser.2007.03.001.

[43] E. Pagounis, P. Müllner, Oral Contributions A1 Piezoactuators I, Materials and Actuator Solutions for Advanced Magnetic Shape Memory Devices (Review), ACTUATOR: 16th International Conference on New Actuators, Berman, Germany, 25-27 June (2018) 25–27.

[44] C. Titsch, M. Veligatla, C.J. Garcia-Cervera, W.-G. Drossel, P. Müllner, Mechanical switching behavior of a Ni-Mn-Ga single crystal in magnetic fields

with different directions, ACTUATOR: 16th International Conference on New Actuators, Bremen, Germany, 25-27 June 2018 : interactive conference proceedings.

[45] A. Hobza, C.L. Patrick, K. Ullakko, N. Rafla, P. Lindquist, P. Müllner, Sensing strain in Ni-Mn-Ga, Sensors Actuators A Phys. 269 (2018) 137-144. doi:10.1016/j.sna.2017.11.002.

[46] J.M. Stephan, E. Pagounis, M. Laufenberg, O. Paul, P. Ruther, A novel concept for strain sensing based on the ferromagnetic shape memory alloy NiMnGa, IEEE Sens. J. 11 (2011) 2683–2689. doi:10.1109/JSEN.2011.2157489.

[47] I. Karaman, B. Basaran, H. E. Karaca, A. I. Karsilayan, Y. I. Chumlyakov, Energy harvesting using martensite variant reorientation mechanism in a NiMnGa magnetic shape memory alloy, J. Appl. Phys. Lett. 90 172505 (2007) 1–4. doi:10.1063/1.2721143.

[48] D. Carpenter, M. Chemielus, A. Rothenbühler, R. Schneider, P. Müllner, Application of ferromagnetic shape memory alloys in power generation devices, Proc. Int. Conf. Maartensitic Transform. “ICOMAT-08”, St. Fe, NM. (2008) 365–369.

[49] N.M. Bruno, C. Ciocanel, H.P. Feigenbaum, A. Waldauer, A theoretical and experimental investigation of power harvesting using the NiMnGa martensite reorientation mechanism, Smart Mater. Struct. 21 (2012). doi:10.1088/0964-1726/21/9/094018.

[50] I. Suorsa, J. Tellinen, K. Ullakko, E. Pagounis, Voltage generation induced by mechanical straining in magnetic shape memory materials, J. Appl. Phys. 95 8054

(2004). doi:10.1063/1.1711181.

[51] P. Lindquist, T. Hobza, C. Patrick, P. Müllner, Efficiency of Energy Harvesting in Ni – Mn – Ga Shape Memory Alloys, Shap. Mem. Superelasticity 4 (2018) 93–101. doi:10.1007/s40830-018-0158-z.

[52] M. Kohl, R. Z. Yin, V. Pinneker, Y. Ezer, A. Sozinov, A miniature energy harvesting device using martensite variant reorientation, Mater. Sci. Forum. 738–739 (2013) 411–415. doi:10.4028/www.scientific.net/MSF.738-739.411.

[53] V. Kopecky, K. Jurek, J. Kopecek, L. Straka, H. Seiner, O. Heczko, Magnetic domains and twin microstructure of single crystal Ni-Mn-Ga exhibiting magnetic shape memory effect, IEEE INTERMAG, Beijing China (2015). doi:10.1109/TMAG.2015.2453054.

[54] L. Straka, N. Lanska, K. Ullakko, A. Sozinov, Twin microstructure dependent mechanical response in Ni – Mn – Ga single crystals, J. Appl. Phys. Lett. 96 131903 (2010) 131903 1–3. doi:10.1063/1.3373608.

[55] O. Perevertov, O. Heczko, R. Schäfer, Direct observation of magnetic domains by Kerr microscopy in a Ni-Mn-Ga magnetic shape-memory alloy, Phys. Rev. B 144431 (2017) 1–5. doi:10.1103/PhysRevB.95.144431.

[56] W.F. Brown Jr., Domains, micromagnetics, and beyond: Reminiscences and assessments, J. Appl. Phys. 49 (1978) 1937–1942. doi:10.1063/1.324811.

[57] R. Tickle, R.D. James, T. Shield, M. Wuttig, V. V. Kokorin, Ferromagnetic shape memory in the NiMnGa system, IEEE Trans. Magn. 35 (1999) 4301–4310. doi:10.1109/20.799080.

[58] V. Runov, U. Stuhr, Neutron spectroscopy study of magnons in the austenite and

martensite phases of a NiMnGa Heusler alloy, J. Magn. Magn. Mater. 323 (2011) 244–247. doi:10.1016/j.jmmm.2010.09.013.

[59] L. Straka and O. Heczko, Magnetic anisotropy in Ni – Mn – Ga martensites, 93 (2003) 8636–8638. doi:10.1063/1.1555982.

[60] O. Söderberg, Y. Ge, A. Sozinov, S.P. Hannula, V.K. Lindroos, Recent breakthrough development of the magnetic shape memory effect in Ni-Mn-Ga alloys, Smart Mater. Struct. 14 (2005). doi:10.1088/0964-1726/14/5/009.

[61] A. Saren, T. Nicholls, J. Tellinen, K. Ullakko, Direct observation of fast-moving twin boundaries in magnetic shape memory alloy Ni–Mn–Ga 5 M martensite, Scr. Mater. 123 (2016) 9–12. doi:10.1016/j.scriptamat.2016.04.004.

[62] E. Pagounis, R. Chulist, M.J. Szczerba, M. Laufenberg, High-temperature magnetic shape memory actuation in a Ni-Mn-Ga single crystal, Scr. Mater. 83 (2014) 29–32. doi:10.1016/j.scriptamat.2014.04.001.

[63] L. Sturz, A. Drevermann, U. Hecht, E. Pagounis, M. Laufenberg, Production and characterization of large single crystals made of ferromagnetic shape memory alloys Ni-Mn-Ga, Phys. Procedia. 10 (2010) 81–86. doi:10.1016/j.phpro.2010.11.079.

[64] D.C. Dunand, P. Müllner, Size effects on magnetic actuation in Ni-Mn-Ga shape-memory alloys, Adv. Mater. 23 (2011) 216–232. doi:10.1002/adma.201002753.

[65] B. Holz, H. Janocha, L. Riccardi, Compact MSM Actuators – Concept for Highest Force Exploitation, Proc. ACTUATOR: International Conference on New Actuators and Drives (2012).

[66] M. Kohl, M. Gueltig, V. Pinneker, R. Yin, F. Wendler, B. Krevet, Magnetic shape

memory microactuators, Micromachines 5 (2014) 1135–1160. doi:10.3390/mi5041135.

[67] K. Ullakko, J.K. Huang, V. V. Kokorin, R.C. O'Handley, Magnetically controlled shape memory effect in Ni2MnGa intermetallics, Scr. Mater. 36 (1997) 1133–1138. doi:10.1016/S1359-6462(96)00483-6.

[68] A.R. Smith, J. Tellinen, K. Ullakko, Rapid actuation and response of Ni – Mn – Ga to magnetic-field-induced stress, Acta Mater. 80 (2014) 373–379. doi:10.1016/j.actamat.2014.06.054.

[69] J. Fidler, R.W. Chantrell, T. Schrefl, M.A. Wongsam, Micromagnetics: Basic Principles, Encycl. Mater. Sci. Technol. (2001) 5642–5650. doi:10.1016/b0-08-043152-6/00984-0.

[70] A. Hobza, P. Müllner, Magnetic Torque in Single Crystal Ni–Mn–Ga, Shape Mem. Superelasticity. 3 (2017) 139–148. doi:10.1007/s40830-017-0106-3.

[71] Y.M. Jin, Y.U. Wang, A. Kazaryan, Y. Wang, D.E. Laughlin, A.G. Khachaturyan, Magnetic structure and hysteresis in hard magnetic nanocrystalline film: Computer simulation, J. Appl. Phys. 92 (2002) 6172–6181. doi:10.1063/1.1510955.

[72] H.B. Huang, X.Q. Ma, J.J. Wang, Z.H. Liu, W.Q. He, L.Q. Chen, A phase-field model of phase transitions and domain structures of NiCoMnIn metamagnetic alloys, Acta Mater. 83 (2015) 333–340. doi:10.1016/j.actamat.2014.10.014.

[73] Y.M. Jin, Effects of magnetostatic interaction on domain microstructure evolution in magnetic shape memory alloys : Phase field simulation, Phil. Mag. 6435 (2010) 169-176. doi:10.1080/14786430902758671.

[74] C.J. Garcia-Cervera, Numerical Micromagnetics : A Review, Bol. Soc. Esp. Mat.

Apl. 0 (2007) 1–33.

[75] E. Faran, I. Benichou, S. Givli, D. Shilo, The effects of magnetic and mechanical microstructures on the twinning stress in Ni-Mn-Ga, J. Appl. Phys. 118 244104 (2015). doi:10.1063/1.4939179.

[76] K. Schlüter, B. Holz, A. Raatz, Principle Design of Actuators Driven by Magnetic Shape Memory Alloys, Adv. Eng. Mater. 14 (2012) 682–686. doi:https://doi.org/10.1002/adem.201200078.

[77] M. Acet, Ll. Mañosa, A. Planes, Magnetic-Field-Induced Effects in Martensitic Heusler-Based Magnetic Shape Memory Alloys, Handbook of Magnetic Materials 19 (2011) 231-289. doi:10.1016/B978-0-444-53780-5.00004-1.

[78] L. Straka, O. Heczko, H. Hänninen, Activation of magnetic shape memory effect in Ni – Mn – Ga alloys by mechanical and magnetic treatment, Acta Mater. 56 (2008) 5492–5499. doi:10.1016/j.actamat.2008.07.020.

[79] N.J. Kucza, C.L. Patrick, D.C. Dunand, P. Müllner, Magnetic-field-induced bending and straining of Ni – Mn – Ga single crystal beams with high aspect ratios, Acta Mater. 95 (2015) 284–290. doi:10.1016/j.actamat.2015.05.030.

[80] I. Suorsa, E. Pagounis, Magnetic field-induced stress in the Ni – Mn – Ga magnetic shape memory alloy, J. Appl. Phys. 95 (2004) 4958–4961. doi:10.1063/1.1697617.

[81] O. Heczko, K. Jurek, K. Ullakko, Magnetic properties and domain structure of magnetic shape memory Ni-Mn-Ga alloy, J. Magn. Magn. Mater. 226-230 (2001) 996–998.

[82] Y. Ge, O. Heczko, O. Söderberg, S-P. Hannula, V. K. Lindroos, Investigation of

magnetic domains in Ni – Mn – Ga alloys with a scanning electron microscope, Smart Mater. Struct. 14 (2005) S211–S215. doi:10.1088/0964-1726/14/5/007.

[83] A. Sozinov, Y. Ezer, G. Kimmel, P. Yakovenko, D. Giller, Y. Wolfus, Y. Yeshurun, K. Ullakko, V. K. Lindroos, Large magnetic-field-induced strains in Ni-Mn-Ga alloys in rotating magnetic field, J. Phys. IV France 11 (2001) 311–316.

[84] O. Heczko, L. Straka, H. Seiner, Different microstructures of mobile twin boundaries in 10 M modulated Ni – Mn – Ga martensite, Acta Mater. 61 (2013) 622–631. doi:10.1016/j.actamat.2012.10.007.

[85] L. Straka, A. Soroka, H. Seiner, H.Hänninen, A.Sozinov, Temperature dependence of twinning stress of Type I and Type II twins in 10M modulated Ni – Mn – Ga martensite, Scr. Mater. 67 (2012) 25–28. doi:10.1016/j.scriptamat.2012.03.012.

[86] R. Chulist, L. Straka, N. Lanska, A. Soroka, A. Sozinov, W. Skrotzki, Characterization of mobile type I and type II twin boundaries in 10M modulated Ni – Mn – Ga martensite by electron backscatter diffraction, Acta Mater. 61 (2013) 1913–1920. doi:10.1016/j.actamat.2012.12.012.

[87] A. Sozinov, N. Lanska, A. Soroka, L. Straka, Highly mobile type II twin boundary in Ni- Mn-Ga five-layered martensite, Appl. Phys. Lett. 99 124103 (2011). doi:10.1063/1.3640489.

[88] L. Straka, H Hänninen, A Soroka, A Sozinov, Ni-Mn-Ga single crystals with very low twinning stress Ni-Mn-Ga single crystals with very low twinning stress, J. Phys. Conf. Ser. 303 (2011). doi:10.1088/1742-6596/303/1/012079.

[89] O. Heczko, P. Veřtát, M. Vronka, V. Kopecky, O. Perevertov, Ni – Mn – Ga Single Crystal Exhibiting Multiple Magnetic Shape Memory Effects, Shap. Mem.

and Superelasticity 2 (2016) 272–280. doi:10.1007/s40830-016-0077-9.

[90] K. Otsuka and C. M. Wayman, Shape Memory Materials, Cambridge University Press, U.K, 1998.

[91] R.C. Pond, B. Muntifering, P. Müllner, Deformation twinning in Ni_2MnGa, 60 (2012) 3976–3984. doi:10.1016/j.actamat.2012.03.045.

[92] J .W. Christian, S. Mahajan, Deformation Twinning, Prog. Mater. Sci. 39 (1995) 1–157.

[93] S. Rajasekhara, P.J. Ferreira, A dislocation model for the magnetic field induced shape memory effect in Ni_2MnGa, Scr. Mater. 53 (2005) 817–822. doi:10.1016/j.scriptamat.2005.06.003.

[94] P. Müllner, G. Kostorz, Microstructure of magnetic shape-memory alloys: between magnetoelasticity and magnetoplasticity, Mater. Sci. Forum. 583 (2008) 43–65.

[95] J. P. Hirth, J. Lothe, Theory of Dislocations, 2nd ed., Krieger Publishing Company, Florida, 1982.

[96] P. Müllner, C. Solenthaler, A proper model of a deformation twin for twin-intersection problems, Philos. Mag. Lett. 69 (1994) 111–113.

[97] P. Müllner, V. A. Chernenko, G. Kostorz, Stress-induced twin rearrangement resulting in change of magnetization in a Ni – Mn – Ga ferromagnetic martensite, Scr. Mater. 49 (2003) 129–133. doi:10.1016/S1359-6462(03)00219-7.

[98] L. Straka, H. Hänninen, N. Lanska, A. Sozinov, Twin interaction and large magnetoelasticity in Ni-Mn-Ga single crystals, J. Appl. Phys. 109 063504 (2011). doi:10.1063/1.3552292.

[99] N. Bruno, C. Ciocanel, H. Feigenbaum, Electromitive force generation using the

dynamic response if $Ni_{50}Mn_{28}.5Ga_{21.5}$ magnetic shape memory alloy, Conf. Proc. SPIE. 79781P (2011). doi:10.1117/12.881294.

[100] I. Nelson, J. Dikes, H. Feigenbaum, C. Ciocanel, Numerical predictions versus experimental findings on the power-harvesting output of a NiMnGa alloy, Behav. Mech. Multifunct. Mater. Compos. 2014. 9058 (2014) 905815. doi:10.1117/12.2046337.

[101] R. Guiel, H. Feigenbaum, C. Ciocanel, The effect of magnetic field orientation on the open-circuit voltage of Ni – Mn – Ga based power harvesters, Smart Mater. Struct. 27 (2018) 1–15.

[102] D. Kellis, A. Smith, K. Ullakko, P. Müllner, Oriented single crystals of Ni – Mn – Ga with very low switching field, 359 (2012) 64–68. doi:10.1016/j.jcrysgro.2012.08.014.

[103] H. Sayyaadi, M.A.A. Farsangi, Frequency-dependent energy harvesting via magnetic shape memory alloys, Smart Mater. Struct. 24 (2015). doi:10.1088/0964-1726/24/11/115022.

[104] M. Veligatla, Christian Titsch, Welf-Guntram Drossel, Carols J. Garcia-Cervera, P. Müllner, Sensitivity of twin boundary movement to sample shape in Ni-Mn-Ga, Acta. Mater. (2019) - *Under review*.

[105] B. Muntifering, R.C. Pond, L. Kovarik, N.D. Browning, P. Müllner, Intra-variant substructure in N-Mn-Ga martensite: Conjugation boundaries, Acta Mater. 71 (2014) 255–263. doi:10.1016/j.actamat.2014.03.018.

[106] S. V. Kamat, J. P. Hirth, P. Müllner, The effect of stress on a blocked deformation twin, Philos. Mag. A. 73 (1996) 669-680. doi:10.1080/01418619608242989.

[107] M. Chmielus, C. Witherspoon, K. Ullakko, P. Müllner, R. Schneider, Effects of surface damage on twinning stress and the stability of twin microstructures of magnetic shape memory alloys, Acta Mater. 59 (2011) 2948–2956. doi:10.1016/j.actamat.2011.01.035.

APPENDIX A

Sample Dimensions and its Corresponding Twin Fractions with Respect to Strain for CHAPTER FIVE

Table A-1: Simulated sample sizes and twin fractions corresponding to strain

Strain (%)	**Length (µm)**	**Width (µm)**	**Twin fraction (f_1)**
0	1.55	0.517	1
0.5	1.56	0.533	0.91
1	1.568	0.530	0.83
1.5	1.57	0.528	0.75
2	1.58	0.525	0.67
2.5	1.59	0.522	0.58
3	1.60	0.52	0.5
3.5	1.60	0.517	0.41
4	1.61	0.514	0.33
4.5	1.62	0.511	0.25
5	1.63	0.509	0.17
5.5	1.63	0.506	0.08
6	1.64	0.503	0

APPENDIX B

Magnetic Structure Resolving Limitations

Limitations on magnetic domain evolution with respect to the number of cells in a simulating sample were discovered while studying the magnetic domain evolution for dense twin microstructures.

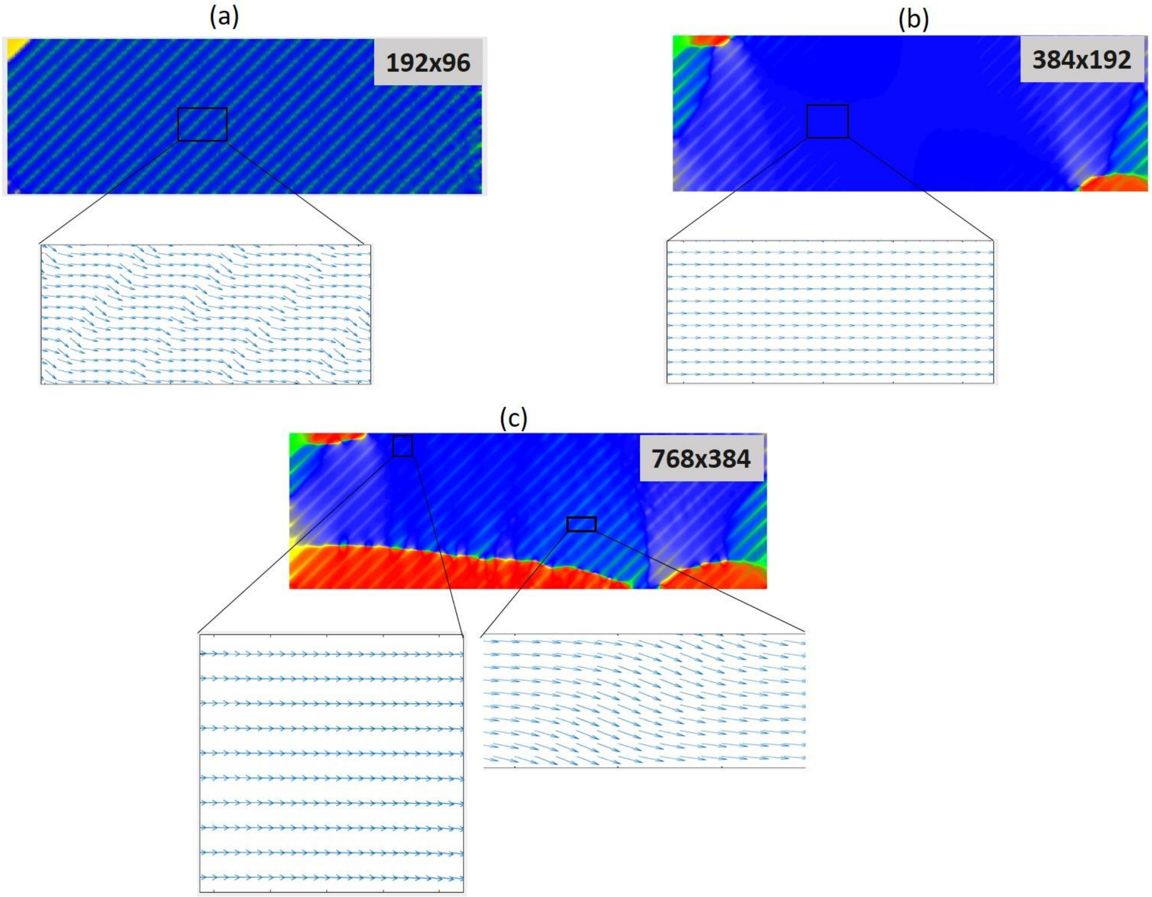

Figure B-1 Equilibrium magnetic structures for (a) cell size = 192 x 96, (b) cell size = 384 x 192, and (c) 768 x 384 on a sample strained to 3 % with 65 twin boundaries.

APPENDIX C

Supporting Data CHAPTER SIX

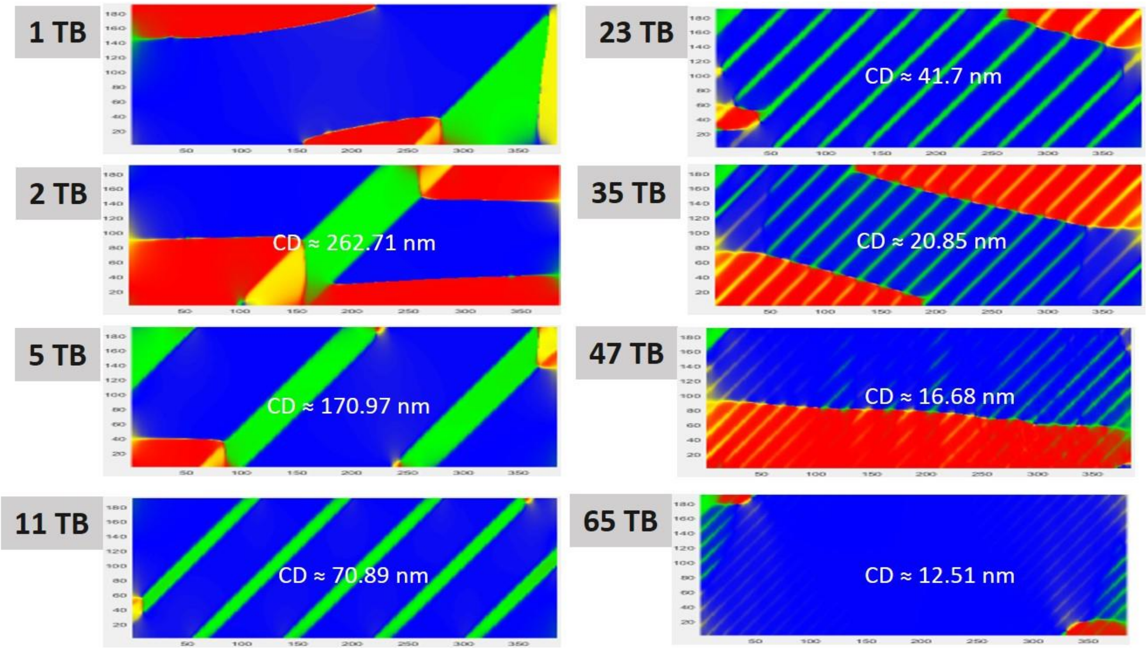

Figure C-1 Equilibrium magnetic domain structure evolution with increasing twin boundaries (or twin densities) from 1 to 65 (or 1.7 to 47 μm^{-1}) for a sample strained to 1%. "CD" denotes the closest distance between two twin boundaries.

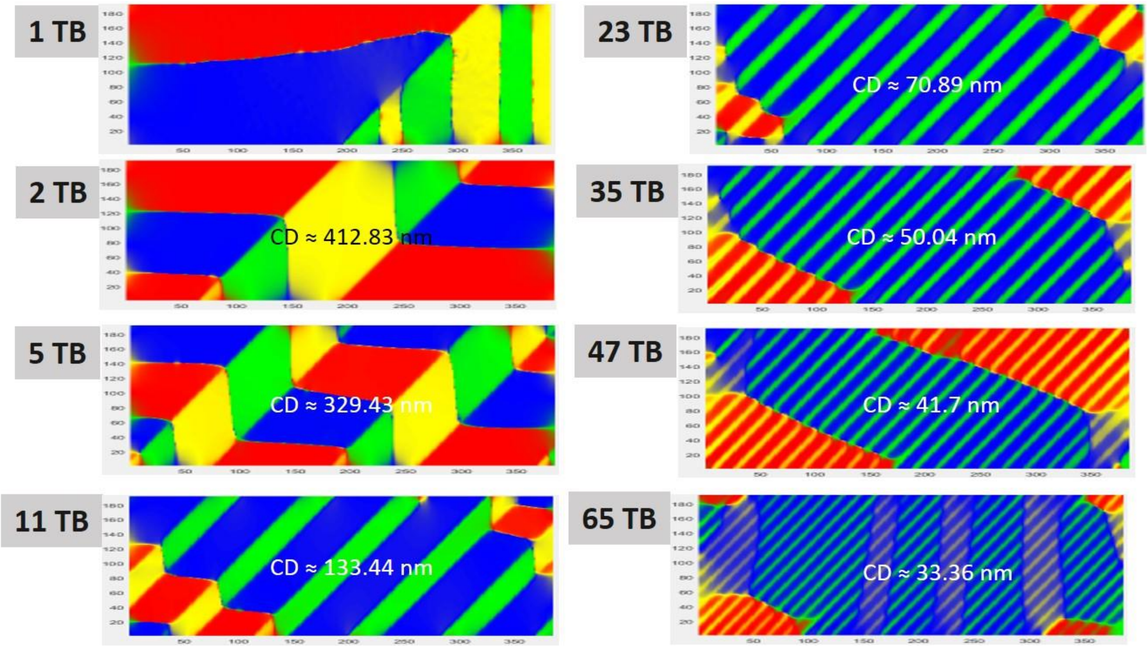

Figure C-2 Equilibrium magnetic domain structures evolution with increasing twin boundaries (or twin densities) from 1 to 65 (or 1.7 to 47 μm^{-1}) for a sample strained to 2%. "CD" denotes the closest distance between two twin boundaries.

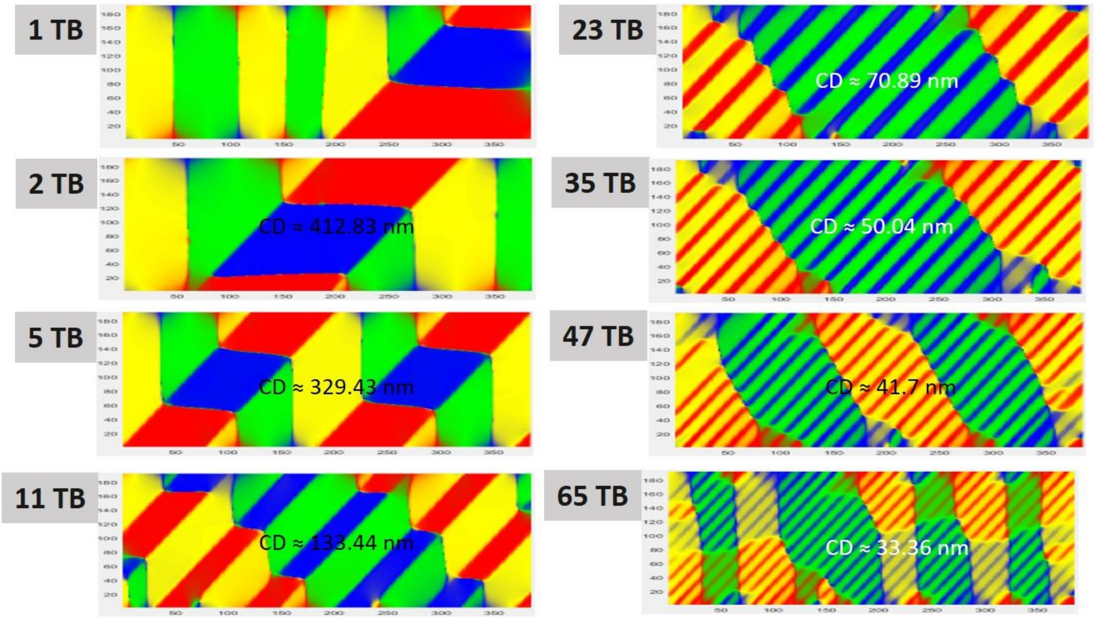

Figure C-3 Equilibrium magnetic domain structures evolution with increasing twin boundaries (or twin densities) from 1 to 65 (or 1.7 to 47 μm^{-1}) for a sample strained to 4%. “CD” denotes the closest distance between two twin boundaries.

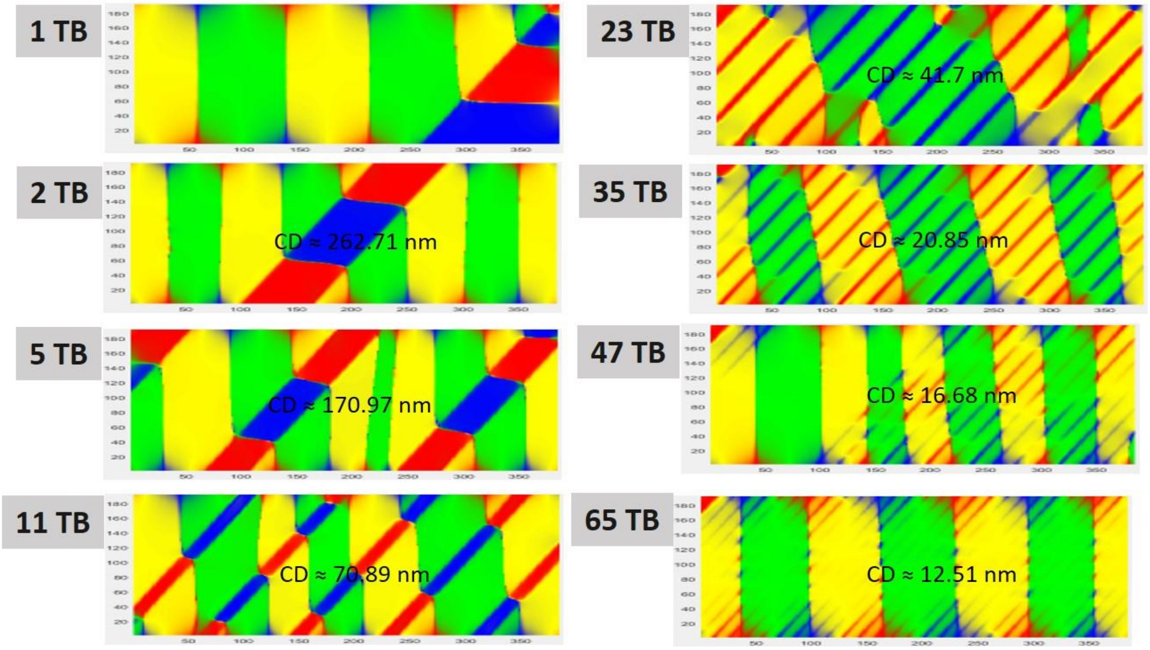

Figure C-4 Equilibrium magnetic domain structures evolution with increasing twin boundaries (or twin densities) from 1 to 65 (or 1.7 to 47 μm^{-1}) for a sample strained to 5%. “CD” denotes the closest distance between two twin boundaries.

APPENDIX D

Magneto-Mechanical Test Apparatus (MMTA)

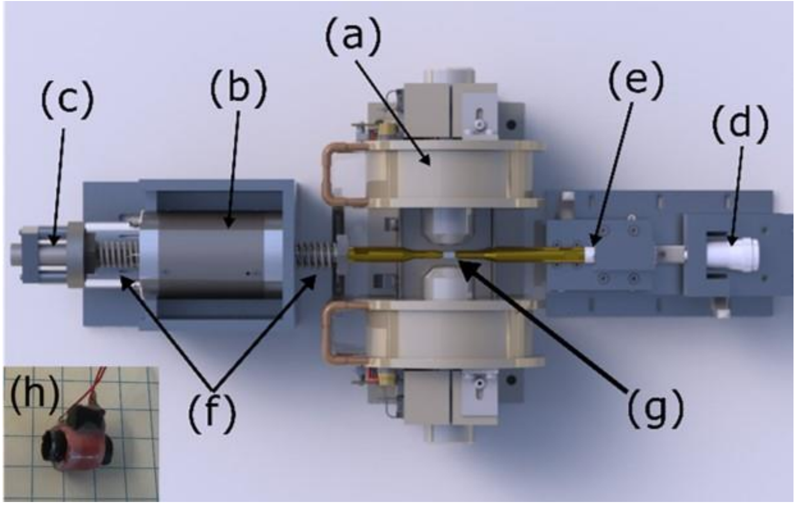

Figure D-1 MMTA apparatus with adjustable electromagnets. The setup consists of (a) field variable electromagnet, (b) Voice coil motor, (c) linear-variable differential transformer, (d) micrometer, (e) piezoelectric force transducer, (f) springs to tune the resonant frequency of the motor, (g) Ni-Mn-Ga specimen, and (h) pickup coil. Reprinted by permission from Springer Nature, [Shape memory and superelasticity, Efficiency of Energy Harvesting in Ni–Mn–Ga Shape Memory Alloys, P. Lindquist, T. Hobza, C. Patrick, and P. Müllner, COPYRIGHT (2018) [51].

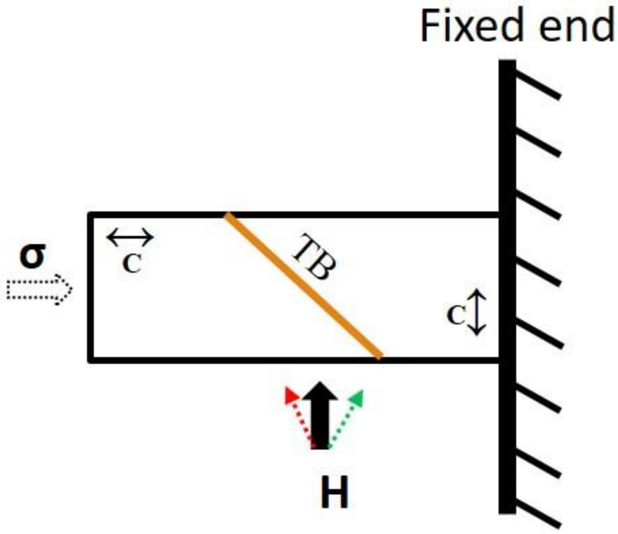

Figure D-2 Schematic of the Ni-Mn-Ga specimen with direction of mechanical force and bias magnetic field in MMTA. σ is force applied, TB is the twin boundary in the specimen, (↔ or ↕) is the direction of c-axis across the twin boundary and H is the direction of bias magnetic field. Red arrow: the direction of field tilted parallel to the twin boundary. Green arrow: the direction of field tilted away from the twin boundary.

(a) **0.2 T, 1% strain**

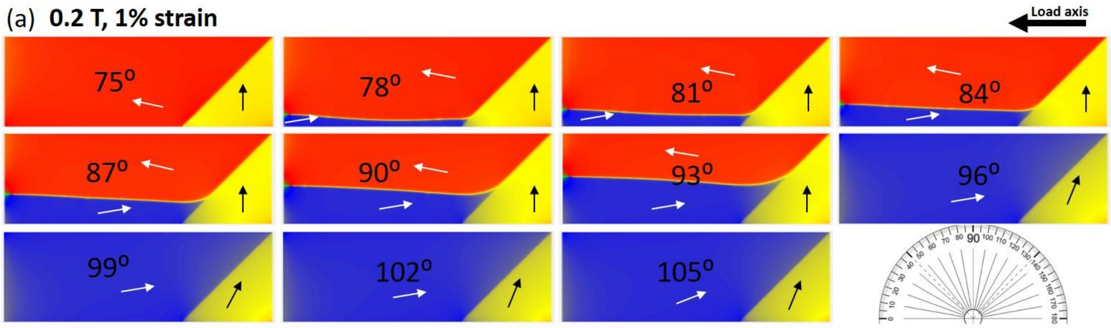

(b) **0.2 T, 5% strain**

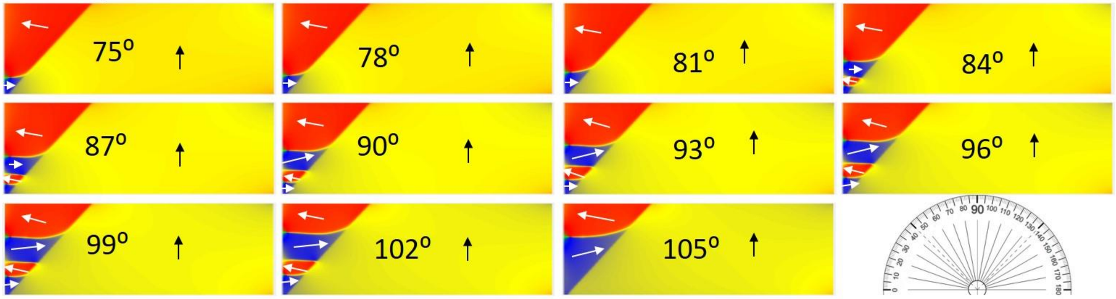

(c) **0.6 T, 1% strain**

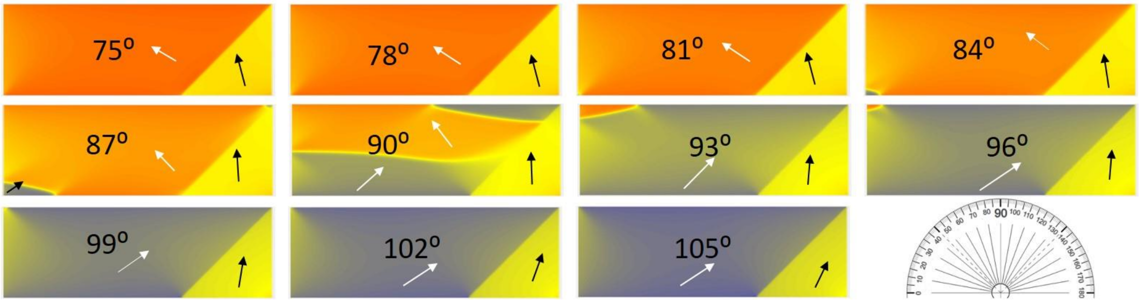

Figure D-3 Magnetic domain structures obtained from simulations at (a) 0.2 T, 1% strain, (b) 0.2 T, 5% strain, and (c) 0.6 T, 1% strain for various magnetic bias field orientations. The orientation of the bias field (with respect to the load axis) is denoted by the numbers on its corresponding domain structures. The arrows represent the direction of magnetization occupied in the center of each magnetic domain and the load axis is indicated by the thick arrow (top right corner). The yellow hue of the red and blue domains in (c) indicates the strong deviation of the magnetization direction from the direction of the axis of easy magnetization. The protractor image is a guide to visualize the direction of the external magnetic field with respect to the twin boundary, which is at 135°.

APPENDIX E

Python Script for Energy Plots

From the micromagnetics simulations, the energy (for anisotropy, exchange, stray field, and Zeeman energies) value associated with each cell from the simulating sample was extracted. A python script was built to plot these energy values as energy densities and distributed across the entire simulating sample. For this, a python script was generated and the script is as follows:

```
# coding: utf-8

# In[ ]:


import numpy as nm
import matplotlib.pyplot as plt

# Anisotropy Energy
# read file with anisotropy E, variable a
a = nm.loadtxt(fname="ani-Heatplots", delimiter="\s")

# file is a list of number (1 column) so reshape, variable a_r
a_r = a.reshape(9,73728)
print("Size of ani E values:", a_r.shape)

# Transpose to get all runs in separate columns, varialble a_T
a_T = a_r.T
print("Size of all runs for all ani E values in each column:",
a_T.shape)

# Extracting all rows in last column for ani E heatplot i.e. last
iteration, variable a_HP
a_HP = a_T[:,-1]
print("Size of ani HP for last run:", a_HP.shape)

# Creating the matrix of ani E values i.e. 384 x 192, variable
ani_matrix
ani_matrix = a_HP.reshape([192,384])
ani_matrix = ani_matrix[::-1] #for some reason the rows are
reversed
print("Size of ani E matrix:", ani_matrix.shape)

# Plotting the heatplot for ani E, variable ani_image
# converting E (J) to E(kJ/m^3)
for j in range(len(ani_matrix[0,:])):
    for i in range(len(ani_matrix[:,0])):
         ani_matrix[i][j] = ani_matrix[i][j]/(4.05*10**-21)
```

```
#ani_image = plt.imshow(ani_matrix, cmap=plt.cm.get_cmap('Reds',
20))
ani_image = plt.imshow(ani_matrix)
plt.colorbar(ani_image)
plt.clim(-40,200)
plt.title("Anisotropy Energy")
plt.show(ani_image)

# Exchange Energy
# read file with exchange E, variable e
e = nm.loadtxt(fname="ex-Heatplots", delimiter="\s")

# file is a list of number (1 column) so reshape, variable e_r
e_r = e.reshape(9,73728)
print("Size of ex E values:", e_r.shape)

## Transpose to get all runs in separate columns, varialble e_T
e_T = e_r.T
print("Size of all runs for all ex E values in each column:",
e_T.shape)

# Extracting all rows in last column for ex E heatplot i.e. last
#iteration, variable e_HP
e_HP = e_T[:,-1]
print("Size of ex HP for last run:", e_HP.shape)

# Creating the matrix of ex E values i.e. 384 x 192, variable
ex_matrix
ex_matrix = e_HP.reshape([192,384])
ex_matrix = ex_matrix[::-1] #for some reason the rows are
reversed
print("Size of ex E matrix:", ex_matrix.shape)

# Plotting the heatplot for ex E, variable ex_image
# converting E (J) to E(kJ/m^3)
for j in range(len(ex_matrix[0,:])):
    for i in range(len(ex_matrix[:,0])):
         ex_matrix[i][j] = ex_matrix[i][j]/(4.05*10**-21)

#ex_image = plt.imshow(ex_matrix, cmap=plt.cm.get_cmap('Reds',
20))
ex_image = plt.imshow(ex_matrix)
plt.colorbar(ex_image)
plt.clim(-40,200)
plt.title("Exchange Energy")
plt.show(ex_image)

# Stray Energy
# read file with stray E, variable s
s = nm.loadtxt(fname="stray-Heatplots", delimiter="\s")

# file is a list of number (1 column) so reshape, variable s_r
```

```
s_r = s.reshape(9,73728)
print("Size of stray E values:", s_r.shape)

# Transpose to get all runs in separate columns, varialble s_T
s_T = s_r.T
print("Size of all runs for all stray E values in each column:",
s_T.shape)

#Extracting all rows in last column for stray E heatplot i.e.
last iteration, variable s_HP
s_HP = s_T[:,-1]
print("Size of stray HP for last run:", s_HP.shape)

# Creating the matrix of stray E values i.e. 384 x 192, variable
stray_matrix
stray_matrix = s_HP.reshape([192,384])
stray_matrix = stray_matrix[::-1] #for some reason the rows are
reversed
print("Size of stray E matrix:", stray_matrix.shape)

# Plotting the heatplot for stray E, variable stray_image
# converting E (J) to E(kJ/m^3)
for j in range(len(stray_matrix[0,:])):
    for i in range(len(stray_matrix[:,0])):
         stray_matrix[i][j] = stray_matrix[i][j]/(4.05*10**-21)

#stray_image =
plt.imshow(stray_matrix,cmap=plt.cm.get_cmap('Reds', 20))
stray_image = plt.imshow(stray_matrix)#for min to max colors
plt.colorbar(stray_image)
plt.clim(-40,200)
plt.title("Stray field Energy")
plt.show(stray_image)

# Zeeman Energy
# read file with zeeman E, variable z
z = nm.loadtxt(fname="zee-Heatplots", delimiter="\s")

# file is a list of number (1 column) so reshape, variable z_r
z_r = z.reshape(9,73728)
print("Size of zeeman E values:", z_r.shape)

# Transpose to get all runs in separate columns, varialble z_T
z_T = z_r.T
print("Size of all runs for all zeeman E values in each column:",
z_T.shape)

# Extracting all rows in last column for zeeman E heatplot i.e.
#last iteration, variable z_HP
z_HP = z_T[:,-1]
print("Size of zeeman HP for last run:", z_HP.shape)
```

```
# Creating the matrix of zeeman E values i.e. 384 x 192, variable
zee_matrix
zee_matrix = z_HP.reshape([192,384])
zee_matrix = zee_matrix[::-1] #for some reason the rows are
reversed
print("Size of zeeman E matrix:", zee_matrix.shape)

# Plotting the heatplot for zeeman E, variable zee_image
# converting E (J) to E(kJ/m^3)
for j in range(len(zee_matrix[0,:])):
    for i in range(len(zee_matrix[:,0])):
         zee_matrix[i][j] = zee_matrix[i][j]/(4.05*10**-21)
#zee_image = plt.imshow(zee_matrix, cmap=plt.cm.get_cmap('Reds',
20))
zee_image = plt.imshow(zee_matrix)
plt.colorbar(zee_image)
plt.clim(-40,200)
plt.title("Zeeman Energy")
plt.show(zee_image)

#adding all the matrices i.e. all the 4 energies
#creating an empty matrix with all zeros
TMagE = nm.zeros([192,384])

# iterate through rows
#print("len(ani_matrix)=", len(ani_matrix[0,:]))
#print("ani_matrix[:,0]", ani_matrix[:,0])
for j in range(len(ani_matrix[0,:])):
    #print ("j:", j)
    for i in range(len(ani_matrix[:,0])):
        #print ("i:", i)
        TMagE[i][j] = ani_matrix[i][j] + ex_matrix[i][j] +
stray_matrix[i][j] + zee_matrix[i][j]

#print(TMagE[i][j].shape)

# Plotting Total magnetic energy, summation of 4 energies saved
#in variable TMagE and image variable is E_image
#print("Size of total E matrix:", r.shape)
#E_image = plt.imshow(TMagE, cmap=plt.cm.get_cmap('Reds', 20))
E_image = plt.imshow(TMagE)
plt.colorbar(E_image)
plt.clim(-40,600)
plt.title("Total Magnetic Energy")
plt.show(E_image)


import xlsxwriter

workbook = xlsxwriter.Workbook('arrays.xlsx')
worksheet = workbook.add_worksheet()
```

```
array = TMagE

row = 0

for col, data in enumerate(array):
    worksheet.write_column(row, col, data)

workbook.close()

# adding all the elements in T.MagE matrix

print("Total Magnetic energy of this structure =",nm.sum(TMagE))
```